



**UNSW**  
AUSTRALIA

T3 2020

**Many Body Quantum Chaos in  
Highly Charged Tin for use in  
Extreme-Ultraviolet Lithography**

Matthew Brand

z5061445

Supervisor:

Associate Professor Julian Berengut

## Originality Statement

I hereby declare that this submission is my own work and to the best of my knowledge it contains no materials previously published or written by another person, or substantial proportions of material which have been accepted for the award of any other degree or diploma at UNSW or any other educational institution, except where due acknowledgement is made in the thesis. Any contribution made to the research by others, with whom I have worked at UNSW or elsewhere, is explicitly acknowledged in the thesis. I also declare that the intellectual content of this thesis is the product of my own work, except to the extent that assistance from others in the project's design and conception or in style, presentation and linguistic expression is acknowledged.

Signed: 

Date: T3 2020

**Abstract**

The manufacture of next generation semiconductors requires the use of state of the art EUV lithography to form smaller and more efficient chip features. This method is not yet industry standard however, as the process has not been optimised to produce light that is of high enough power, reliability and stability for use in mass manufacturing. A significant issue is the characterisation of the properties of the tin plasma used to produce the EUV light, such as the atomic cross-sections, optical spectra and temperature of the constituent highly charged ions. Due to the open  $d$  and  $f$  shells of these ions and the strong interactions between different configurations, it is extremely computationally expensive to determine atomic properties because of the large size of the systems. However, by using statistical theories based on many body quantum chaos (MBQC), average properties can be obtained instead, drastically reducing the size of the problem. This thesis verifies that the tin systems exhibits the properties of MBQC and that statistical theories can indeed be applied to tin plasmas. The values for the spreading width, which the atomic cross-sections and spectra are dependent on, are calculated and shown to be constant with respect to energy at the first approximation. In addition, the values for the level growth parameter, which is necessary to perform temperature diagnostics is also calculated. Finally, the statistical theory for the line strength has been applied to a tin plasma, and is shown to be incomplete as it does not replicate the important spectral narrowing features due to configuration interactions that is known to occur in tin ions.

## Acknowledgements

Firstly, I would like to express my sincere gratitude to my supervisor A/Prof. Julian Berengut for his support and guidance throughout this thesis. At many stages in the course of this research I have greatly benefited from his advice, knowledge, direction and feedback. I could not have imagined having a better supervisor.

To my friends and the 2020 Physics Honours Cohort, thank you for preventing me from becoming a total hermit during this weird and trying year by providing me with some means of human interaction. Despite all the stress and Coronavirus fears, you have helped keep me balanced and given me plenty of opportunities to enjoy myself and be sociable (even if its just virtual beers over Zoom!).

Last but definitely not least, thank you to my family for their continuous support and encouragement. To Mum for providing all the brain food to keep me motivated. To Dad for helping to brainstorm and troubleshoot code when I got stuck, as well as proofreading my work. To Kayla for providing some levity and distraction throughout this long year so that I didn't go insane from overworking at home.

Matt Brand

**Table of Contents**

<b>Originality Statement</b> . . . . .	i
<b>Abstract</b> . . . . .	ii
<b>Acknowledgements</b> . . . . .	iii
<b>List of Figures</b> . . . . .	vi
<b>List of Tables</b> . . . . .	vii
<b>Nomenclature</b> . . . . .	viii
<b>1 Introduction</b> . . . . .	1
<b>2 Literature Review</b> . . . . .	3
2.1 Tin Plasma . . . . .	3
2.2 Many Body Quantum Chaos . . . . .	4
2.3 Random Matrix Theory . . . . .	5
2.3.1 The Ensemble Distribution . . . . .	6
2.3.2 Spectral Fluctuation Measures . . . . .	8
2.3.2.1 Wigner's Surmise . . . . .	8
2.3.2.2 The Dyson-Mehta Statistic . . . . .	9
2.3.2.3 The Porter-Thomas Distribution . . . . .	9
2.4 Doorway States . . . . .	10
2.5 Chaos in Atomic Systems . . . . .	12
2.5.1 Cerium . . . . .	12
2.5.2 Chaotic Eigenstates . . . . .	13
2.6 Electron Recombination in Highly Charged Ions . . . . .	16
2.6.1 Direct Recombination . . . . .	16
2.6.2 Resonant Recombination . . . . .	16
2.6.2.1 Recombination Cross-Sections . . . . .	18
2.6.2.2 Fluorescent Yield . . . . .	18
2.6.2.3 Autoionisation Width . . . . .	19
2.6.2.4 Radiative Width . . . . .	20

---

**TABLE OF CONTENTS**

---

2.7	Other Atomic Processes . . . . .	22
2.8	Transitions between Atomic States . . . . .	23
2.8.1	Line Strengths . . . . .	23
2.8.2	Einstein Coefficients . . . . .	23
2.8.3	Observed Intensity . . . . .	24
<b>3</b>	<b>Verification of MBQC in Highly Charged Tin Ions . . . . .</b>	<b>25</b>
3.1	Verification of Wigner’s Surmise and Distributed Eigencomponents . . . . .	25
3.2	Trends in MBQC Properties . . . . .	28
<b>4</b>	<b>Model for Spreading Width . . . . .</b>	<b>34</b>
4.1	Overview of the Atomic Hamiltonian . . . . .	34
4.2	Self-configuration Blocks . . . . .	36
4.3	Interaction Blocks . . . . .	36
4.3.1	One-differing Electron . . . . .	36
4.3.2	Two-differing Electrons . . . . .	38
4.3.3	Magnitude of the Corrections . . . . .	38
4.4	A Spreading Width Model . . . . .	39
4.5	Spreading Width and Level Growth Parameters in Tin . . . . .	40
<b>5</b>	<b>Transition Lines . . . . .</b>	<b>43</b>
5.1	A Derivation for the Statistical Line Strength . . . . .	43
5.2	A Mean Spectrum from Averaged Configurations . . . . .	45
5.3	The Impact of CI on the Emission Spectra . . . . .	50
5.3.1	Energy Shift . . . . .	50
5.3.2	Spectral Narrowing . . . . .	51
5.3.3	The Difficulty of a Generalised Heuristic . . . . .	52
5.4	A Statistical Plasma Intensity Spectrum . . . . .	53
<b>6</b>	<b>Conclusion . . . . .</b>	<b>55</b>
<b>References</b>	. . . . .	<b>60</b>

## List of Figures

Figure 1.	Evolution of patterning resolution and lithographic wavelength over time. . . . .	2
Figure 2.	Simplified schematics of the laser-droplet interaction in a typical industrial EUV light source module. . . . .	3
Figure 3.	Occupation numbers of single electron orbitals in the Ce atom as a function of eigen-state energy. . . . .	5
Figure 4.	Nearest neighbour spacing distributions for the Gaussian Ensembles. . . . .	8
Figure 5.	Components of the 590th eigenstate for $\text{Au}^{24+}$ with probability distribution fitted to a Lorentzian . . . . .	15
Figure 6.	Energy diagram of a dielectronic doorway state in multielectronic recombination . .	17
Figure 7.	Schematic diagram of multi-electron resonant capture of an electron through the $h^{-1}ab$ doorway state. . . . .	18
Figure 8.	Electron recombination rate of $\text{W}^{20+}$ . . . . .	21
Figure 9.	Ordered eigenstates of $\text{Sn}^{13+}$ with $J^\pi = 1/2^-$ . . . . .	26
Figure 10.	NNS distribution for $\text{Sn}^{13+}$ with $J^\pi = 1/2^-$ . . . . .	26
Figure 11.	Components of the 2200 <sup>th</sup> eigenstate $J^\pi = 1/2^-$ for $\text{Sn}^{13+}$ . . . . .	27
Figure 12.	MBQC parameters for highly charged tin ions . . . . .	29
Figure 13.	Average MBQC parameters for $\text{Sn}^{13+}$ as a function of energy threshold $E_{th}$ . . . . .	33
Figure 14.	Hamiltonian matrix diagram for atomic systems. . . . .	35
Figure 15.	Energy vs number of configurations $M$ for $\text{Sn}^{13+}$ . . . . .	35
Figure 16.	Number of energy levels in $\text{Sn}^{13+}$ as a function of energy . . . . .	40
Figure 17.	Oscillatory component of the level density normalised by the exponential density component, and the spreading width $\Gamma_{\text{spr}}$ for $\text{Sn}^{13+} J = 1/2$ , as a function of threshold energy $E_{th}$ . . . . .	41
Figure 18.	Line strengths for EUV producing configurations of $\text{Sn}^{12+}$ . . . . .	48
Figure 19.	Power intensity spectrum including up to the third level excitations for $\text{Sn}^{12+}$ at the LTE temperature of 26 eV . . . . .	49
Figure 20.	Energies of all second level excitations states in $\text{Sn}^{12+}$ . . . . .	51
Figure 21.	Spectra for second level excitations of $\text{Sn}^{12+}$ using the heuristic described in Section 5.3.3. . . . .	53
Figure 22.	Power intensity spectrum for a tin plasma at a non-LTE (LTE) temperature of 36 eV (26 eV). . . . .	54

**List of Tables**

Table 1.	MBQC chaos parameters for $\text{Sn}^{13+}, J^\pi = 1/2^-$ . . . . .	26
Table 2.	Primary EUV producing configurations of $\text{Sn}^{13+}$ with their corresponding parities, energies and level density local peaks. . . . .	42
Table 3.	Values for $\Gamma_{\text{spr}}$ and $\varepsilon_\rho$ in the $\text{Sn}^{7+} - \text{Sn}^{14+}$ systems. . . . .	42
Table 4.	Configuration average energies and number of projections for relativistic configurations in the ground and first excited states of $\text{Sn}^{12+}$ . . . . .	47
Table 5.	Single electron transition reduced matrix elements for $\text{Sn}^{12+}$ . . . . .	47
Table 6.	Fraction of ions present and spreading width in a tin plasma with a LTE temperature of 26 eV . . . . .	54

## Nomenclature

### Symbols

$\bar{x}$	Mean of $x$	$\hat{m}$	Reduced single body operator
$x^*$	Complex conjugate of $x$	$m_i$	Number of projections in the relativistic configuration $C_i$
$a/b/c/h$	Electron subshells	$N$	Number of states
$A^{(i)}$	RMS interaction of configuration blocks that differ by $i$ electrons	$\mathcal{N}$	Energy number staircase function
$A_{kl}^{ij}$	Scattering amplitude with incoming/outgoing particles $i/j$ and initial/final states $k/l$	$N_p$	Principal number of basis states mixed together in a complex state
$A_{12}$	Einstein coefficient for spontaneous emission from state 1 to state 2	$n_0$	Principal quantum number of the lowest unoccupied single particle state
$c$	Speed of light	$n_a$	Occupation number of subshell $a$
$C_j^{(i)}$	$j$ th basis state component in the $i$ th eigenstate	$O$	Orthogonal transformation
$C_i$	Self-configuration block	$p$	Total number of available single electron shells in a system
$C_{ij}$	Interaction block	$P(H)$	Ensemble probability distribution
$\hat{D}$	Electric dipole operator	$P(S)$	The Porter-Thomas distribution
$D$	Mean level spacing	$P(s)$	Nearest neighbour spacing distribution
$\hat{d}$	Reduced electric dipole operator	$S$	Transition line strength
$d$	Energy level spacing	$s$	Normalised energy level spacing
$E_c$	Cutoff energy	$T$	Plasma temperature
$E_i$	Energy of configuration $i$	$V$	RMS residual coupling interaction
$E_{th}$	Energy threshold for calculation	$v$	Number of valence electrons in a system
$f_{\mu\nu}$	Distribution function of each component	$\hat{V}$	Two body Coulomb operator
$g_i$	Statistical weight of state $i$	$\hat{v}$	Reduced two body Coulomb operator
$H$	Hamiltonian	$V^{(i)}$	$i$ th correction to $V$
$h$	Planks constant	$w$	Chaotic strength function
$I$	Ionisation threshold	$Z$	Partition function
$I_n$	Identity matrix of size $n$	$\alpha$	Angle of rotation
$I_{12}$	Intensity of transition from state 1 to 2	$\chi$	Averaged mixed states
$j$	Single particle total momentum	$\Delta$	Energy conservation term
$J^\pi$	Total angular momentum $J$ and parity $\pi$	$\Delta_3$	The Dyson-Mehta statistic
$k$	Electron momentum	$\tilde{\delta}$	Finite width $\delta$ function
$k_B$	Boltzmann constant	$\varepsilon$	Electron and single particle energy
$L$	Correlation length of observed energy interval	$\varepsilon_0$	Permitivity of free space
$l$	Single particle angular momentum	$\varepsilon_\rho$	Level growth parameter
$M$	Number of configurations included in the Hamiltonian	$\Gamma$	Total width
$\hat{M}$	Single body operator	$\Gamma^{(a)}$	Autoionisation width
		$\Gamma^{(r)}$	Radiative width
		$\Gamma_{spr}$	Spreading width
		$\lambda$	Photon wavelength
		$\omega$	Photon energy

$\omega_{ba}$	Single electron transition energy	Sn	Tin
$\omega_f$	Fluorescence yield	W	Tungsten
$\Phi$	Basis states	$m$	Ground state shell occupancy
$\Psi$	Complex mixed states	$n$	Principle quantum number
$\rho$	Level density	$X^*$	Excited state
$\rho_{ab}^{(21)}$	Transition matrix element for the $b \rightarrow a$ single electron transition component in the $1 \rightarrow 2$ transition	$X^{q+}$	Ion with charge q
$\sigma^\gamma$	Photon induced process cross-section	Z	Atomic number
$\sigma^e$	Electron induced process cross-section	$Z_i$	Ionic charge
$\sigma_c$	Capture cross-section		
$\sigma_d$	Direct recombination cross-section		
$\sigma_r$	Resonant recombination cross-section		
$\theta$	Heaviside step function		
$\zeta$	Distribution parameter associated with mean level spacing		

### Common Chemical Symbols

$\gamma$	Photon
$e^-$	Electron
E1	Electric dipole transition
E2	Electric quadrupole transition
M1	Magnetic dipole transition
Au	Gold
Ce	Cerium

### Acronyms

a.u.	Atomic energy unit, 1 a.u.=27.211 eV
CI	Configuration Interaction
CSF	Configuration State Function
EUV	Extreme Ultra-Violet
FWHM	Full Width Half Maximum
GOE	Gaussian Orthogonal Ensemble
GSE	Gaussian Symplectic Ensemble
GUE	Gaussian Unitary Ensemble
LLP	Laser Produced Plasma
LTE	Local Thermal Equilibrium
MBQC	Many Body Quantum Chaos
NNS	Nearest Neighbour Spacing
RMT	Random Matrix Theory
UTA	Unresolved Transition Array

## 1 Introduction

The development of smaller, more cost effective semiconductors has driven technological advancement in modern day society, leading to the invention of every day devices such as the home computer and smart phones. Moore's law, which states that the number of transistors on a microchip doubles every two years, has allowed the development of revolutionary new technologies to occur as semiconductor components have become smaller and more powerful. In order for the size of features in semiconductors to reduce, the lithographic resolution of the manufacturing process must increase. Current state of the art "193i" immersion lithography uses a 193 nm UV laser light to produce features that can be as small as 14 nm in size (see Fig. 1). However, the industry has stalled in further reducing this size in a reliable and cost effective manner using current technology, necessitating the introduction of extreme-ultraviolet (EUV) lithography [1]. EUV uses light that is an order of magnitude shorter at 13.5 nm to produce smaller features that are sub-10 nm in size. This will greatly reduce the scale of features in components of CPUs and flash memory, pushing the semiconductor industry and computers closer to the atomic scale while decreasing the cost and power consumption of individual transistors.

Big name international semiconductor companies such as Intel, Samsung and Huawei have already started experimenting with designing and manufacturing microchips with EUV. Although it's been recently reported that these companies are starting to use EUV in the "5 nm process" to produce select components for their latest generation of devices, this is just a naming convention and does not indicate the true feature size. EUV has not yet been used to its fullest potential in creating entire features at a sub-10 nm scale and is not yet industry standard. This is due to there still being major challenges to overcome in the production EUV light that is of a high enough power, reliability and stability for use in mass manufacturing [2].

Unlike "193i" immersion, EUV light is produced by irradiating a tin (Sn) droplet with a high power laser multiple times [3]. This ablates the tin, turning it into a dense plasma containing highly charged tin ions. There are multiple ionic species within the plasma, which all remarkably produce a significant amount of light in the narrow bandwidth around 13.5 nm that is useful for lithography [4]. However, to become industry standard, the power output from this EUV light must be increased by an order of magnitude. As the atomic processes that these ions undergo to produce this light are not fully understood, further theoretical research is needed to describe the system and inform industrial design choices that will enable EUV to be commercially viable for mass manufacture.

Tin plasma is difficult to analyse with its theoretical treatment being incomplete. A missing aspect from the current framework is the statistical theory of many body quantum chaos (MBQC). Because of the open  $4d$  shell in the tin ions, the ions have extremely dense energy levels that result in a heavily mixed state that is highly chaotic, changing under any small perturbation. This fundamentally alters the atomic properties of the plasma and must be accounted for to accurately calculate the atomic processes that result in the emission of EUV light such as the rates of recombination, ionisation and excitation of the ions.

In this thesis the properties of MBQC within highly charged tin ions will be analysed, and a model for how these properties alter with increasing energy will be developed. This will enable the application of MBQC to various excitation levels within the tin systems that are responsible for the emission of

light. Furthermore, a statistical theory for the emission spectrum of a chaotically mixed system will be applied and compared to the traditional analytical theory.

The thesis has been divided into 6 sections. Section 2 provides an overview of the tin plasma EUV emission process for lithography. In addition, the physical and mathematical processes of MBQC, as well as its application to atomic systems, has been summarised. Section 3 analyses to what extent MBQC can be applied to tin ions, while Section 4 develops a model for how the statistical parameters, in particular the spreading width, evolve with energy. Section 5 presents the application of the statistical theory to obtain the emission spectrum. Section 6 concludes the thesis. All code written and utilised in this thesis can be found in the github repository linked [here](#)<sup>1</sup>.

A MBQC description of highly charged tin ions will advance current understanding in atomic and plasma physics, as well as furthering the growth and application of industrial EUV-lithography.

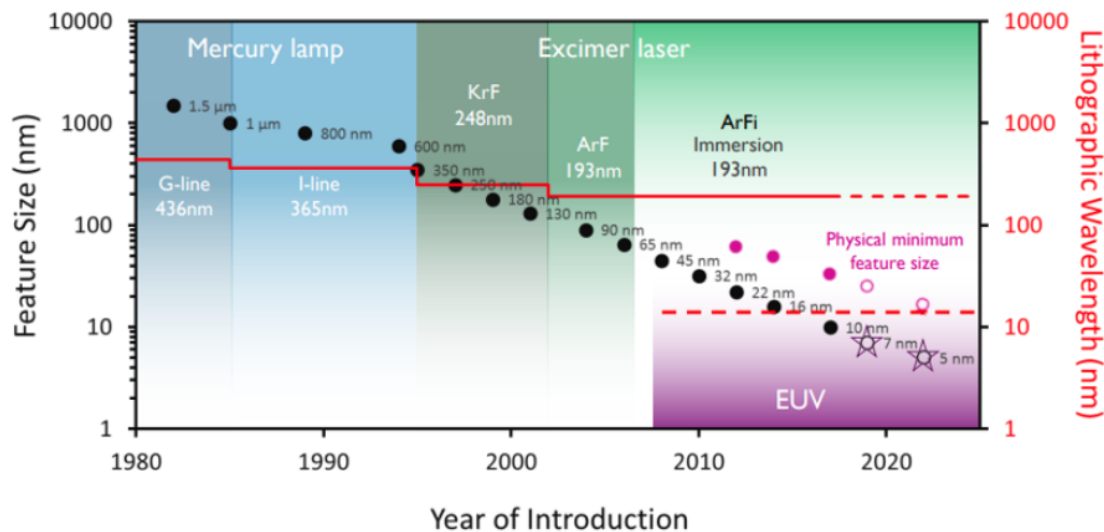


Figure 1. Evolution of patterning resolution and lithographic wavelength over time. Figure from Ref. [5]. Engineering feats such as immersion lithography, optical proximity correction and double patterning, have allowed feature sizes well below the diffraction limit, but only at very high cost [1].

<sup>1</sup>URL link: <https://github.com/MIB101/MBQC-in-Sn>

## 2 Literature Review

### 2.1 Tin Plasma

EUV light is industrially produced through the irradiation of chemically pure molten tin droplets by infrared lasers as shown in Fig. 2. Droplets approximately  $30\text{ }\mu\text{m}$  in diameter are initially hit with a relatively low intensity laser which deforms and propels the droplet into a pancake shape [6, 7]. This has been shown to give optimal conditions for the production of light as it results in optical breakdown and prevents re-absorption of the emitted light by the plasma [8]. A second higher energy laser is then shone on the deformed droplet, causing it to ablate, creating a dense laser-produced-plasma (LPP) that emits EUV light. The LPP has a typical electron density of  $10^{19}\text{ cm}^{-3}$  and a temperature of 20–40 eV(232 000–464 000 K). In these conditions, the  $\text{Sn}^{7+}$ – $\text{Sn}^{14+}$  ions become prevalent and emit light due to numerous atomic processes [4]. Remarkably, all of these tin species emit a significant portion of light in the narrow 2% spectral bandwidth centred at 13.5 nm, which matches the reflectivity bandwidth of the specialised Mo/Si multilayer mirrors that have been specially designed for EUV-lithography, as most matter readily absorbs the short EUV wavelengths of light.

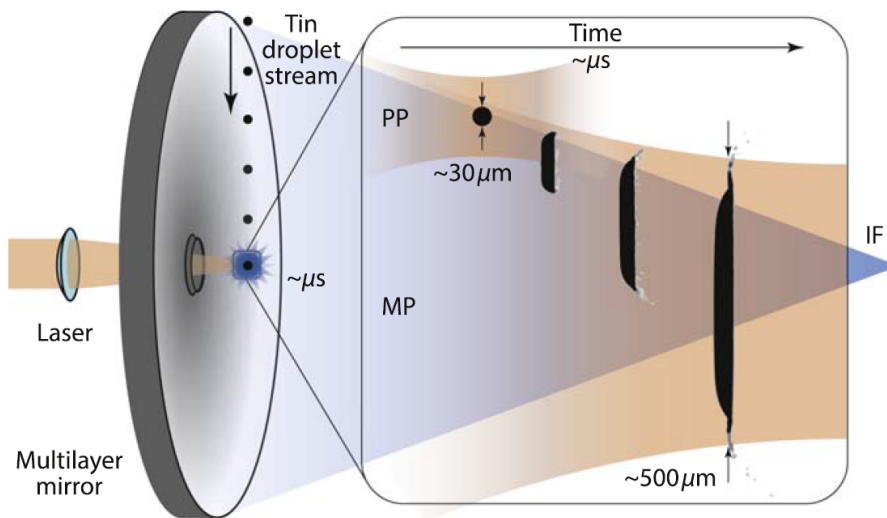


Figure 2. Simplified schematics of the laser-droplet interaction in a typical industrial EUV light source module. Figure and following caption from Ref. [2]. A spherical liquid tin microdroplet is hit by a laser prepulse (PP). The droplet is propelled by the plasma created by the PP and gets reshaped into an extended disk-shaped target suitable for the main-pulse (MP) laser irradiation, creating the highly-ionised, EUV emitting tin plasma. A multilayer mirror collects the in-band EUV light emitted in the laser-facing hemisphere and focuses it towards the so-called intermediate focus (IF).

The EUV light in the 13.5 nm bandwidth was initially thought to be produced by the atomic transitions between the first excited states  $4p^54d^{m+1} + 4p^64d^{m-1}4f$  and the ground state  $4p^64d^m$ , where  $m = 14 - q$  and  $q$  is the ion charge [4]. Recently though, it has been found that most of the light actually involves transitions between highly and intermediately excited states in addition to transitions with the ground state. In particular, the set of transitions responsible for the creation of the majority of the

relevant EUV light by tin ions come from the triply, doubly and singly excited states [9]:

$$4p^34d^{m+3} + 4p^44d^{m+1}4f \rightarrow 4p^44d^{m+2} + 4p^54d^m4f \rightarrow 4p^54d^{m+1} + 4p^64d^{m-1}4f \rightarrow 4p^64d^m. \quad (1)$$

Possible atomic states in these shell configurations number in the thousands, resulting in indistinguishable spectral lines and so-called unresolved transition arrays (UTA) [10]. However traditional UTA methods fail to accurately reproduce the experimentally observed spectra [11].

The open  $4d$  shells in the tin ions result in hundreds of thousands of possible energy levels and over  $10^{10}$  possible transition interactions [9]. This causes the system to form heavily mixed states that require a statistical approach to understand, as explicitly calculating the atomic properties is functionally impossible. The atomic processes the tin ions undergo, which includes recombination, ionisation, excitation and relaxation of the atoms, determine which ionic species are present and ultimately the final optical spectra of a given plasma. However, these processes are currently poorly understood in the context of heavily mixed states in highly charged ions. For instance, one of the more likely processes for the cooling of the plasma, multi-electronic recombination (the primary mechanism by which electrons and ions recombine) is typically not included in most plasma simulations [12] despite its reaction cross-section being two orders of magnitude larger than that of simpler radiative recombination.

As exact calculations cannot be performed, a statistical description of the system may provide an alternate avenue for the efficient calculation and design of the optical spectrum for tin plasmas.

## 2.2 Many Body Quantum Chaos

The atomic spectra of highly charged ions with open shells can only be accurately calculated for the ground state and relatively low lying transitions. Plasmas are highly energetic though, with dynamical processes such as electron excitation, ionisation and recombination needing spectra to be calculated up to and beyond the ionisation energy. Due to large degeneracy splitting of these highly excited states, the level spacing between different energy levels becomes too small for any computational method based on exact wave-functions. The small spacings between energy levels cause the ion to exist in a heavily mixed state. This leads the ions to exhibit many body quantum chaos (MBQC), where any small perturbation of the system, such as higher order corrections or relativistic effects, results in completely different basis configurations [13].

Due to the large amount of mixing, individual eigenstates cannot be readily identified and the only remaining good quantum numbers that can be used to describe the system are the total angular momentum  $J$  and parity  $\pi$ . To illustrate this point in atomic systems, Flambaum et al. show that in the highly chaotic cerium (Ce) atom, eigenstates at higher energies cannot be described by single electron orbitals [13]. As shown in Fig. 3, the occupation numbers of each orbital clearly have non-integer values and can no longer be considered good quantum numbers.

MBQC is a statistical method of describing many body quantum systems and is analogous to classical statistical theories such as the ideal gas law for hot gasses. Instead of considering the motion of each and every individual particle within the gas, the ideal gas law takes an ensemble average of all possible micro-states to determine macroscopic properties such as pressure and temperature. These macroscopic properties can be determined without considering the system specific Hamiltonian. In a similar vein,

MBQC takes a statistical average of the possible atomic states and energies of the ion to describe atomic properties such as the energy spectra and atomic ionisation, recombination and scattering cross-sections, without needing to consider the complex resonant structures and configuration interactions of the system in detail [14].

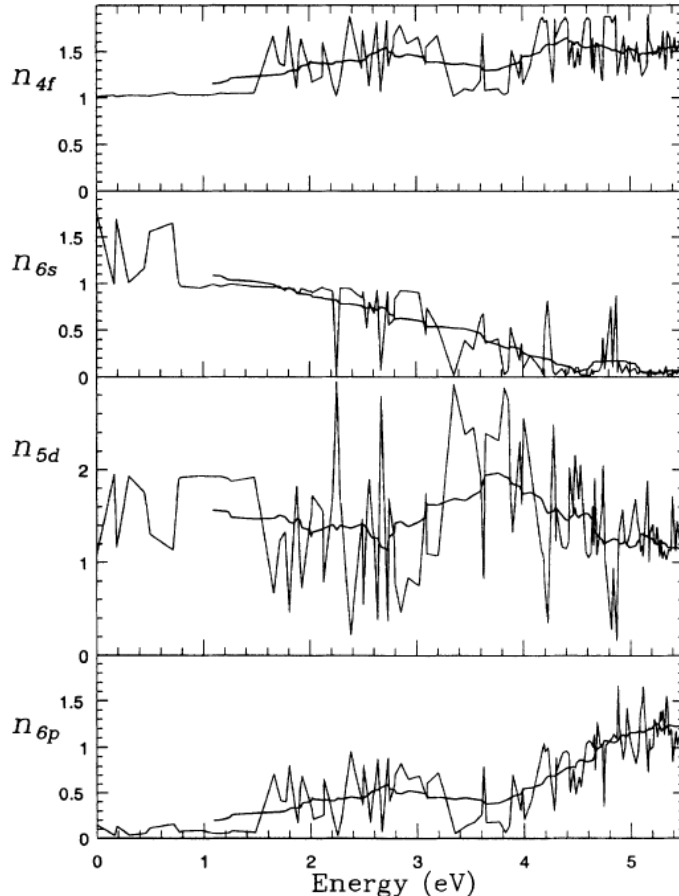


Figure 3. Occupation numbers of single electron orbitals in the Ce atom as a function of eigenstate energy. The thick line shows a moving average over the nearest 19 neighbouring levels. Figure from Ref [13].

### 2.3 Random Matrix Theory

The mathematics behind MBQC is based on random matrix theory (RMT). Usually, the exact structure and spectra of a system are calculated directly from the system Hamiltonian, with the results compared to experimental data to test the validity of the theory. RMT instead aims to identify the spectral properties expected from a strongly interacting system by characterising the fluctuations and distributions of the energy eigenvalues.

RMT was first introduced to physics by Eugene Wigner in the late 1950's as a means to determine the properties of atomic nuclei [15, 16]. The neutron scattering experiments performed by Fermi in the 1930's [17, 18] had revealed the presence of many narrow resonances in the nuclei of multiple atoms, the origin of which was a mystery at the time. Bohr later argued [19] that the existence of these finely spaced resonances was a result of the strong nucleon-nucleon interactions in the nucleus. However, it was still largely unknown how to determine the Hamiltonian and corresponding spectra of

these strongly-interacting, complex quantum mechanical systems.

As the Hamiltonian of the nuclear system was unknown, Wigner instead considered an ensemble of all possible Hamiltonian's from which the system could originate. By averaging over the ensemble, fluctuation properties of the spectrum were able to be determined and compared to the actual fluctuations obtained from experimental data.

The Hamiltonian ensemble is constructed by considering Hamiltonians whose matrix elements are defined by a given probability distribution. The distribution chosen for the ensemble is dependent on the physical symmetry of the system being considered. The most common choice of symmetry is that the system is time and rotationally invariant (i.e. energy and total angular momentum are conserved). In this scenario, the Hamiltonian  $H$  can be shown to be apart of the Orthogonal group (see Ref. [20]). As a result, the matrix can be made real and symmetric with

$$H = H^* = H^{-1} \quad \text{i.e.} \quad H_{\mu\nu} = H_{\nu\mu} = H_{\mu\nu}^*. \quad (2)$$

As the distribution of matrix elements in this type of system will be later shown to be uncorrelated, Gaussian-distributed random variables, this distribution is known as a Gaussian Orthogonal Ensemble (GOE).

Two other ensembles that are also usually considered are the Gaussian Unitary Ensemble (GUE) and the Gaussian Symplectic Ensemble (GSE). The GSE relates to systems that are time invariant, but not rotationaly invariant, while the GUE describes systems with no symmetries and is commonly used in nuclear physics to test for time-reversal invariance.

As the Hamiltonains for the atomic systems that will be considered later in this thesis are calculated for the fixed quantum numbers  $J^\pi$  and conserve energy, this discussion will be limited to that of the GOE. Discussions on the GUE and GSE can be found in Refs. [20, 21] which also include detailed derivations and proofs of the following functions and distributions.

### 2.3.1 The Ensemble Distribution

When discussing the GOE, a finite  $N$  dimensional submatrix for each symmetry  $J^\pi$  of the actually infinite dimensional Hilbert space is considered, with the limit  $N \rightarrow \infty$  later applied when developing appropriate statistical measures. As  $H$  is real and symmetric, there are  $N(N + 1)/2$  real parameters in each matrix. In matrix space, the volume element  $dH$  and probability distribution function  $P(H)$  (which has Gaussian form) for the Hamiltonian are given by

$$dH = \prod_{\mu \leq \nu=1}^N dH_{\mu\nu} \quad (3)$$

$$P(H) dH = N_0 \exp\left(-\frac{N}{4\zeta^2} \text{Tr}(H^2)\right) dH, \quad (4)$$

where  $N_0$  is a normalisation factor and  $\zeta$  is a parameter that is usually associated with the average level spacing. This equation arises by considering the constraints that  $P$  must be an invariant function of  $H$  and that the matrix elements must be independent [22], i.e. for the orthogonal transformation  $O$  that relates  $H$  to  $H'$

$$O = \begin{pmatrix} \cos \alpha & \sin \alpha & 0 \\ -\sin \alpha & \cos \alpha & 0 \\ 0 & 0 & I_n \end{pmatrix} \quad \text{such that} \quad H = O^T H' O \quad (5)$$

$$\frac{dP(H)}{d\alpha} = 0 \quad (6)$$

$$P(H) = \prod_{\lambda < \mu=1}^N f_{\mu\nu}(H_{\mu\nu}), \quad (7)$$

where  $I_n$  is the identity matrix of size  $n = N - 2$ ,  $\alpha$  is the angle of rotation, and  $f_{\mu\nu}$  is the distribution function for each matrix element.

Using the symmetric properties of  $H$  in Eq. (2), Eq. (4) can be re-written as

$$\text{Tr}(H^2) = \sum_{\mu=1}^N H_{\mu\mu}^2 + \sum_{\mu < \nu=1}^N 2H_{\mu\nu}^2 \quad (8)$$

$$\Rightarrow P(H) dH = N_0 \prod_{\mu=1}^N \exp\left(-\frac{N}{4\zeta^2} H_{\mu\mu}^2\right) dH_{\mu\mu} \times \prod_{\rho < \sigma=1}^N \exp\left(-\frac{N}{2\zeta^2} H_{\rho\sigma}^2\right) dH_{\rho\sigma}. \quad (9)$$

From Eq. (9), it can be seen that the mean squared dispersion of the off-diagonal elements ( $2\zeta^2$ ) is half that of the diagonal elements ( $4\zeta^2$ ). In the GOE, as every off-diagonal element is populated by the same distribution, all states are coupled to together with the same average strength by the assumed strong interactions in the system. This results in the complete mixing of the states and gives rise to the experimentally observed level repulsion in nuclear systems. In the non-interacting limit where all off-diagonal elements are zero, the Hamiltonian ensemble reduces to only diagonal elements that are independently Gaussian-distributed. The average spectrum in this case has a Gaussian profile with Poissonian distributed energy level spacings, as is normally observed in simple atomic systems. Furthermore, from Eq. (9) it can be seen that the threshold for significant mixing between states roughly occurs when the average interaction is greater than the mean level spacing  $D$  (noting again that  $\zeta$  is associated with  $D$ ). When this is true (i.e. Eq. (10) is true), the off-diagonal distribution is far from unity and significantly influences the overall distribution.

$$\overline{H_{\rho\sigma}^2} \gtrsim D^2 \sim \zeta^2. \quad (10)$$

The ensemble can alternatively be formulated using the  $N$  eigenvalues  $E_\mu$  and  $N(N - 1)/2$  eigenvector generators  $dO$  of the orthogonal transform  $O$  which diagonalises  $H$ . In this representation the volume element and distribution are

$$dH = dO \prod_{\mu < \nu=1}^N |E_\mu - E_\nu| \prod_{\rho=1}^N dE_\rho \quad (11)$$

$$P(H) dH = N_0 dO \exp\left(-\frac{N}{4\zeta^2} \sum_{\mu=1}^N E_\mu^2\right) \prod_{\rho < \sigma=1}^N |E_\rho - E_\sigma| \prod_{\nu=1}^N dE_\nu. \quad (12)$$

From this form of the distribution, the level repulsion is made explicit by the  $|E_\rho - E_\sigma|$  factor. When the energy levels are close to each other, the probability distribution approaches zero. However, when the levels repel each other and are evenly distributed with  $|E_\rho - E_\sigma| = (E_{\max} - E_{\min})/N$ , the probability

is maximised. Equation (12) also shows that the eigenvalues  $E$  and eigenvectors  $O$  are uncorrelated random variables as they are separate factors in the expression.

### 2.3.2 Spectral Fluctuation Measures

#### 2.3.2.1 Wigner's Surmise

There are many measures of the spectral fluctuations that can be derived from the GOE. However the measure that is most commonly used, and easiest to understand, is the nearest-neighbouring-spacing distribution (NNS). This gives the probability distribution for the possible size of the energy level spacing between neighbouring eigenvalues  $P(s)$ , where  $s$  is the actual level spacing  $d$  normalised by the mean level spacing  $D$  in the system.

$$P(s) = \frac{\pi}{2} s \exp(-\pi s^2/4), \quad \text{where } s = \frac{d}{D}. \quad (13)$$

This equation is known as Wigner's surmise as it was first surmised by Wigner from the expected level repulsion characteristics of a strongly interacting Hamiltonian without derivation [23]. This was first explicitly derived from the GOE by Gaudin a few years later [24].  $P(s)$  in Eq. (13) is exact for a 2-dimensional system, and while the actual distribution for higher dimensions cannot be given in closed form, it has been shown to be in excellent agreement with the 2-dimensional form as displayed in Fig. 4a. Consequently, Eq. (13) is frequently used to describe the level spacing distribution. It is briefly noted that the NNS distributions for GSE and GUE systems have a similar form to that of the GOE. The NNS distribution for all three Gaussian ensembles, as well as the Poisson distribution, have been plotted in Fig. 4b. If the experimental data for a system can be fitted to one of the  $P(s)$  distributions, it is a good indicator that the system can be accurately described using the relevant Gaussian ensemble statistics.

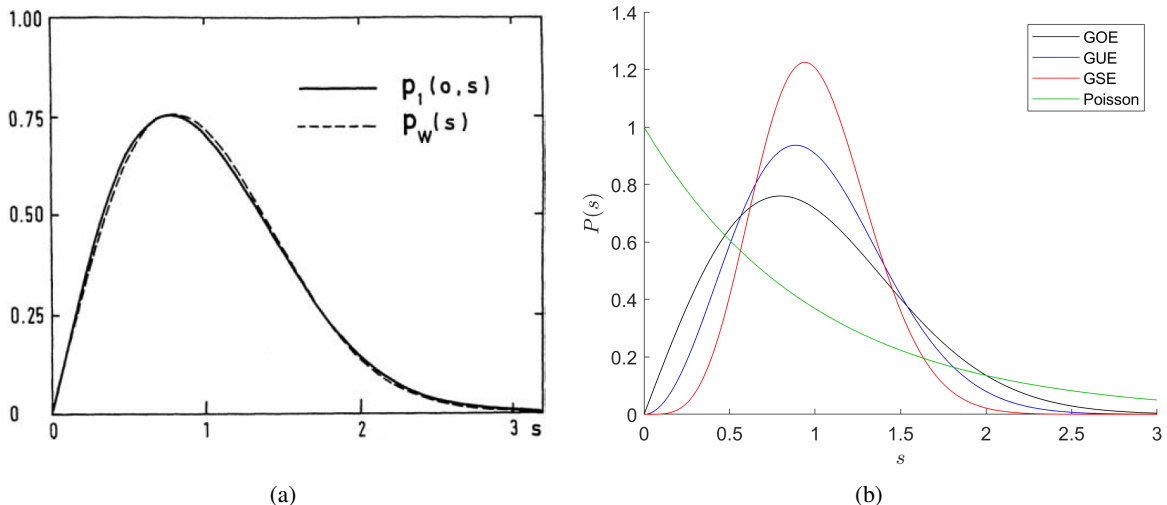


Figure 4. Nearest neighbour spacing distributions for the Gaussian Ensembles: (a) shows a comparison between the distribution for many dimensions (solid line) and Wigner's surmise for 2 dimensions (dashed line), figure from Ref. [24]; (b) shows the NNS distributions for the GOE, GUE, GSE and Poisson ensembles.

### 2.3.2.2 The Dyson-Mehta Statistic

While Wigner's surmise describes the overall distribution of the level spacing, it does not give any information about the correlation between these spacings. This is instead usually given by the Dyson-Mehta statistic  $\Delta_3$ , also known as the spectral rigidity in nuclear physics [25]. If the spectrum was constructed by randomly drawing energy spacings from the NSS, the variance in the number of levels would grow linearly with the energy of the spectrum. While this is the case for a Poisson Distribution [20], the variance in a GOE grows logarithmically. This indicates that small and large spacings are not randomly chosen, but alternate in some manner.  $\Delta_3$  quantifies these long range correlations in the spectra and is given by Eq. (14)

$$\Delta_3(L) = \min_{a,b} \frac{1}{L} \left\langle \int_{E_0}^{E_0+L} [\mathcal{N}(E') - a - bE'] dE' \right\rangle_{E_0} \quad (14)$$

$$\mathcal{N}(E) = \int_{-\infty}^E dE' \sum_{\mu} \delta(E' - E - E_{\mu}), \quad (15)$$

where  $\mathcal{N}$  is the energy number staircase function of the spectra,  $a + bE'$  is the line of best fit over the energy interval  $E_0 \rightarrow E_0 + L$ , and the expected value of the variance between the two is averaged with respect to choice of initial energy  $E_0$ . For large  $L$  this results in a logarithmic relationship for the GOE and a linear relationship for the Poisson distribution.

$$\Delta_3^{\text{GOE}}(L) \approx \frac{1}{\pi^2} (\ln L - 0.0687) \quad (16)$$

$$\Delta_3^{\text{Poisson}}(L) = \frac{L}{15}. \quad (17)$$

As the calculations to obtain  $\Delta_3$  from experimental data are much more involved [26], typically only the NNS distribution is considered when confirming the properties of the experimental data, as demonstrated in Section 3.

### 2.3.2.3 The Porter-Thomas Distribution

Another distribution derived from the GOE is the Porter-Thomas distribution [27]. This gives the distribution of the squared matrix elements  $P$ , and as such is usually associated with the transition line strengths  $S$  in a system. Line strengths will be discussed in more detail in Section 2.8.

$$P(S) = \frac{1}{\sqrt{2\pi S\bar{S}}} \exp\left(-\frac{S}{2\bar{S}}\right), \quad (18)$$

where  $\bar{S}$  is the mean line strength. Experimentally, it is the transmission rate of the lines that is typically measured. This is proportional to  $\omega^3 S$  where  $\omega$  is the transition photon energy. The measurement equipment usually has a minimum threshold intensity below which a signal is not detected. Therefore, even if the line has a high strength, if the energy is too low the line may be omitted from the data. If transitions only in the energy range  $0 < \omega < \omega_{max}$  are measured, the Porter-Thomas distribution can be

modified to give the expected distribution observed by the measurement device [28]

$$P(S) = \begin{cases} 0, & S \leq S_{min} \\ \frac{S_0}{\sqrt{2\pi S}} \exp\left(-\frac{S}{2S}\right) \left[1 - \left(\frac{S_{min}}{S}\right)^{1/3}\right], & S > S_{min} \end{cases}, \quad (19)$$

where  $S_{min}$  is the minimal line strength that can be observed at  $\omega = \omega_{min}$ , and  $S_0$  is a normalisation factor.

## 2.4 Doorway States

Due to the strong mixing of the basis states inherent in systems that exhibit MBQC, the strength of transitions between states can be enhanced through a concept known as doorway states. Consider a specific mode of excitation, for instance the electric dipole operator  $\hat{D}$ , acting on the ground state  $|\Phi_g\rangle$ . The normalised dipole mode  $|\Psi_D\rangle$  and mean excitation energy  $E_D$  are given by

$$|\Psi_D\rangle = \hat{D}|\Phi_g\rangle, \quad \langle\Psi_D|\Psi_D\rangle = 1, \quad E_D = \langle\Psi_D|H|\Psi_D\rangle. \quad (20)$$

The dipole mode is generally not an eigenstate of the system, so the variance of the Hamiltonian with respect to the dipole mode  $\Delta H^2$ , is non-zero

$$\Delta H^2 = \langle\Psi_D|H^2|\Psi_D\rangle - E_D^2 = \sum_{\mu \geq 1} (H_{D\mu})^2, \quad (21)$$

where  $\mu$  denotes states that are orthogonal to  $|\Psi_D\rangle$  but have the same quantum numbers. As such, the mean squared coupling strength of the dipole mode with the other states of the system is given by

$$V_{\text{dipole}}^2 = \frac{1}{N} \Delta H^2 = \frac{1}{N} \sum_{\mu \neq D} H_{D\mu}^2. \quad (22)$$

This definition of the mean coupling strength can be readily extended to include all modes of transition with [29]

$$V^2 = \frac{1}{N^2} \sum_{\mu \neq v} H_{\mu v}^2. \quad (23)$$

Because the value of the dipole interaction is non-vanishing, the cross-section for the dipole absorption process has a large number of sharp lines that occur at eigenstates of  $H$ . Taking the ratio of  $V$  to the mean level spacing, gives a measure of the energy interval where states are strongly mixed with the dipole mode. Within this interval, the dipole absorption lines become much stronger and a resonance occurs at or near  $E_D$ . This is known as a doorway state and can be thought of as a two step process.

1. The initial transition mode is formed. It is not an eigenstate of the system, but is embedded in and mixed with the spectrum of other excited states
2. The state then decays into eigenstates of  $H$ , enhancing the transition strengths.

The mechanics of a doorway state can be clearly seen through the theory of multi-electron recombination (which will be discussed in more mathematical detail in Section 2.6). Instead of all the excess energy from the incident electron being transferred to a single particle, the incident electron is captured and forms a doorway state which then decays and disperses the energy among the many electrons in the atom. This statistical distribution of the energy is akin to the break shot in a game of billiards, where although the white ball imparts enough kinetic energy for the colliding ball to escape the table, the energy is instead shared between all the balls on the table. Due to this sharing of energy, the incident electron is statistically unlikely to regain all of its energy and escape. As a result, radiative decay is preferred in multi-electron recombination over auto-ionisation, unlike in standard dielectric recombination theories, and recombination has a much higher probability (and hence cross-section) of occurring.

For a doorway state in a GOE, the Hamiltonian can be written as

$$H = \begin{pmatrix} E_D & H_{Dv} \\ H_{\mu D} & H_{\mu v} \end{pmatrix}, \quad (24)$$

where  $E_D$  is the mean excitation energy of the doorway state. As there is now a distinct state, the system is no longer orthogonally invariant. However, in the subspace  $\mu \neq D$ , the orthogonality remains. Furthermore, in the limit  $N \rightarrow \infty$ , the entire system can still be considered invariant. As a consequence though, observables depend on the orthogonally invariant mean square coupling matrix element  $V$ , and not on the individual coupling matrix elements of  $H$  [30].

From RMT, Bohr and Mottelson [29] derive that the strength function of the doorway state, which gives the probability per unit energy interval of finding the eigenstate with energy  $E$  mixed within the doorway state, is given by the Lorentzian

$$\frac{1}{2\pi} \frac{\Gamma_{\text{spr}}}{(E - E_D)^2 + (\Gamma_{\text{spr}}/2)^2}, \quad \Gamma_{\text{spr}} = 2\pi V^2 \rho, \quad (25)$$

where  $\rho$  is the energy level density and  $\Gamma_{\text{spr}}$  is known as the spreading width and gives the length of the energy interval over which significant admixtures of the eigenstates can be found within the doorway state.

In nuclear systems,  $\Gamma_{\text{spr}}$  is known to vary slowly with energy. This can be argued intuitively [30]. An increase in energy increases the level density of the system, but also increases the wavefunction complexity which strongly reduces each matrix element. Therefore the increase in level density is compensated by a corresponding decrease in mean-square coupling strength. The two effects are shown to cancel exactly in very simple models [31], and  $\Gamma_{\text{spr}}$  has been experimentally verified to slowly vary for isospin mixing in nuclear systems [32].

In atomic systems, the only analysis of the energy dependence of the spreading width was performed on highly charged gold (Au) ions [33]. While it was found that  $\Gamma_{\text{spr}}$  remained essentially constant, only a few relativistic configurations within a single non-relativistic configuration were examined. No analytical justification has since been provided.

## 2.5 Chaos in Atomic Systems

Since their introduction to physics, MBQC and RMT have predominately been used to determine properties of nuclear systems [30, 34–36]. More recently, the theory of MBQC has also been applied to complex atomic systems such as highly charged ions. In atomic systems the suitability of using RMT to describe the spectra is not known *a priori*. The electronic structure of atoms differs significantly from the structure of the nucleus. The Coulomb interaction between electrons is generally much weaker than the interaction between nucleons. This electron interaction is non-negligible though, and it is not immediately known whether it is strong enough to induce MBQC behaviour in a given atom or ion.

RMT was first applied to atomic systems by Rosenzweig and Porter in 1960 [22]. The NNS distribution was examined for three chains of neutral atoms with atomic numbers  $Z = 21\text{--}28$ ,  $39\text{--}46$ , and  $71\text{--}79$  where the  $3d$ ,  $4d$  and  $5d$  shells were filled respectively. It was found that the first chain exhibited pure Poisson energy spacing, the second exhibited a mix between Poisson and GOE spacing, and the third exhibited pure GOE spacing. This was attributed to the spin-orbit coupling strength growing in strength with  $Z$ . As the atom becomes more relativistic, the  $LS$  coupling scheme decreases in effectiveness and  $L$  and  $S$  are no longer good quantum numbers. This work was extended by Camarda and Georgopoulos in 1983, with the level spacing for atoms before the third chain with  $Z = 57\text{--}71$  being analysed [37].  $\Delta_3$  was calculated for these atoms and it was found that the long-range correlations in the spectra were consistent with GOE predictions.

More recently, Flambaum et al. performed an in-depth analysis of MBQC in atomic systems, in particular on the rare earth element Ce [13]. Applications of doorway states has also been extensively studied in gold (Au) and tungsten (W) highly charged ions, which will be detailed in Section 2.6.

### 2.5.1 Cerium

The most comprehensive study of if and how MBQC can be applied to atomic systems was performed by Flambaum et al. on Ce [13]. Ce has a large number of valence electrons ( $n = 4$ ) which can be distributed among many possible orbitals when excited, resulting in an exponentially large number of configurations for the basis of the many electron system when performing calculations. Configurations in the system are classified by  $J^\pi$  with different  $J^\pi$ 's not interacting. Due to the large density of states, the average spacing between levels is smaller than the residual interaction, and the interaction can mix and alter the basis states from that of single-electron orbitals. As the fine structure intervals between levels are much larger than the average level spacing, single electron orbitals have non-integer occupancies as was shown in Fig. 3 and the levels can no longer be classified using the  $LS$  coupling scheme. The excited states in each  $J^\pi$  manifold can instead be thought of as being formed by the strong mixing of a principal number of basis states  $N_p$ , which becomes non-perturbative for large interactions ( $V/D > 1$ ). This situation is very similar to that observed in the compound nucleus, and as such RMT was thought to be applicable.

Through analysis of the NNS distribution it was found that a GOE could indeed be used to describe the atomic system. However, as the Hamiltonian used to calculate a real complex system such as this is known, RMT ensemble averaging does not need to be performed. Instead, an alternate interpretation of spectral averaging was developed, whereby averaging is performed over neighbouring chaotic eigenstates instead of ensembles.

### 2.5.2 Chaotic Eigenstates

In the chaotic system, the structure and number  $N_p$  of principal components in the basis states determines the magnitude of the matrix elements between states. In Ce, it was found that the  $N_p$  principal components were mixed in a random fashion, with the matrix element  $H_{\mu\nu} \propto 1/\sqrt{N_p}$  [13]. The average spacing between levels is given by  $D \sim \Gamma_{\text{spr}}/N_p$ , where  $\Gamma_{\text{spr}}$  is the spreading width and gives the interval over which the single component is mixed. This is the same spreading width discussed in Section 2.4. The admixture of nearest states is hence given by  $H_{\mu\nu}/D \propto \sqrt{N_p}$ . This gives rise to the idea of localisation of the eigenstates, where perturbation mixes the basis states locally, with components of the given mixed state rapidly vanishing as they move away from the eigenstate energy.

Analysis of the eigenstate components  $C_j$  against the eigenvalue energies  $E_j$ , showed that the components were randomly distributed but mostly localised near the eigenstate. The strength function introduced by Wigner [15, 16] is considered so that the distribution of components in the eigenstate can be studied in more detail. The level density as a function of energy  $E$ , weighted by the probability of finding the  $j$ th basis state in the  $i$ th eigenstate of the system,  $\rho_w(E, j)$ , and its average are given by

$$\rho_w(E, j) = \sum_i C_j^{(i)2} \delta(E - E_i) \quad (26)$$

$$\overline{\rho_w(E, j)} = D^{-1} \overline{C_j^{(i)2}} \quad (27)$$

$$\equiv D^{-1} w(E_j; E, \Gamma_{\text{spr}}, N_p) \quad \text{with} \quad E \approx E_i. \quad (28)$$

There are two different ways of performing this averaging. The first is to take an ensemble average of random matrices. The second is to average over the neighbouring eigenstates  $i$  and components  $j$ . While both methods should yield identical results for physical quantities, only the second can be performed on a unique matrix obtained experimentally.

A function  $w$  was introduced in Eq. (28). This is the strength function and describes the eigenstate composition in terms of the number of principal components  $N_p$  and the width over which the principal components occur  $\Gamma_{\text{spr}}$ . Models and numerical calculations [15, 16, 29] show that  $w$  depends strongly on the difference between the basis state energy  $E_j - E$  and is a symmetric function. Normalisation of the eigenstates imposes the following requirement

$$\sum_j C_j^{(i)2} = 1 \Rightarrow \sum_j w(E_j; E, \Gamma_{\text{spr}}, N_p) = 1 \quad (29)$$

$$\rightarrow \int w(E_j; E, \Gamma_{\text{spr}}, N_p) \frac{dE_j}{D} = 1. \quad (30)$$

While  $w$  is assumed to be a smooth, symmetric function, there are effects that distort its shape. The main effect is a low-energy displacement of the maximum due to the second order perturbation shift of the energy  $\Delta E_i = \sum_j V_{ij}^2 / (E_i - E_j)$ . There is also a skewness to lower energies for low energy eigenstates as the basis is bounded from below, and the presence of additional shoulders due to nonstatistic deviations, but these properties are neglected.

$w$  can be solved to give the same Lorentzian curve and spreading width, derived by Bohr and Mottelson [29] and discussed in Section 2.4, Eq. (25). As such, this method of averaging has the same physical results as ensemble averaging, and RMT can be used to describe the composition of the eigenstates. Using the normalisation condition in Eq. (30), Eq. (32) is obtained. An example of this MBQC averaging applied to the eigenstate in atomic systems is provided in Fig. 5.

$$\overline{C_j^{(i)2}} = w(E_j; E, \Gamma_{\text{spr}}, N_p) \quad \text{with} \quad E \approx E_i \quad (31)$$

$$= \frac{1}{N_p} \frac{\Gamma_{\text{spr}}^2/4}{(E_i - E_j)^2 + \Gamma_{\text{spr}}^2/4} \quad (32)$$

$$N_p = \frac{\pi \Gamma_{\text{spr}}}{2D} \quad (33)$$

$$\Gamma_{\text{spr}} = \frac{2\pi V^2}{D} \quad \text{from Eq. (25).} \quad (34)$$

It is noted that when the level spacing is much greater than the spreading width, (i.e. the interaction is weak), this reduces to the usual perturbation mixing result [13]

$$|E_i - E_j| \gg \Gamma_{\text{spr}} \quad \Rightarrow \quad \overline{C_j^{(i)2}} \approx \frac{V^2}{(E_i - E_j)^2}. \quad (35)$$

For systems where MBQC is applicable, approximate solutions  $\Psi_v$  can be constructed from the basis states  $\Phi_k$  and eigenstate components  $C_k^{(v)}$  without the resource intensive process of diagonalising large Hamiltonians as

$$|\Psi_v\rangle = \sum_k C_k^{(v)} |\Phi_k\rangle \quad (36)$$

$$\left|C_k^{(v)}\right|^2 = \frac{2D}{\pi \Gamma_{\text{spr}}} \frac{\Gamma_{\text{spr}}^2/4}{(E_v - E_k)^2 + \Gamma_{\text{spr}}^2/4} \quad (37)$$

$$\Gamma_{\text{spr}} = 2\pi V^2 \rho(E_v). \quad (38)$$

Furthermore, as the level density for a given momentum  $J^\pi$  and energy  $E_v$  can be estimated using the variance of the interaction energies with respect to the configuration energies  $\sigma^2$  [33];

$$\rho(E_v) \approx N(2\pi\sigma^2)^{-1/2} \quad (39)$$

$$\sigma^2 = \frac{1}{N} \sum_{ij} H_{ij}^2 - \frac{1}{N^2} \left( \sum_i H_{ii} \right)^2 \quad (40)$$

$$= (N-1)V^2 + \frac{1}{N} \sum_i (H_{ii} - E_v)^2, \quad (41)$$

these equations allow for the quick and economic estimation of eigenstates for very large systems.

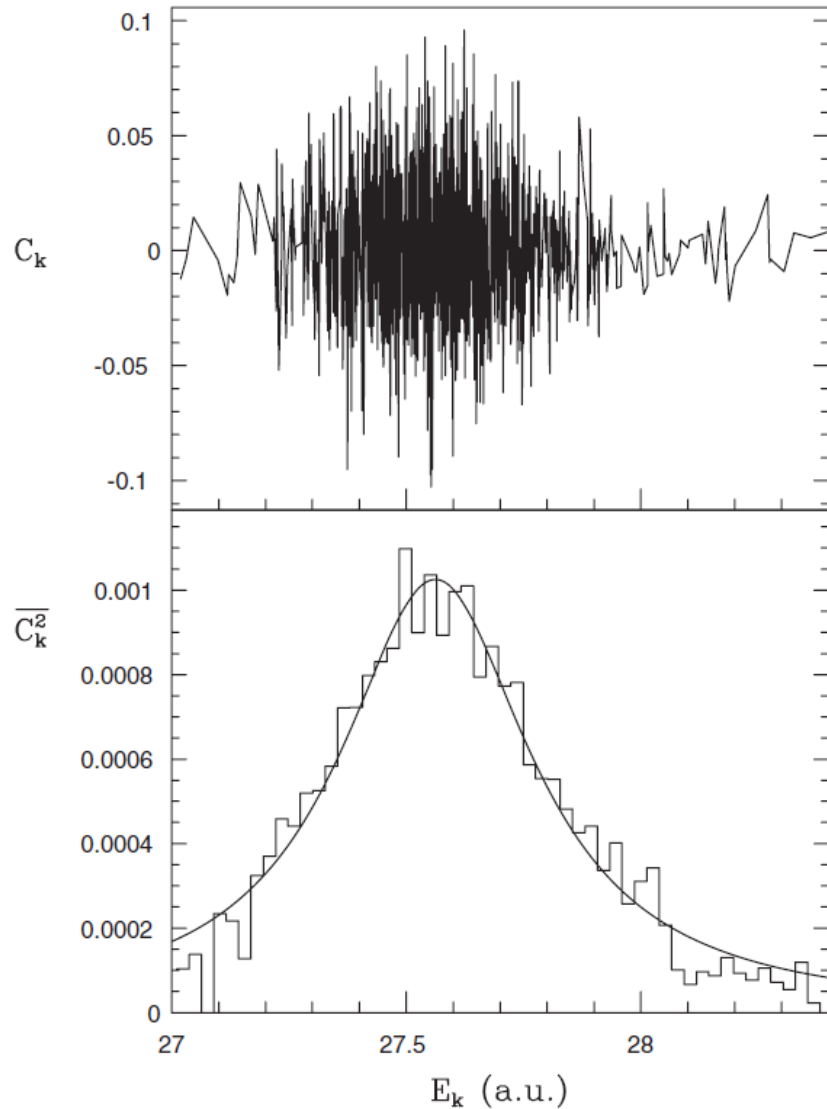


Figure 5. Components of the 590th eigenstate for  $\text{Au}^{24+}$  with probability distribution (histogram) fitted to a Lorentzian (solid line). Figure from Ref. [14].

## 2.6 Electron Recombination in Highly Charged Ions

The main mechanism of cooling in plasma, and emission of light, is an electron recombining with an ion. The processes involved in electron recombination need to be fully included in plasma codes so that the evolution of the states within the plasma, and the resulting emission spectra, can be accurately determined. Furthermore, a statistical theory derived from MBQC to calculate the recombination cross-sections of chaotic, highly charged ions has been successfully applied to plasma systems. Numerical results were obtained that strongly agreed with the experimental data.

Typically, only direct recombination is considered as it is a significantly simpler calculation. However this tends to underestimate the capture cross-section by orders of magnitude in complex highly charged ions. This has been quantitatively rectified by the MBQC theory of resonant recombinations and doorway states. First applied to Au systems [38], MBQC solved the long standing issue of “enormous discrepancies between theoretical and experimental rate coefficients” in the recombination of  $\text{Au}^{25+}$  forming  $\text{Au}^{24+}$ , where the observed cross-section was two orders of magnitude greater than that predicted by direct recombination [39]. After confirmation that the system could be described by a GOE, Gribakin, Gribakina, and Flambaum [38] demonstrated how the capture cross-section was primarily due to resonant multi-electronic recombination via electron capture into multiply-excited compound states of the system. Further work on the  $\text{W}^{20+}$  system has resulted in a detailed theory of resonant recombination [14, 40–43].

### 2.6.1 Direct Recombination

In direct recombination, a free electron  $e^-$  with energy  $\epsilon = k^2/2$  is captured by the target ion  $X$  with charge  $q$ . The excess energy from the incident electron is directly radiated away by a photon  $\gamma$



In a Coulomb field, the direct recombination cross-section  $\sigma_d$  is given by the relatively simple Kramers formula [44]

$$\sigma_d \approx \frac{32\pi}{3\sqrt{3}c^3} \frac{Z_i^2}{k^2} \ln\left(\frac{Z_i}{n_0 k}\right), \quad (43)$$

where  $Z_i$  is the ionic charge,  $n_0$  is the principal quantum number of the lowest unoccupied single particle orbital, and  $c$  is the speed of light. Figure 8a shows the direct recombination rate for the  $\text{W}^{20+}$  system. It can be clearly seen that  $\sigma_d$  underestimates the cross-section by two orders of magnitude.

### 2.6.2 Resonant Recombination

In resonant recombination, the excess energy from the incident electron is not immediately radiated away, but instead excites other electrons within the ion. The excited electrons then decay by photoemission. A special case is dielectronic recombination, where the incident electron only excites a single

electron within the atom before decay [45, 46].



While dielectronic recombination by itself can be used to explain very simple systems with low charges [14], it is inadequate for more complicated highly charged ions where chaotic compound resonances are present. In these resonances, dielectronic, trielectronic and other capture processes cannot be separated as the compound state is a mixture of multiple excited electrons. All these excited configurations contribute to and mix within the capture amplitude.

Despite this, dielectronic states still play a very important role in multi-resonant recombination theory. Initially the incident electron collides with the ion and excites a single electron by exchanging a virtual photon, forming an intermediate dielectronic state. This is followed by a “chain reaction” in which the two excited electrons interact with and excite other ground state electrons [41]. This is a fast internal decay from the dielectronic doorway state, and is much faster than the external autoionisation or radiative decays. Photons can be emitted at any stage of this chain reaction. Continuing the billiards analogy from Section 2.4, during the break shot, the white ball will first hit a single ball on the table, imparting some of its energy (i.e. the dielectric state as two balls now have energy). This second ball then almost immediately imparts its energy to all the other balls. All balls will then eventually slow down and return to rest (i.e. emit photons). Figure 6 shows an energy schematic of a dielectronic atomic doorway state.

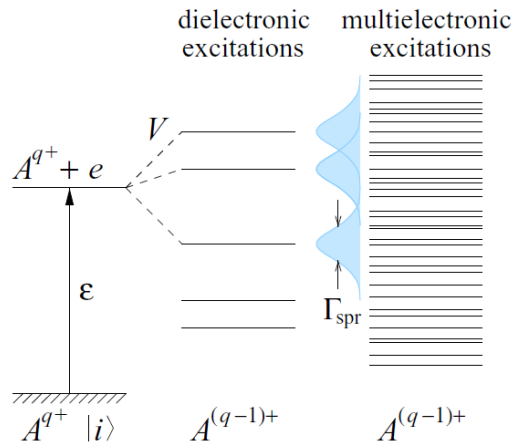


Figure 6. Energy diagram of a dielectronic doorway state in multielectronic recombination. Figure from [42].

A perturbative approach to multi-electron recombination is drawn in Fig. 7. An initial electron  $c$  with energy  $\epsilon$  collides with an atomic electron in state  $h$ . It loses some energy and falls to the  $a$  excited state, while exciting  $h$  to the state  $b$ , forming the dielectronic doorway state  $h^{-1}ab$ . One of these electrons then interacts with other electrons within the ion producing more excitations, although none have enough energy to escape the system [14].

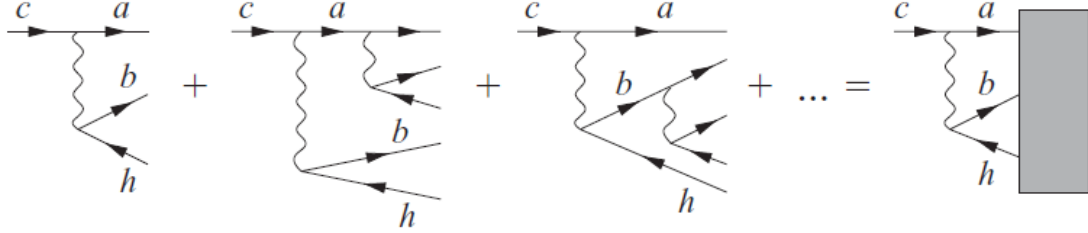


Figure 7. Schematic diagram of multi-electron resonant capture of an electron through the  $h^{-1}ab$  doorway state. Wavy lines show the Coulomb interaction. The shaded block represents the final strongly mixed multi-configurational eigenstate. Figure from [14].

### 2.6.2.1 Recombination Cross-Sections

The recombination cross-section for low energy electrons  $\sigma_r$  is given by [47]

$$\sigma_r = \frac{\pi}{k^2} \sum_v \frac{2J+1}{2J_i+1} \frac{\Gamma_v^{(r)} \Gamma_v^{(a)}}{(\epsilon - \epsilon_v)^2 + \Gamma_v^2/4} \quad (45)$$

$$\Gamma_v = \Gamma_v^{(r)} + \Gamma_v^{(a)}, \quad (46)$$

where  $J_i$  is angular momentum of the initial (ground state) of the ion,  $J$  are the angular momenta of the resonances, and  $\epsilon_v = E_v - I$  is the position of the  $v$ th resonance relative to the ionisation threshold of the compound (final state) ion.  $\Gamma_v^{(r)}$ ,  $\Gamma_v^{(a)}$ , and  $\Gamma_v$  are the radiative width, autoionisation width and total width respectively. If the resonance spectrum is dense ( $D \ll \Delta\epsilon \ll \epsilon$ ), the cross-section can be averaged over the interval  $\Delta\epsilon$  that contains many resonances to give [40]

$$\overline{\sigma}_r = \frac{\pi^2}{k^2} \frac{1}{(2J_i+1)} \sum_{J^\pi} (2J+1) \rho_{J^\pi} \left\langle \frac{\Gamma_v^{(r)} \Gamma_v^{(a)}}{\Gamma_v} \right\rangle \quad (47)$$

$$\rho_{J^\pi} \propto \frac{2(2J+1)^2}{(2J_m+1)^2} \exp\left(-\frac{(2J+1)^2}{2(2J_m+1)^2}\right), \quad (48)$$

where  $\rho_{J^\pi}$  is the level density for a given  $J^\pi$  and  $J_m$  is the  $J$  with the most levels within the system.

### 2.6.2.2 Fluorescent Yield

$\overline{\sigma}_r$  can be factored into the fluorescent yield  $\omega_f$  and average capture cross-section  $\overline{\sigma}_c$

$$\omega_f \equiv \frac{\Gamma^{(r)}}{\Gamma^{(r)} + \Gamma^{(a)}} \quad (49)$$

$$\overline{\sigma}_r = \overline{\sigma}_c \omega_f \quad (50)$$

$$\overline{\sigma}_c = \frac{\pi^2}{k^2} \frac{\Gamma^{(a)}}{(2J_i+1)} \sum_{J^\pi} (2J+1) \rho_{J^\pi}. \quad (51)$$

The fluorescent yield gives the probability that the excited ion stabilises through radiative decay, instead of ejecting the captured electron through autoionisation. It is assumed that the only open channels are

radiative decay (inelastic) and autoionisation (elastic). All other inelastic channels such as electronic excitations are closed [14].

At low energies, the fluorescence is near unity. When the electron energy is near the ionisation threshold there is only a single autoionisation channel through which the decay to the ground state can occur, while there are thousands of open photoemission channels [41]. In this case radiative decay occurs with near 100% certainty and  $\overline{\sigma}_r \approx \overline{\sigma}_c$ .

At higher energies, many more autoionisation channels become open as there are many possible low lying excited states within the ion that could ionise. In this case the fluorescence is small and the recombination cross-section is

$$\overline{\sigma}'_r = \frac{\pi^2}{k^2} \frac{\Gamma^{(r)}}{(2J_i + 1)} \sum_{J\pi} (2J + 1) \rho_{J\pi}, \quad (52)$$

and in general the cross-section can be given by

$$\overline{\sigma}_r \approx \frac{\overline{\sigma}_c \overline{\sigma}'_r}{\overline{\sigma}_c + \overline{\sigma}'_r}. \quad (53)$$

### 2.6.2.3 Autoionisation Width

The autoionisation width  $\Gamma_v^{(a)} = 2\pi |\langle \Psi_v | \hat{V} | \Phi_i; \varepsilon \rangle|^2$  gives the transition rate between the complex final resonant state  $\Psi_v$ , and the initial basis state  $\Phi_i$  (which is usually dominated by a single configuration) and incident electron with energy  $\varepsilon$  due to the two body Coulomb interaction  $\hat{V}$ , where [14, 40]

$$\hat{V} = \frac{1}{2} \sum_{a,b,h,c} \langle a, b | \hat{v} | h, c \rangle a_a^\dagger a_b^\dagger a_h a_c, \quad (54)$$

and  $\hat{v}$  is the reduced Coulomb operator.

The complex final state  $\Psi_v$  can be written in terms of a superposition of basis states through RMT as shown in Eq. (36), resulting in

$$\Gamma_v^{(a)} = 2\pi \sum_{k,k'} C_k^{(v)*} C_{k'}^{(v)} \langle \Phi_i; \varepsilon | \hat{V} | \Phi_{k'} \rangle \langle \Phi_k | \hat{V} | \Phi_i; \varepsilon \rangle. \quad (55)$$

As the eigenstate coefficients in RMT are assumed to be uncorrelated random variables

$$\overline{C_i^{(u)}} = 0 \quad \text{and} \quad \overline{C_i^{(u)*} C_j^{(v)}} = |C_i^{(u)}|^2 \delta_{ij} \delta_{uv}, \quad (56)$$

the average autoionisation width is

$$\overline{\Gamma^{(a)}} = 2\pi \sum_k \overline{|C_k^{(v)}|^2} |\langle \Phi_k | \hat{V} | \Phi_i; \varepsilon \rangle|^2, \quad (57)$$

which using the strength function from Section 2.5, gives a capture cross-section of

$$\overline{\sigma}_c = \frac{\pi}{k^2} \sum_d \frac{2J+1}{2(2J_i+1)} \frac{\Gamma_{\text{spr}}}{(\varepsilon - \varepsilon_a - \varepsilon_b + \varepsilon_h)^2 + \Gamma_{\text{spr}}^2/4} 2\pi |\langle \Phi_d | \hat{V} | \Phi_i; \varepsilon \rangle|^2, \quad (58)$$

where  $\varepsilon_{a/b/h}$  are the single electron orbital energies of the  $a/b/h$  states respectively, and  $d$  is the di-electronic (doubly excited) doorway states of the system that have finite energy spreading width  $\Gamma_{\text{spr}}$ . Summing over the magnetic numbers and performing an angular reduction of the two body Coulomb matrix elements gives the final expression for the capture cross-section [14, 40, 41, 43]

$$\overline{\sigma}_c = \frac{\pi^2}{2k^2} \sum_{ab,h,lj} \frac{|\langle a,b | \hat{V} | h, \varepsilon l j \rangle - \langle b,a | \hat{V} | h, \varepsilon l j \rangle|^2 \Gamma_{\text{spr}}}{(\varepsilon - \varepsilon_a - \varepsilon_b + \varepsilon_h)^2 + \Gamma_{\text{spr}}^2/4} \langle n_h (1-n_a)(1-n_b) \rangle \quad (59)$$

$$= \frac{\pi^2}{k^2} \sum_{ab,h,lj} \frac{\Gamma_{\text{spr}}}{(\varepsilon - \varepsilon_a - \varepsilon_b + \varepsilon_h)^2 + \Gamma_{\text{spr}}^2/4} \sum_{\lambda} \frac{\langle a,b | V_{\lambda} | h, \varepsilon l j \rangle}{2\lambda + 1} \left[ \langle a,b | \hat{V}_{\lambda} | h, \varepsilon l j \rangle - (2\lambda + 1) \right] \\ \times \sum_{\lambda'} (-1)^{\lambda+\lambda'+1} \begin{Bmatrix} \lambda & j_a & j \\ \lambda' & j_b & j_h \end{Bmatrix} \langle b,a | \hat{V}_{\lambda'} | h, \varepsilon l j \rangle \left[ \frac{n_h}{2j_h + 1} \left( 1 - \frac{n_a}{2j_a + 1} \right) \left( 1 - \frac{n_b}{2j_b + 1} \right) \right], \quad (60)$$

where  $n$  are the occupation numbers of the respective subshells and  $l, j$  are the angular and total momentum of the incident electron. The terms in the square bracket are the direct and exchange interactions. The reduced Coulomb matrix element is

$$\langle a,b | V_{\lambda} | h,c \rangle = \sqrt{(2j_a+1)(2j_b+1)(2j_h+1)(2j_c+1)} \xi(l_a+l_c+\lambda) \xi(l_b+l_h+\lambda) \\ \times \begin{pmatrix} \lambda & j_a & j_c \\ 0 & -\frac{1}{2} & \frac{1}{2} \end{pmatrix} \begin{pmatrix} \lambda & j_b & j_h \\ 0 & -\frac{1}{2} & \frac{1}{2} \end{pmatrix} R_{\lambda}(a,b;h,c) \quad (61)$$

$$\xi(l) = \frac{1}{2} [1 + (-1)^l] \quad (62)$$

$$R_{\lambda}(a,b;h,c) = \iint \frac{r_{<}^{\lambda}}{r_{>}^{\lambda+1}} [f_a(r)f_c(r) + g_a(r)g_c(r)] [f_b(r')f_h(r') + g_b(r')g_h(r')] dr dr', \quad (63)$$

where  $\xi(l)$  is the parity selection factor and  $R_{\lambda}$  is the radial Coulomb integral with  $f/g$  the upper/lower components of the relativistic spinors.

#### 2.6.2.4 Radiative Width

The radiative width is significantly simpler. The electron-photon interaction that produces radiation is described by the reduced single-particle dipole operator  $\hat{d}$ . As any excited electron can emit a photon, the average radiative width is estimated as the weighted sum of the emission rates from all single particle states  $a$  and  $b$  [40]

$$\Gamma^{(r)} \approx \sum_{a,b} \frac{4\omega_{ba}^3}{3c^3} |\langle a | \hat{d} | b \rangle|^2 \left\langle \frac{n_b}{2j_b + 1} \left( 1 - \frac{n_a}{2j_a + 1} \right) \right\rangle \quad \text{where} \quad \omega_{ba} = \varepsilon_b - \varepsilon_a > 0. \quad (64)$$

Figure 8 below shows the application of the resonant recombintation theory presented in this section to the  $W^{20+}$  system. It is shown to reproduce the experimental data with remarkable accuracy.

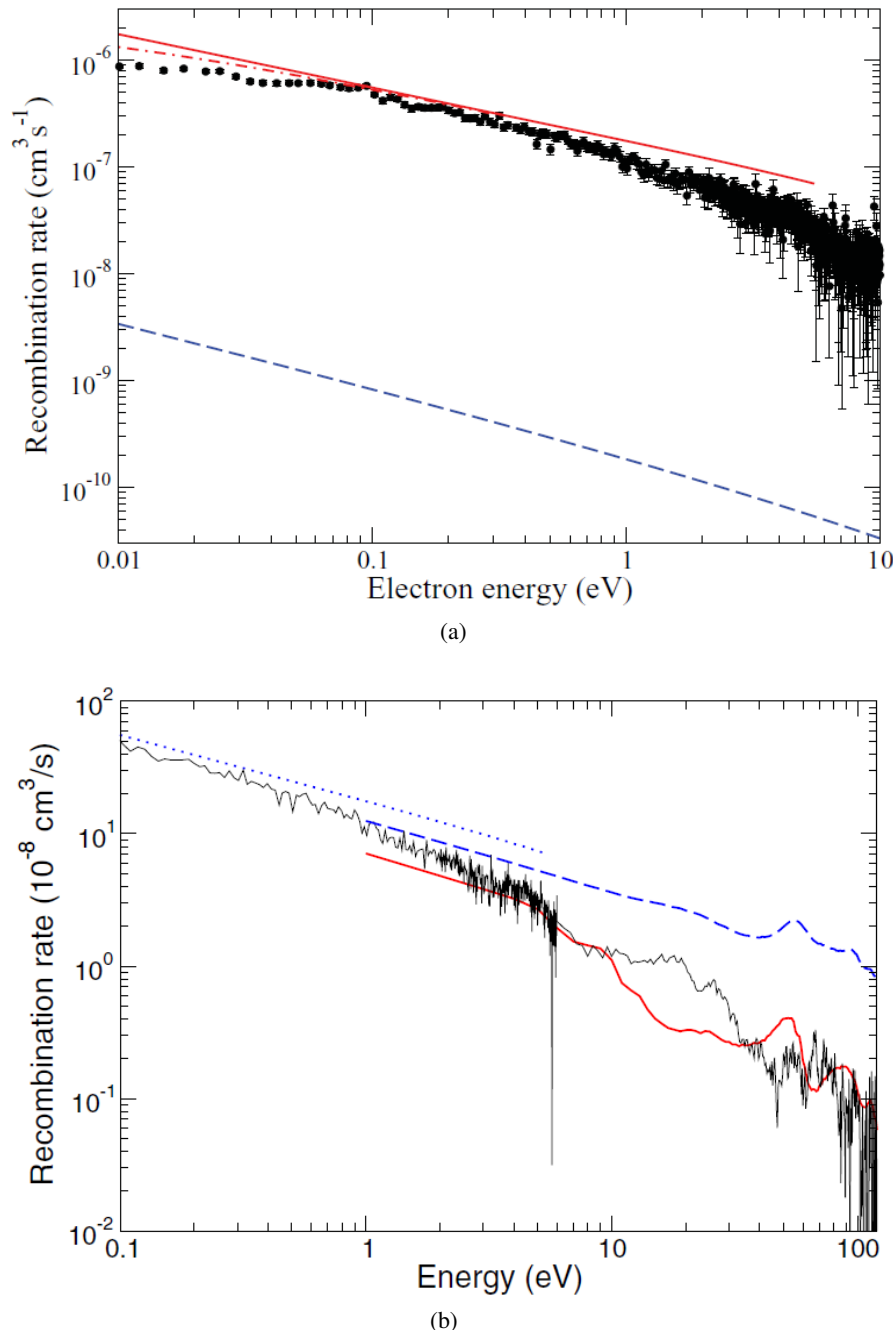


Figure 8. Electron recombination rate of  $\text{W}^{20+}$ . Black line is experimental data from [48]. (a) dashed line is the direct recombination rate from Eq. (43), red line is resonant recombination with unit fluorescence, figure from [14]; (b) dashed blue line is the resonant recombination with unit fluorescence, red line is the resonant recombination with nonunit fluorescence, figure from [42].

## 2.7 Other Atomic Processes

The resonance averaged cross-sections for other atomic processes such as photon scattering, photo-ionisation and electron scattering, can also be obtained using MBQC and doorway states. Considering the coherent amplitude of these processes  $A$ , they can be averaged over small energy intervals containing many resonances to give the resonance averaged amplitude  $\bar{A}$  describing a doorway state. This gives for photon scattering  $X + \gamma \rightarrow X^* + \gamma'$  [42]

$$\overline{A_f^{\gamma\gamma'}} = \sum_d \frac{\langle \Phi_f | \hat{D} | \Phi_d \rangle \langle \Phi_d | \hat{D} | \Phi_i \rangle}{E_i + \omega - E_d + (i/2)\Gamma_{\text{spr}}} ; \quad (65)$$

for photo-ionisation  $X + \gamma \rightarrow X^+ + e^-$

$$\overline{A_f^{\gamma e}} = \sum_d \frac{\langle \Phi_f, \varepsilon | \hat{V} | \Phi_d \rangle \langle \Phi_d | \hat{D} | \Phi_i \rangle}{E_i + \omega - E_d + (i/2)\Gamma_{\text{spr}}} ; \quad (66)$$

and for electron scattering  $X + e^- \rightarrow X^* + e^-$

$$\overline{A_{if}^{ee'}} = \sum_d \frac{\langle \Phi_f, \varepsilon' | \hat{V} | \Phi_d \rangle \langle \Phi_d | \hat{V} | \Phi_i, \varepsilon \rangle}{E_i + \varepsilon - E_d + (i/2)\Gamma_{\text{spr}}} ; \quad (67)$$

where  $\Phi_i$ ,  $\Phi_d$  and  $\Phi_f$  are the initial, intermediate doorway and final state of the atom respectively. The doorway state is a singularly excited state for the photon incident processes, and a doubly excited state for electron incident processes.  $E_i$  and  $E_d$  are the energies of the initial and doorway states, with  $\omega$  and  $\varepsilon$  the energies of the incoming photons and electrons.

From the optical theorem [47] the total cross-section for photon and electron induced reactions can be obtained. The elastic forward scattering amplitude for use in the optical theorem is obtained by setting  $\Phi_f = \Phi_i$ . For the photon induced scattering and ionisation processes, the total cross-section  $\sigma_{\text{tot}}^\gamma$  is

$$\sigma_{\text{tot}}^\gamma \propto \text{Im} \overline{A_i^{\gamma\gamma}} = \frac{1}{2} \sum_d \frac{|\langle \Phi_d | \hat{D} | \Phi_i \rangle|^2 \Gamma_{\text{spr}}}{(E_i + \omega - E_d)^2 + \Gamma_{\text{spr}}^2/4} . \quad (68)$$

The total cross-section  $\sigma_{\text{tot}}^e$  for electron induced processes is

$$\sigma_{\text{tot}}^e \propto \text{Im} \overline{A_i^{ee}} = \frac{1}{2} \sum_d \frac{|\langle \Phi_d | \hat{V} | \Phi_i, \varepsilon \rangle|^2 \Gamma_{\text{spr}}}{(E_i + \varepsilon - E_d)^2 + \Gamma_{\text{spr}}^2/4} . \quad (69)$$

This also includes effects from the electron recombination processes calculated in Section 2.6, with resonant recombination shown to have the same form as Eq. (69). The squared matrix elements in the cross-sections can be evaluated using the radiative and autoionisation widths from Section 2.6.2 as

$$\Gamma^{(r)} \propto |\langle \Phi_d | \hat{D} | \Phi_i \rangle|^2 \quad \text{and} \quad \Gamma^{(a)} \propto |\langle \Phi_d | \hat{V} | \Phi_i, \varepsilon \rangle|^2 , \quad (70)$$

with normalisation conditions returning the constants of proportionality.

## 2.8 Transitions between Atomic States

While the cross-sections for the formation of excited doorway states in highly charged ions have been discussed in Sections 2.6 and 2.7, the wavelengths and associated intensities of the light emitted from these excited states still need to be calculated. In atomic physics, the prominence of a specific transition is calculated and quantified through a property known as the line strength  $S$ . The experimentally observed intensity of a line is directly proportional to this value.

### 2.8.1 Line Strengths

The line strength  $S_{21}$  of a transition between an initial eigenstate  $|\Psi_1\rangle$  with energy  $E_1$  and final eigenstate  $|\Psi_2\rangle$  with energy  $E_2$  is given by the squared matrix element of the single-particle operator  $\hat{M}$

$$S_{21} = |\langle \Psi_2 | \hat{M} | \Psi_1 \rangle|^2, \quad (71)$$

with the resultant photon having energy  $\omega = E_1 - E_2$ . Usually  $S$  is calculated directly in atomic physics codes after performing configuration interaction (CI) calculations. However, an approximate solution for chaotic systems can instead be obtained without intensive computation by using MBQC theory.

MBQC gives a statistical line strength of

$$S_{21} = \overline{|\langle \Psi_2 | \hat{M} | \Psi_1 \rangle|^2} \quad (72)$$

$$= \frac{2J_1 + 1}{3} D_2 \sum_{a,b} |\langle a | \hat{m} | b \rangle|^2 \frac{1}{2\pi} \frac{\Gamma_1 + \Gamma_2}{(\omega_{ba} - \omega)^2 + (\Gamma_1 + \Gamma_2)^2 / 4} \left\langle \frac{n_b}{2j_b + 1} \left( 1 - \frac{n_a}{2j_a + 1} \right) \right\rangle_1, \quad (73)$$

with  $J_1$  the average total momentum of the initial  $|\Psi_1\rangle$  mixed state,  $D_2$  the average level spacing of the final  $|\Psi_2\rangle$  mixed state.  $a$  and  $b$  are the final and initial electron orbitals with single electron transition operator  $\hat{m}$  and transition energy  $\omega_{ba}$  in the single electron basis. The expectation value gives the average occupancy  $n$  of the single electron orbitals  $a$  and  $b$ , weighted by the total angular momentum of the orbitals  $j$ , in the vicinity of the initial state.  $\Gamma_1$  and  $\Gamma_2$  are the spreading widths of  $|\Psi_1\rangle$  and  $|\Psi_2\rangle$  respectively. A derivation of Eq. (73) is provided in Section 5.1. It is also noted that, to the best of our knowledge, this theory has not previously been implemented and compared to experimental results.

### 2.8.2 Einstein Coefficients

Once the line strength  $S_{21}$  is known, the rate of the transition  $|\Psi_1\rangle \rightarrow |\Psi_2\rangle$  can be determined using the Einstein coefficient for spontaneous emission  $A_{12}$ . For electric dipole (E1) transitions [49, 50]

$$A_{12} = \frac{16\pi^3}{3h\varepsilon_0\lambda^3} \frac{S_{21}}{g_1}, \quad (74)$$

where  $h$  is Planks constant,  $\varepsilon_0$  is the permittivity of free space,  $\lambda$  is the wavelength of light, and  $g_1$  is the statistical weight of state  $|\Psi_1\rangle$ . Note that this equation differs for higher order transitions such as magnetic dipole (M1) and electric quadrupole (E2) transitions. In customary units ( $A$  in  $s^{-1}$ ,  $\lambda$  in Å,  $S$  in a.u., and  $\omega$  in eV)

$$A_{12} = \frac{2.0261 \times 10^{18}}{\lambda^3} \frac{S_{21}}{g_1} = 1.0608 \times 10^6 \times \omega^3 \frac{S_{21}}{g_1}. \quad (75)$$

### 2.8.3 Observed Intensity

The total intensity of the emitted light per steridian (sr, unit solid angle) from a given source due to the  $|\Psi_1\rangle \rightarrow |\Psi_2\rangle$  transition is given by [49, 50]

$$I_{12} = \frac{N_1 A_{12} \omega}{4\pi}, \quad (76)$$

with  $N_1$  being the number of atoms in source that are in the  $|\Psi_1\rangle$  excited state. For a given plasma,  $N_1$  is determined using the theory of Sections 2.6 and 2.7. However, if the plasma is assumed to be in local thermal equilibrium (LTE), the distribution of occupied states can instead be determined through use of the Boltzmann distribution [9, 49]

$$\frac{N_1}{N_T} = \frac{1}{Z} g_1 \exp\left(-\frac{E_1}{k_B T}\right) \quad (77)$$

$$Z = \sum_i g_i \exp\left(-\frac{E_i}{k_B T}\right). \quad (78)$$

Here  $N_T$  is the total number of atoms in the source,  $E$  is the energy of the excited states,  $k_B$  is Boltzmann's constant,  $T$  is the temperature of the plasma, and  $Z$  is the partition function. This is not an unreasonable assumption, as it has recently been shown by Sheil and Versolato [51] that a population in a non-LTE tin plasma (at  $k_B T = 36$  eV) can be accurately predicted by using a LTE plasma at a lower temperature ( $k_B T = 26$  eV).  $k_B$  is set to 1 for the rest of this thesis such that temperature has units eV.

The total intensity of light for the transition is

$$\frac{I_{12}}{N_T} = \frac{1.0608 \times 10^6}{4\pi} \frac{1}{Z} \exp\left(-\frac{E_1}{T}\right) \omega^4 S_{21}, \quad (79)$$

and the total spectrum of light emitted from the plasma is

$$\sum_{i,j} I_{ij}. \quad (80)$$

### 3 Verification of MBQC in Highly Charged Tin Ions

Using the atomic code AMBiT [52], the Hamiltonians for all  $J^\pi$ 's of the  $\text{Sn}^{7+} - \text{Sn}^{14+}$  systems have been calculated and investigated for the presence of MBQC. All configurations with electron excitations up to the  $5g$  valence shell, and with average energy less than a given energy threshold  $E_{th}$ , were included in the calculations. The systems all had a frozen  $3spd$  core, with  $E_{th}$  always remaining below the energy that would unfreeze the  $3d$  core shell.

As the tin systems have open  $d$  shells, as opposed to the open  $f$  shells of studied Au and W highly charged ions, there are fewer energy levels and the tin systems are significantly smaller in matrix size. While these systems will be shown to be chaotic, they are also small enough to be calculated on a standard home computer and can be readily decomposed into their exact eigenstates with reasonable accuracy. As a result, the energy levels and spacings of the systems are considered exactly and the level density formula of Section 2.5 is not utilised at this stage.

#### 3.1 Verification of Wigner's Surmise and Distributed Eigencomponents

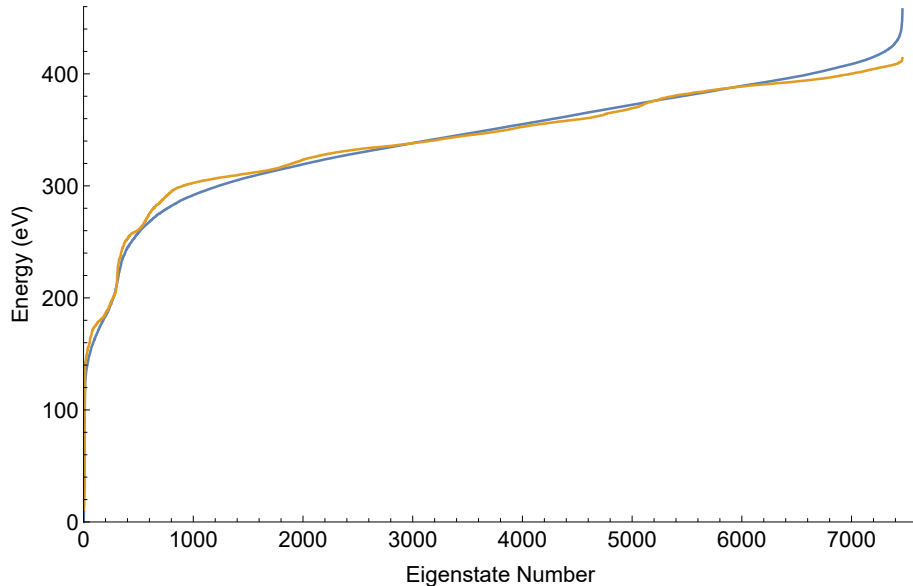
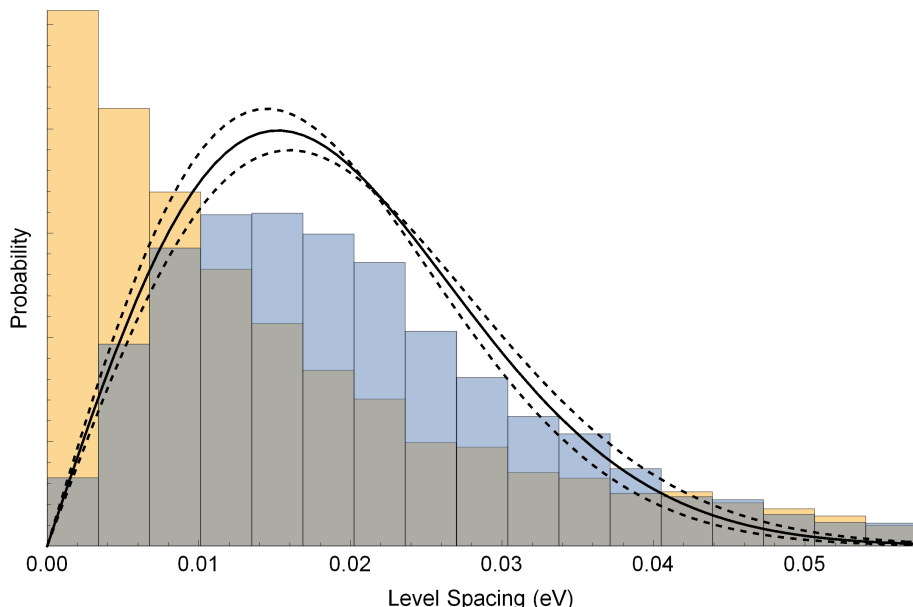
The analysis of MBQC in the  $\text{Sn}^{13+}$  system with  $J^\pi = 1/2^-$  at an energy of  $E_{th} = 17$  a.u. is shown in detail below, with MBQC values surmised in Table 1. Figure 9 shows the diagonal elements of the Hamiltonian  $H_{ii}$  and energy eigenvalues  $E_i$  in ascending order for all 7464 eigenstates of momenta and parity  $J^\pi = 1/2^-$ . All energies have been offset by the first eigenvalue such that  $E_0 = 0$ . Figure 10 shows the NNS distributions of the  $H_{ii}$  and  $E_i$  elements of the same system, with the  $E_i$  elements fitted to Wigner's surmise to extract the average level spacing  $D$ . It is found that the ratio of the RMS residual coupling interaction  $V$  (given by Eq. (23), repeated below) to the average level spacing  $D$ , is much greater than 1, indicating that the system is chaotic. Matching the NNS distribution to Wigner's surmise also demonstrates that the Hamiltonian can be described using GOE statistics. This particular  $J^\pi$  is representative of all  $J^\pi$  in  $\text{Sn}^{7+} - \text{Sn}^{14+}$ .

$$V^2 = \frac{1}{N^2} \sum_{\mu \neq \nu} H_{\mu\nu}^2. \quad (23)$$

To further confirm the applicability of MBQC, the wave-function coefficients of the eigenstates were analysed. The 2200<sup>th</sup> eigenstate of  $J^\pi = 1/2^-$  in  $\text{Sn}^{13+}$  was selected randomly and is representative of all eigenstates within the tin ions. The wave-function coefficients of this eigenstate are shown in Fig. 11a with its squared components fitted to a Lorentzian in Fig. 11b. These figures clearly agree with the theoretical distributions that are characteristic of MBQC. Furthermore, the values of the characteristic spreading width obtained from Wigner's surmise and the Lorentzian fitting agree with each other. This provides a strong consistency check for the strong basis mixing within the eigenstates of tin.

Table 1. MBQC chaos parameters for  $\text{Sn}^{13+}$ ,  $J^\pi = 1/2^-$  at the energy threshold  $E_{th} = 17$  a.u.

$V$ (eV)	$D$ (eV)	$V/D$	$\Gamma_{\text{spr}}$ (eV)	
			From Wigner Surmise	From Lorentzian Distribution
0.2496	$0.019 \pm 0.001$	13.085	$20.52 \pm 1.08$	21.59


 Figure 9. Ordered eigenstates of  $\text{Sn}^{13+}$  with  $J^\pi = 1/2^-$ . Orange shows the diagonal elements of the Hamiltonian  $H_{ii}$ . Blue shows the corresponding energy eigenvalues  $E_i$ .

 Figure 10. NNS distribution for  $\text{Sn}^{13+}$  with  $J^\pi = 1/2^-$ . Orange shows level spacing for the diagonal Hamiltonian elements  $H_{ii}$  and is seen to obey a Poissonian distribution as expected. Blue shows level spacing for energy eigenvalues  $E_i$ . Black line shows the fitted Wigner Surmise. Dotted black line shows  $1\sigma$  deviation of the fit.

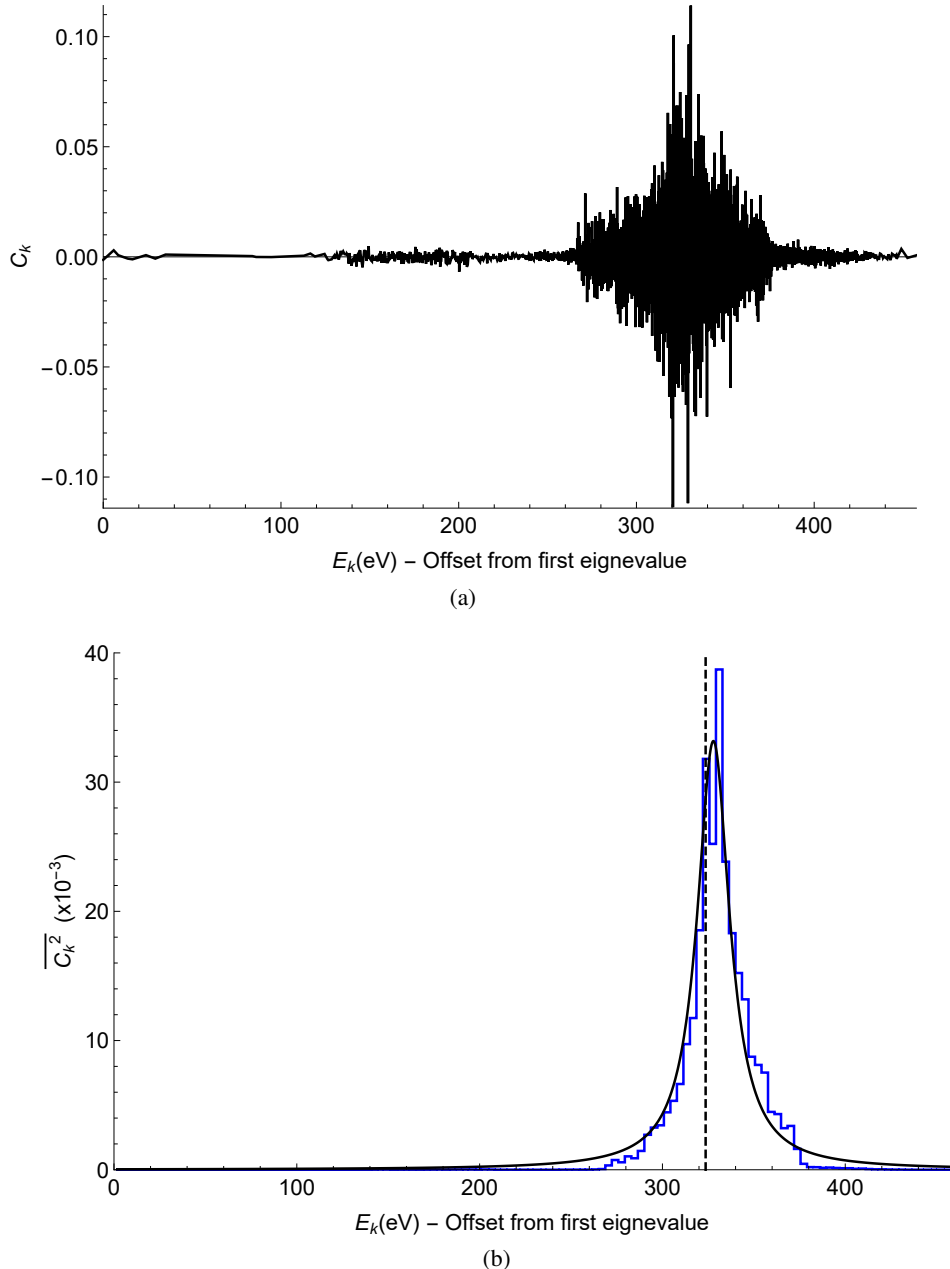


Figure 11. Components of the 2200<sup>th</sup> eigenstate  $J^\pi = 1/2^-$  for  $\text{Sn}^{13+}$ ; (a) shows the  $C_k$  components, (b) shows the histogram of the averaged squared components  $\overline{C_k^2}$  (blue line) fitted to a Lorentzian (black line) with  $\Gamma_{\text{spr}} = 21.59 \text{ eV}$ . Dashed black line shows the energy of the 2200<sup>th</sup> eigenstate  $E_{2200} = 323.63 \text{ eV}$ .

### 3.2 Trends in MBQC Properties

Summaries of the MBQC parameters for all the tin systems at the maximum energy threshold that could be handled by my computer (i.e. matrices that did not exceed 2 GB in size) are presented in Fig. 12. These include the values of the residual interaction  $V$ , the average level spacing  $D$  as obtained by fitting the NNS distribution to Wigners surmise, the ratio  $V/D$ , and the spreading width  $\Gamma_{\text{spr}}$ . As  $V/D \gg 1$  for all systems, the tin highly charged ions are clearly chaotic and display the features of MBQC. As such, statistical theories such as doorway states are applicable to the tin systems.

Firstly, it can be clearly seen that MBQC properties can have differing values for the even (black) and odd (blue)  $\pi$  of the same  $J$ . While  $V$  remains approximately the same for both parities,  $D$  can vary greatly in either direction with even parities having smaller, greater or the same level spacing as odd parities. This propagates to the other parameters which are dependent on  $D$ . This will be discussed in detail in Section 4.5.

It is noted here though, that the shape of the level spacing is a direct reflection of the level density as a function of momenta  $\rho_{J\pi}$  (see Eq. (48)) as  $D = \rho^{-1}$ . More levels are present for lower  $J$  due to the combinatorics of the available energy levels, with more levels resulting in a narrower level spacing. The ratio  $V/D$  also follows the inverse trend of  $D$  and is much larger for smaller  $J$ . This is a consequence of the narrower energy spacings. With narrower spacings, it is easier to interact with — and alter — more levels. The system becomes more chaotic as shown by the higher ratio. While this trend is not as pronounced in  $\Gamma_{\text{spr}}$ , it is still seen that for lower  $J$  where there are more levels,  $\Gamma_{\text{spr}}$  is larger (and roughly the same value). As there are more levels closer together, the interaction can propagate further.

From these graphs it is also seen that for the largest values of  $J$ , the parameters can significantly deviate from the observed trend and/or have very large errors. This is due to these momenta having relatively few contributing levels of less than  $\sim 20$ , compared the  $10^3$ – $10^5$  levels that occur in the lower  $J$ 's. As a result MBQC has not fully developed in these parts of the system as illustrated by  $V/D$  being close to or less than 1. However, as more configurations are added with increasing energy threshold, more levels with larger  $J$  will become available and MBQC properties for these momenta will become more fully developed. Furthermore it is expected that for very high energies, MBQC properties, in particular  $\Gamma_{\text{spr}}$ , will be constant across all  $J^\pi$ , i.e.:

$$\lim_{E_{th} \rightarrow \infty} \Gamma_{\text{spr}}(J^\pi) = \Gamma_{\text{spr}}. \quad (81)$$

It is worth noting, that for practical purposes, the fact that these higher  $J$  states are not chaotic to the same extent as lower  $J$  states is not significant. These large  $J$  have considerably fewer constituent states, and as a result contribute to only a tiny minority of the total amount of levels and transition lines within the entire system.

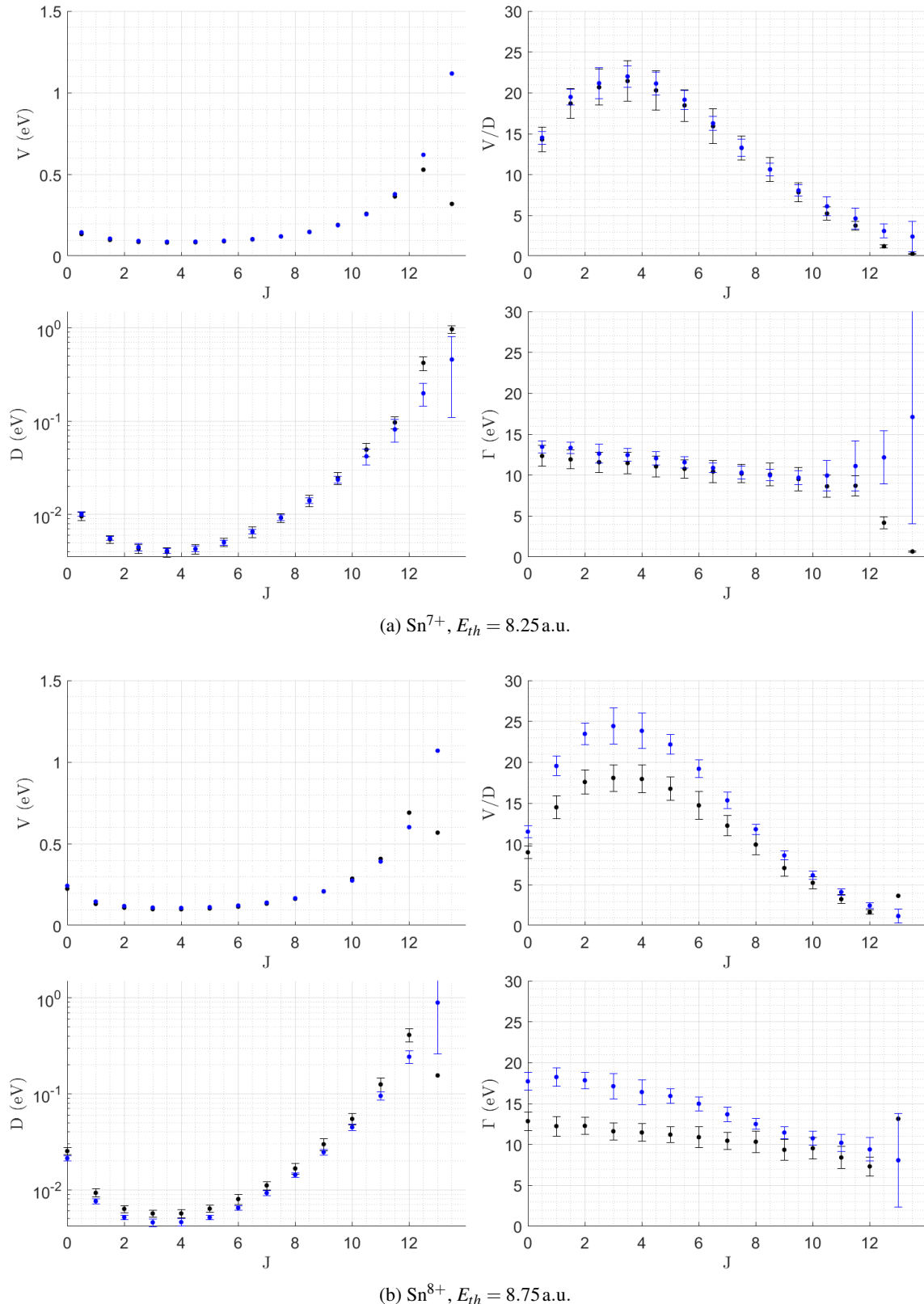


Figure 12. MBQC parameters for highly charged tin ions. The residual interaction  $V$ , average level spacing  $D$ , ratio  $V/D$ , and spreading width  $\Gamma_{\text{spr}}$  are plotted for a given configuration energy threshold  $E_{th}$ . Errors estimated from  $1\sigma$  curve fitting of  $D$  in Wigner's surmise. (a)–(h) show properties for  $\text{Sn}^{7+}$ – $\text{Sn}^{14+}$  respectively. Black shows even parity, blue shows odd parity.

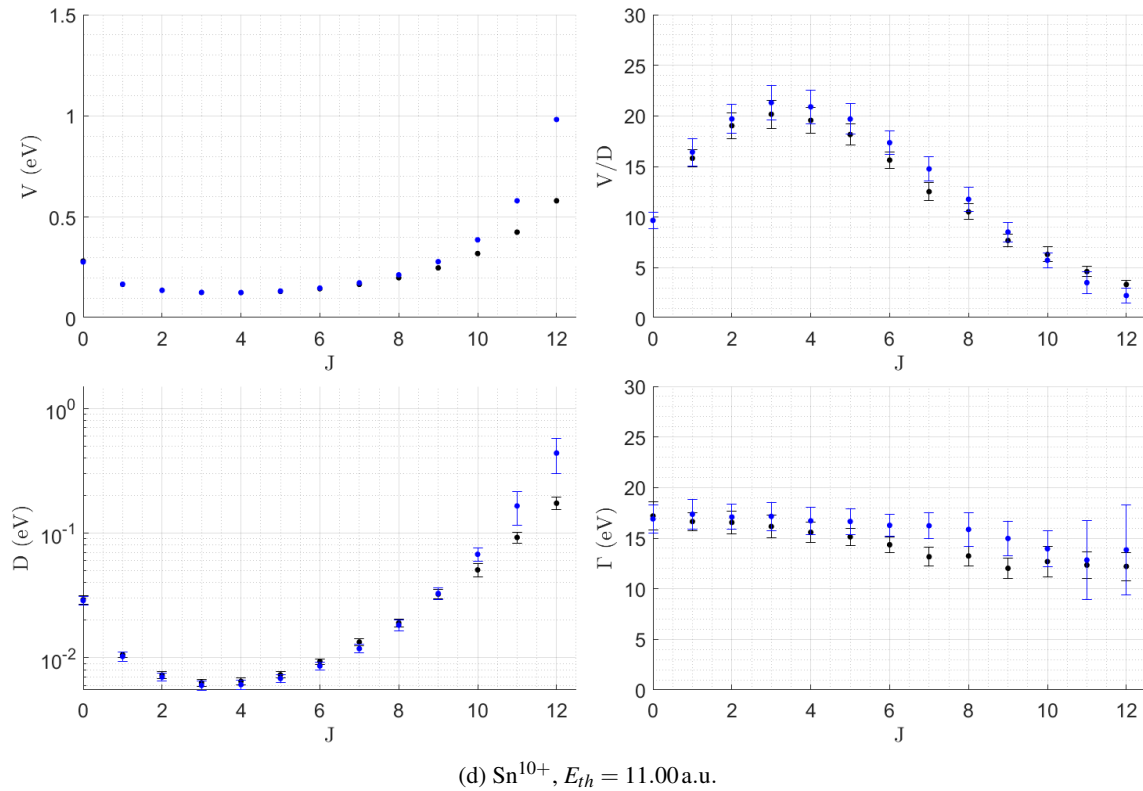
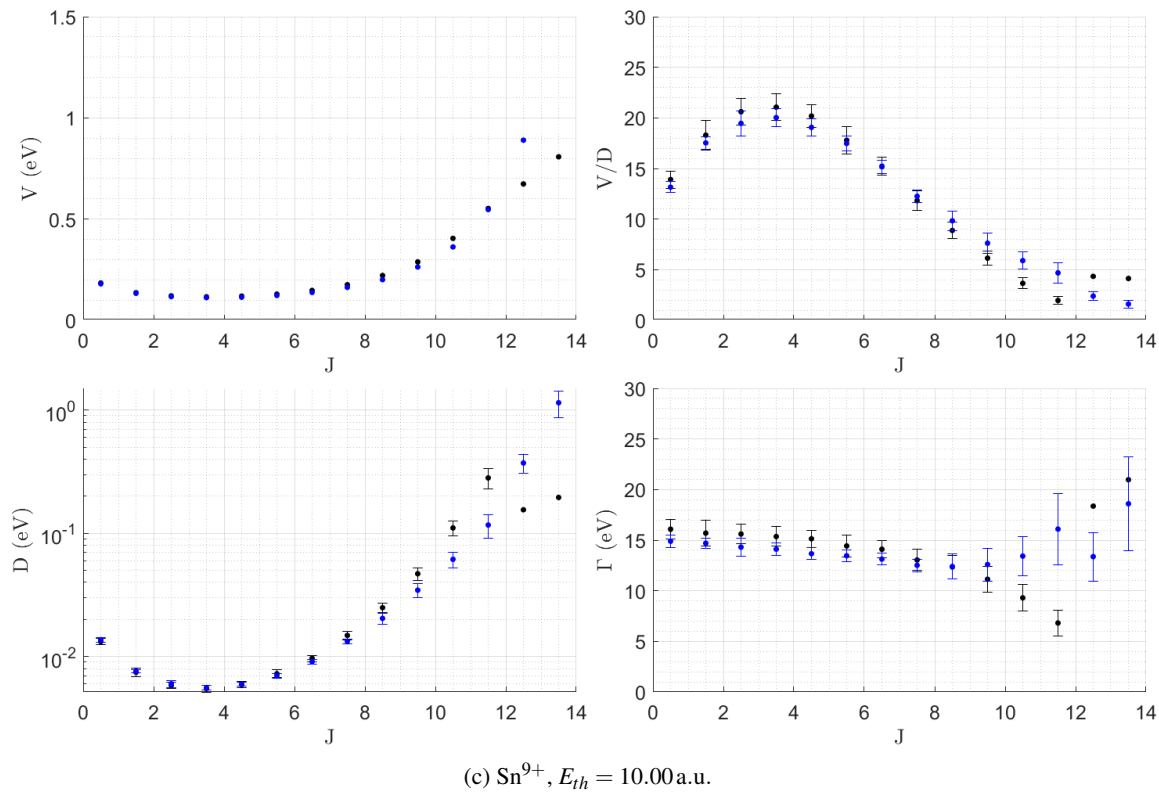


Figure 12. MBQC parameters for highly charged tin ions continued.

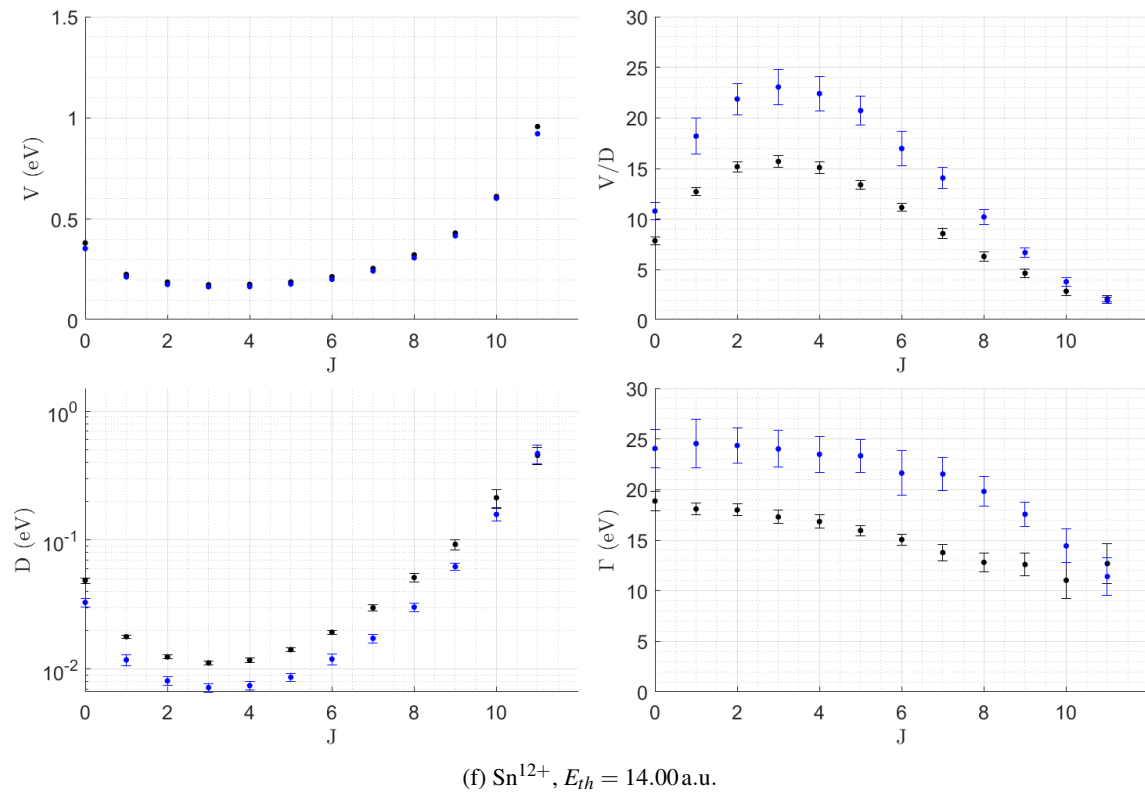
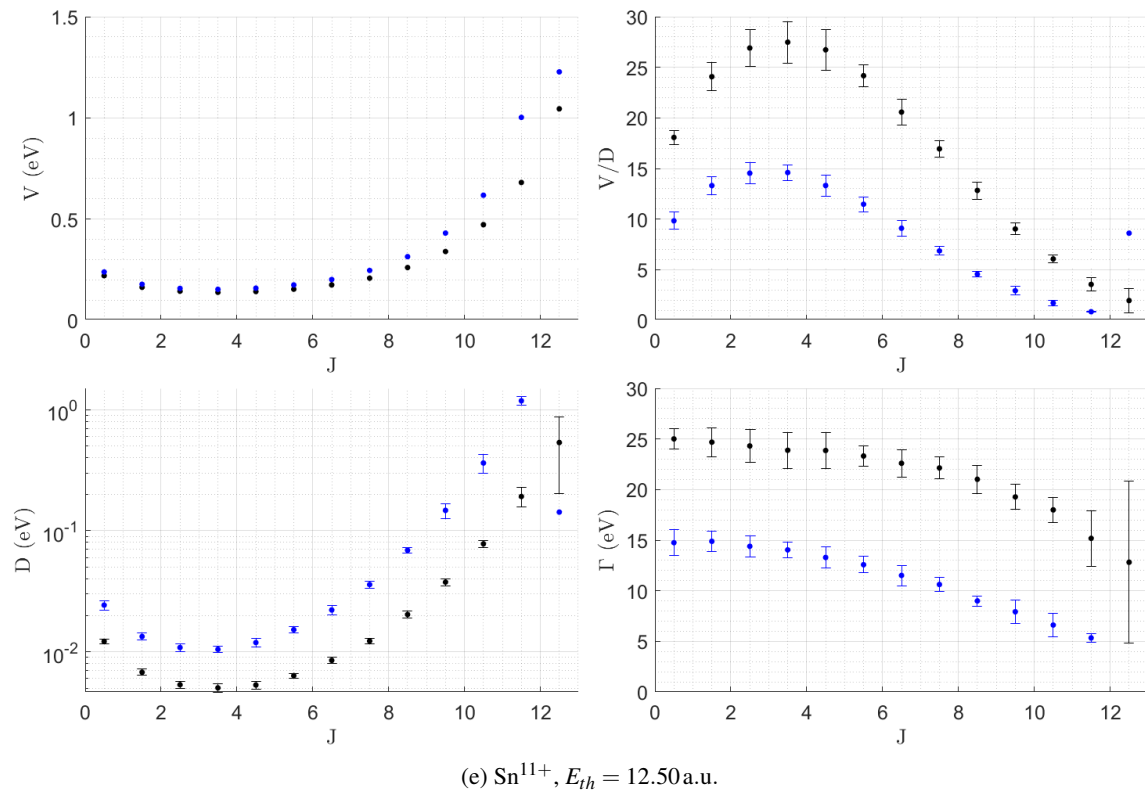


Figure 12. MBQC parameters for highly charged tin ions continued.

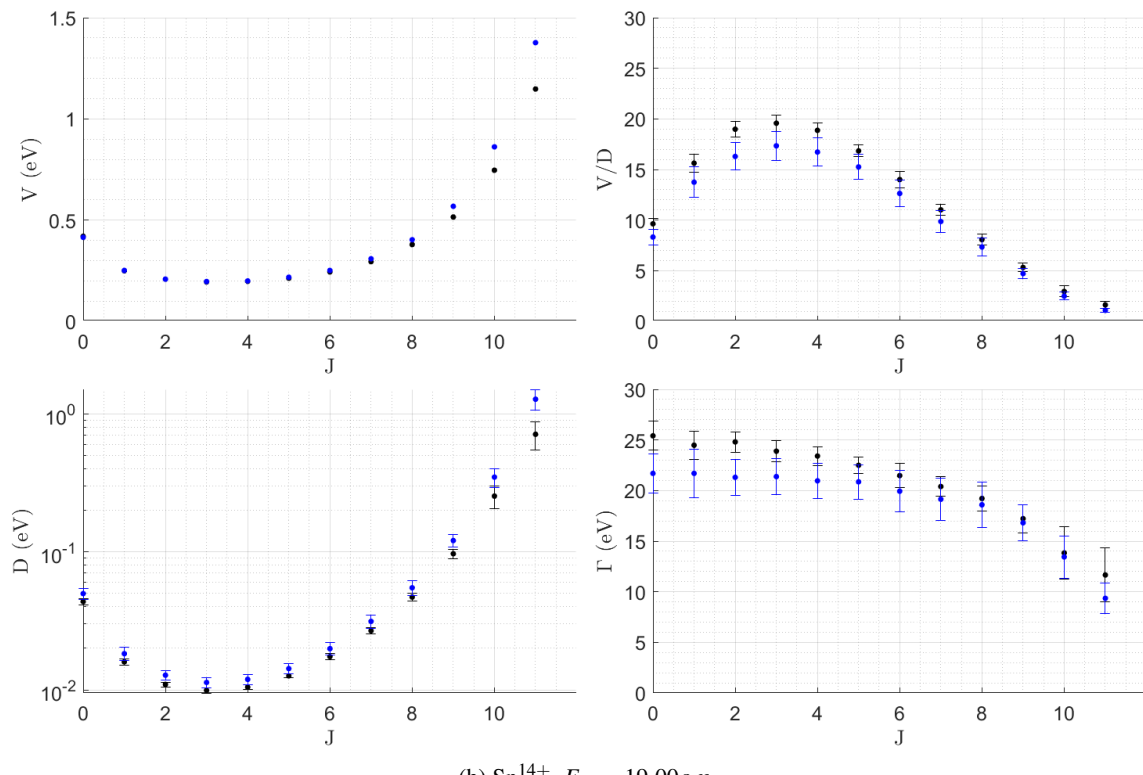
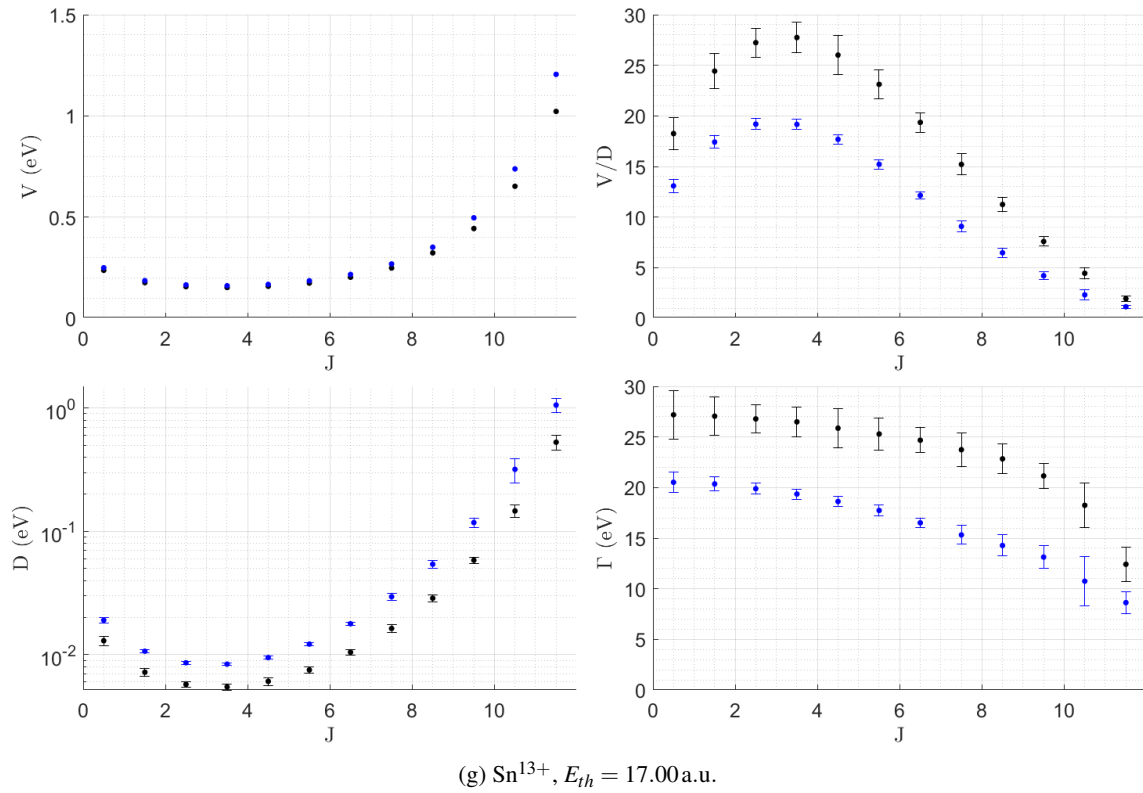


Figure 12. MBQC parameters for highly charged tin ions continued.

While Fig. 12 shows how the MBQC properties of the highly charged tin ions vary with  $J^\pi$ , Fig. 13 below shows how the properties change with increasing energy threshold.  $\text{Sn}^{13+}$  has been used as an illustrative example. The weighted mean of the properties for all  $J^\pi$ 's at a given  $E_{th}$ , with respect to the total number of states in each  $J^\pi$ , has been plotted.

From these graphs it is first seen that the ratio  $V/D$  grows with increasing energy, indicating that the system becomes more chaotic. This is expected as more states are included in the Hamiltonian with increasing energy, resulting in more interactions and mixing within the system. Secondly, the log plots show that the average level spacing  $D$ , and squared residual interaction  $V^2$ , decay exponentially with energy. The reasoning for this will be explained in depth in Sections 4.1 and 4.2 respectively. Finally, it is seen that the spreading width is approximately constant at higher energies where MBQC is fully developed. This matches with the observations in  $\text{Au}^{24+}$  [33] and agrees with the model that will be developed in the following section, Section 4.

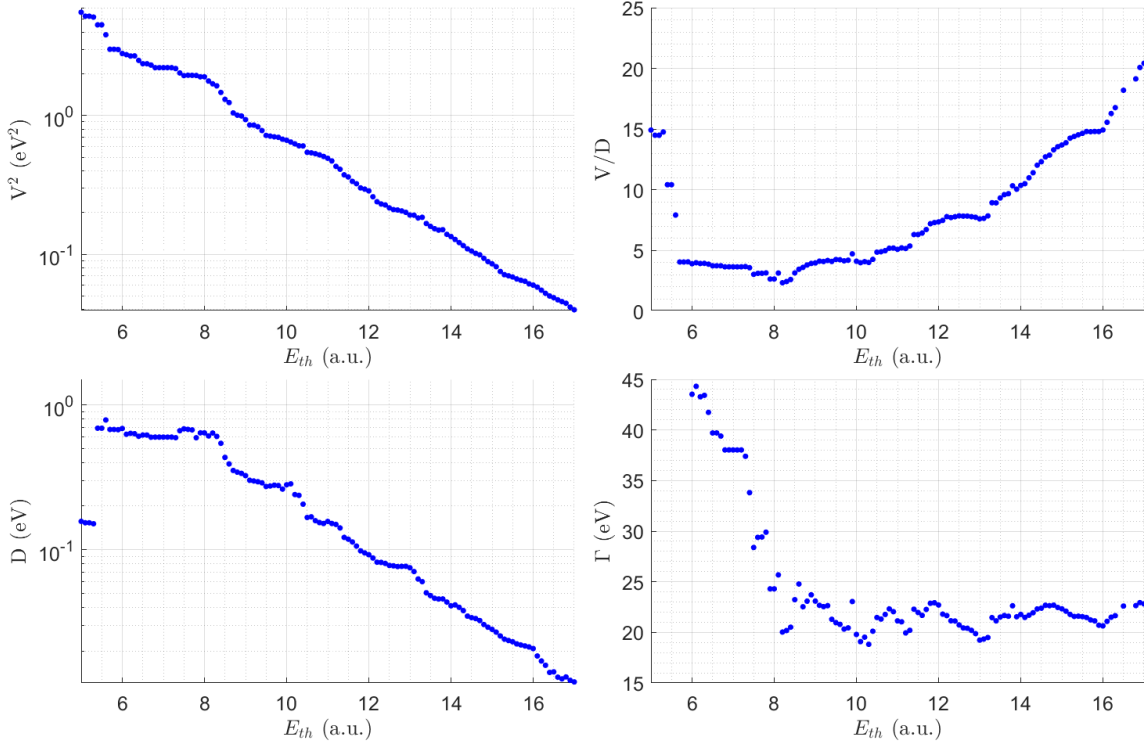


Figure 13. Average MBQC parameters for  $\text{Sn}^{13+}$  as a function of energy threshold  $E_{th}$ . Data points show the average value obtained from all  $J^\pi$ 's in the system at the given energy threshold, weighted by the total number of states in each  $J^\pi$ .

## 4 Model for Spreading Width

Section 3 only considered MBQC in tin systems at a single energy level. This section will seek to develop a model for how the  $\Gamma_{\text{spr}}$  parameter of MBQC evolves as a function of energy in atomic systems, remembering that

$$\Gamma_{\text{spr}} = \frac{2\pi V^2(E)}{D(E)} = 2\pi V^2(E)\rho(E).$$

### 4.1 Overview of the Atomic Hamiltonian

The energy level density as a function of energy  $\rho(E)$  of an atomic system is known to increase exponentially [28, 53]

$$\rho(E) = \frac{dN}{dE} \propto \exp\left(\frac{E}{\varepsilon_\rho}\right) \quad (82)$$

$$D(E) = \frac{1}{\rho(E)} \propto \exp\left(-\frac{E}{\varepsilon_\rho}\right). \quad (83)$$

where  $N$  is the number of energy levels,  $D$  is the average energy level spacing and  $\varepsilon_\rho$  is the level growth constant. This exponential decay in average level spacing can be seen in Fig. 13.

A model for the trend in  $V^2(E)$  will now be developed for atomic systems using the general structure of the atomic Hamiltonian. By dividing the Hamiltonian into blocks of interactions where the interacting configurations differ by 0, 1 or 2 electrons, the residual interaction can be separated into three components:  $V^{(0)}$ ,  $V^{(1)}$ , and  $V^{(2)}$ . Combinatorics is used to count the average number of blocks that contribute to each of these cases. Through also including how the number of configurations within the Hamiltonian increases with energy, a relation for how  $V^2$  depends  $E$  is established.

An atomic Hamiltonian  $H$  with  $N^2 \propto \rho^2$  elements can be split into blocks of self-configurations  $C_i$  along the diagonal for configuration state functions (CSFs) that correspond to each relativistic configuration, and blocks of interactions  $C_{ij}$  elsewhere. This is illustrated in Fig. 14. The  $C_i$  blocks have  $m_i^2$  many elements, where  $m_i$  is the number of CSFs in the configuration  $C_i$ , while the  $C_{ij}$  blocks have  $m_i m_j$  elements.

For a Hamiltonian that includes  $M$  configurations

$$N = \sum_{i=1}^M m_i, \quad \text{with } m_i \ll N \quad \text{for large } N. \quad (84)$$

It is also empirically observed that in the tin systems (see Fig. 15), the total number of configurations  $M$  increases via a power law with

$$M(E) = a_M E^b, \quad (85)$$

where  $a_M$  and  $b$  are constants.

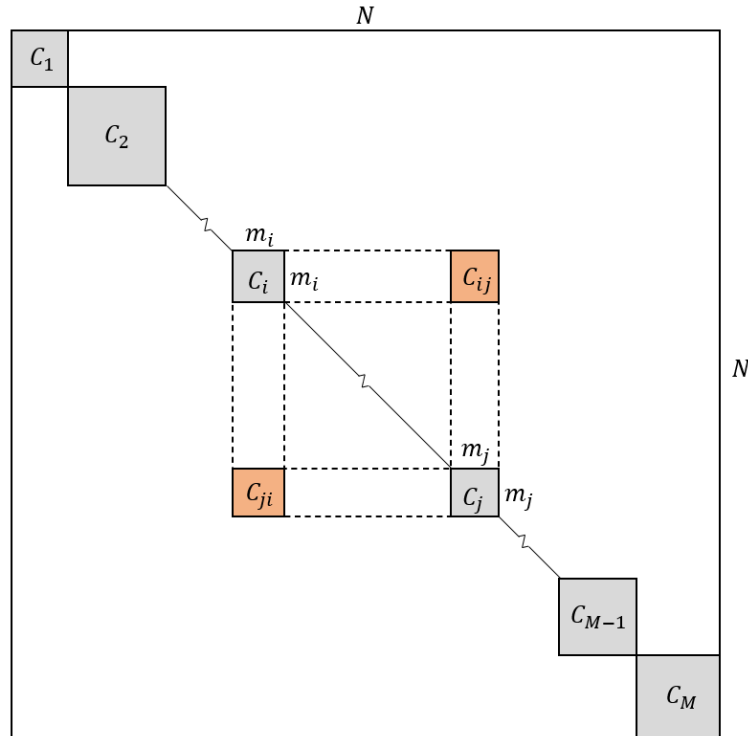
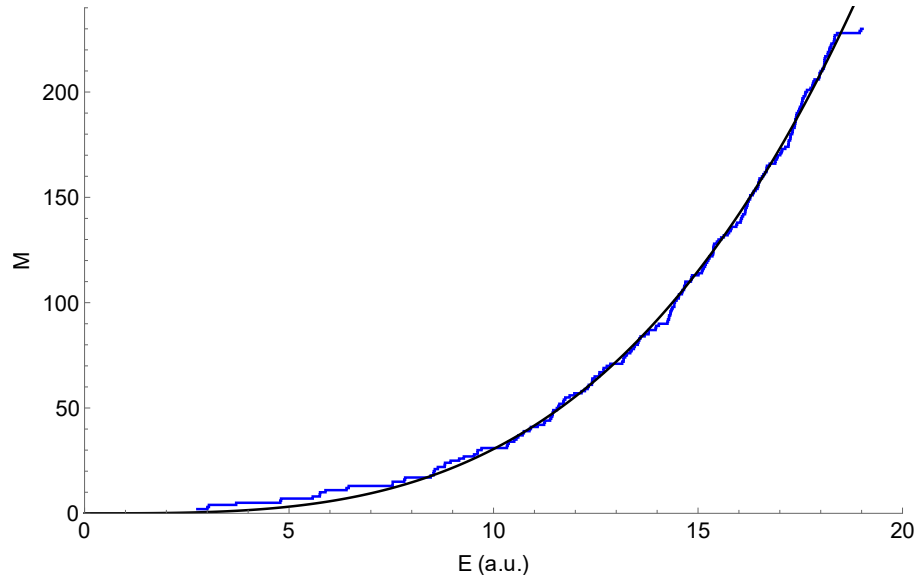


Figure 14. Hamiltonian matrix diagram for atomic systems.

Figure 15. Energy vs number of configurations  $M$  for  $\text{Sn}^{13+}$ . Blue shows cumulative number of configurations  $M$  at each energy. Black shows power law fitting to the function  $M(E) = a_M E^b$  with  $a_M = 0.0163$ ,  $b = 3.27$  and  $R^2 = 0.9995$ . In general for the Sn systems,  $a_M \sim 0.01$  and  $b \sim 3-4$ .

## 4.2 Self-configuration Blocks

The zeroth order contribution to the residual interaction  $V^{(0)}$  due to the self-configuration blocks  $C_i$  along the diagonal of the matrix are considered first. It is assumed that these blocks have an RMS value of  $A^{(0)}$ . As  $m_i \ll N$ , the elements in  $C_i$  are localised near the main diagonals with  $\mu \approx v$ . There are hence of order  $N$  non-zero elements  $H_{\mu v}$  due to the self configuration blocks. Remembering the definition

$$V^2 = \frac{1}{N^2} \sum_{\mu \neq v} H_{\mu v}^2, \quad (23)$$

the zeroth order interaction is

$$V^{(0)2} = \frac{1}{N^2} \sum_{\mu \approx v}^N A^{(0)2} \quad (86)$$

$$= \frac{1}{N^2} N A^{(0)2} \quad (87)$$

$$= \frac{1}{N} A^{(0)2} \quad (88)$$

$$\propto \rho^{-1} = \exp\left(-\frac{E}{\varepsilon_\rho}\right). \quad (89)$$

The exponential decay of this zeroth order, principle contribution to  $V^2$ , agrees well with the observations that were made in Fig. 13 where  $V^2$  was plotted against  $E$ .

## 4.3 Interaction Blocks

It is well known that when calculating atomic Hamiltonians using 2 body interactions, the interaction blocks  $C_{ij}$  are zero if the configurations  $C_i$  and  $C_j$  differ by more than 2 electrons. The first ( $V^{(1)}$ ) and second ( $V^{(2)}$ ) corrections to the interaction can hence be obtained by separately considering the situations where the configurations differ by one or two electrons respectively.

It is assumed that each configuration has  $v$  valence electrons and is constructed by randomly selecting single electron shells  $nl$  with,  $g = 2(2l + 1)$  allowed repetitions such that there is a total of  $p$  possible shells to select from.

### 4.3.1 One-differing Electron

For a given Hamiltonian  $H$  containing  $(M - 1)$  configurations, there are  $\binom{p}{v} - (M - 1)$  possible combinations from which a new configuration  $C_M$  can be added to  $H$ . For a chosen configuration  $C_i$ , there are on average  $v(p - v)$  configurations that differ to it by one electron. The probability  $\Pr(C_M | C_i)$  that  $C_M$  differs to  $C_i$  by one electron is

$$\Pr(C_M | C_i) = \frac{v(p-v)}{\binom{p}{v} - i}. \quad (90)$$

The probability  $\Pr(C_M^{(1)})$  that  $C_M$  differs to any of the other configurations by one electron is

$$\Pr(C_M^{(1)}) = \sum_{i=1}^{M-1} \Pr(C_M | C_i) \quad (91)$$

$$= \sum_{i=1}^{M-1} \frac{v(p-v)}{\binom{p}{v} - i} \quad (92)$$

$$\approx \sum_{i=1}^{M-1} \frac{v(p-v)}{\binom{p}{v}} \quad \text{as} \quad \binom{p}{v} \gg i \quad \forall i \in [1, M-1] \quad (93)$$

$$= \frac{v(p-v)}{\binom{p}{v}} (M-1). \quad (94)$$

The probability  $\Pr(C^{(1)})$  that any two configurations in the entire matrix differ by one electron is

$$\Pr(C^{(1)}) = \sum_{i=2}^M \Pr(C_i^{(1)}) \quad (95)$$

$$= \sum_{i=2}^M \frac{v(p-v)}{\binom{p}{v}} (i-1) \quad (96)$$

$$= \frac{v(p-v)}{\binom{p}{v}} \frac{(M-1)(M-2)}{2} \quad (97)$$

$$\approx \frac{v(p-v)}{\binom{p}{v}} \frac{M^2}{2}. \quad (98)$$

There are  $M(M-1)$  interaction blocks in  $H$ , so the total number of blocks  $C^{(1)}$  in  $H$  that differ by 1 electron is

$$C^{(1)} = M(M-1)\Pr(C^{(1)}) \quad (99)$$

$$\approx M^2 \frac{v(p-v)}{\binom{p}{v}} \frac{M^2}{2}. \quad (100)$$

If the blocks differing by one electron have an RMS value of  $A^{(1)}$ , the first correction  $V^{(1)}$  is

$$V^{(1)2} = \frac{1}{N^2} \sum_{i \neq j} C_{ij}^2 \quad (101)$$

$$= \frac{1}{N^2} C^{(1)} A^{(1)2} \quad (102)$$

$$= \frac{1}{N^2} M^2 \frac{v(p-v)}{\binom{p}{v}} \frac{M^2}{2} A^{(1)2} \quad (103)$$

$$\propto \frac{M^4}{N^2} \quad (104)$$

$$\propto E^{4b} \exp\left(-\frac{2E}{\epsilon_\rho}\right). \quad (105)$$

### 4.3.2 Two-differing Electrons

It can be shown that for a chosen configuration  $C_i$  there are  $v(p-v)(v-1)(p-v-1)/4$  possible configurations that differ from it by two electrons. Through the same rationale as above, the number  $C^{(2)}$  of two electron differing blocks  $C_{ij}$  in  $H$  is

$$C^{(2)} \approx M(M-1) \frac{v(p-v)(v-1)(p-v-1)}{4 \binom{p}{v}} \frac{M^2}{2}, \quad (106)$$

and assuming they have an RMS value  $A^{(2)}$ , the second correction  $V^{(2)}$  is

$$V^{(2)2} = \frac{1}{N^2} \frac{v(p-v)(v-1)(p-v-1)}{8 \binom{p}{v}} M^4 A^{(2)2} \quad (107)$$

$$\propto E^{4b} \exp\left(-\frac{2E}{\epsilon_\rho}\right). \quad (108)$$

Note that as  $E$  increases, the number of single electron states  $p$  should also increase (i.e. higher principal shells  $n$  should be added), but this will change much slower than  $M$  and is hence neglected. Furthermore for very high energies, such as in the continuum, the total number of possible states is infinite and the corrections approach 0.

### 4.3.3 Magnitude of the Corrections

The corrections to  $V^2$  grow rapidly and have very sharp peaks due to the large  $4b$  power of  $E$  (of order 12–16) and small  $\epsilon_\rho$  exponential decay constant (of order 1–2 a.u.). This sharp peak however is heavily suppressed by the coefficients of this energy relation. Considering the One-differing electron case in Section 4.3.1, the coefficient is shown to be very small:

$$\frac{v(p-v)}{\binom{p}{v}} A^{(1)2} = v(p-v)/\frac{p!}{v!(p-v)!} A^{(1)2} \quad (109)$$

$$= \frac{vv!(p-v)}{p(p-1)(p-2)\dots(p-v+1)} A^{(1)2} \quad (110)$$

$$\approx \frac{vv!}{p^{v-1}} \quad \text{as } p \gg v > 1 \quad \text{and } A^{(1)} \text{ is of order unity} \quad (111)$$

$$\lll 1. \quad (112)$$

As a numerical example, for  $v = 9$  (the number of valence electrons in  $\text{Sn}^{13+}$ ) and  $p = 82$  (the total number of orbitals in the  $n = 4$  and  $n = 5$  shells), a coefficient of order  $10^{-9}$  is obtained. Furthermore, the coefficient of  $M(E)$ ,  $a_M$  is of order 0.01, so an additional factor of  $10^{-8}$  is present in  $V^2$  due to the  $M^4$ . This gives a total coefficient magnitude of  $10^{-17}$ . On the other hand, the maximum value of  $E^{4b} \exp(-E/\epsilon_\rho)$  for  $\text{Sn}^{13+}$  with  $b = 3.27$  and  $\epsilon_\rho = 1.78 \text{ a.u.}$  is of order  $10^{12}$ . Therefore the first correction  $V^{(1)2}$  has size  $10^{-5}$  and does not significantly contribute to the total value of  $V^2$  in the tin system.

For the Two-differing electron case in Section 4.3.2, the additional factor of  $(v-1)(p-v-1)$  will increase the second order coefficient by a few orders of magnitude. This however will be offset by a smaller RMS interaction  $A^{(2)}$ , as typically the greater the difference between configurations, the weaker the interactions. Note that while these interaction strengths  $A^{(2)}$  are weaker, they are still greater than the average level spacing, and MBQC is still applicable. The magnitudes of the first and second corrections to  $V$  are heavily suppressed by the coefficients.

#### 4.4 A Spreading Width Model

The spreading width  $\Gamma_{\text{spr}}$  can be separated into the three separate contributions

$$\Gamma_{\text{spr}} = \Gamma_{\text{spr}}^{(0)} + \Gamma_{\text{spr}}^{(1)} + \Gamma_{\text{spr}}^{(2)} \quad (113)$$

$$\text{where } \Gamma_{\text{spr}}^{(i)} = 2\pi V^{(i)2} \rho. \quad (114)$$

Therefore at zeroth order,  $\Gamma_{\text{spr}}^{(0)} \propto \text{constant}$ , which agrees with the results observed in the  $\text{Au}^{24+}$  system [33] and the  $\text{Sn}^{13+}$  system in Fig. 13. For the first and second corrections

$$\Gamma_{\text{spr}}^{(1)} + \Gamma_{\text{spr}}^{(2)} \propto E^{4b} \exp\left(-\frac{E}{\epsilon_\rho}\right) \quad (115)$$

$$\therefore \Gamma_{\text{spr}} = \text{constant} + a E^{4b} \exp\left(-\frac{E}{\epsilon_\rho}\right), \quad (116)$$

with system dependent parameters  $a$ ,  $b$  and  $\epsilon_\rho$ . The energy dependence is heavily suppressed by  $a$  in tin systems, and at high energies the corrections decay to 0. The spreading width  $\Gamma_{\text{spr}}$  in a system can hence be approximated as a constant value as long as  $a$  is small.

#### 4.5 Spreading Width and Level Growth Parameters in Tin

$\Gamma_{\text{spr}}$  is most strongly dependent on the level density  $\rho(E)$ . To obtain the density of states of the  $\text{Sn}^{13+}$  system, the number of levels in each configuration at the configuration energy (Fig. 16a) has been convolved with a Lorentzian of width  $\sim \Gamma = 23 \text{ eV}$  (the value of  $\Gamma_{\text{spr}}$  in  $\text{Sn}^{13+}$ ) to approximate the distribution of the energy levels (Fig. 16b). The number of levels  $N$  is seen to grow exponentially as expected. However, at lower energies, the density does not grow uniformly with parity. Instead it oscillates with growing the even and odd parities. This appears to be a quirk of tin systems.

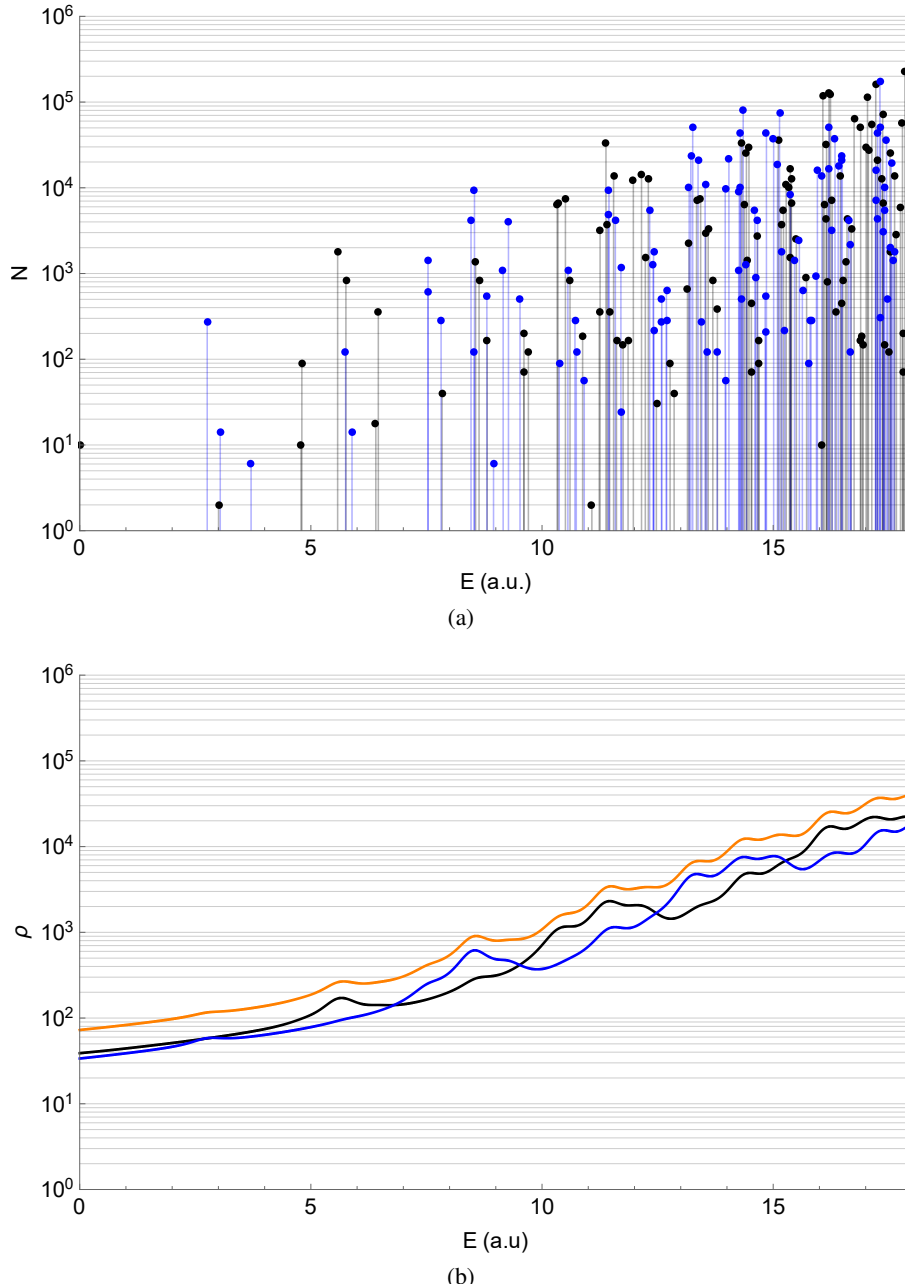


Figure 16. Number of energy levels in  $\text{Sn}^{13+}$  as a function of energy: (a) shows the number of levels for even (black) and odd (blue) parities as a function of average configuration energies; (b) shows the energy level density of even (black), odd (blue) and combined (orange) parities assuming an average spreading width of  $\Gamma_{\text{spr}} = 23 \text{ eV}$ .

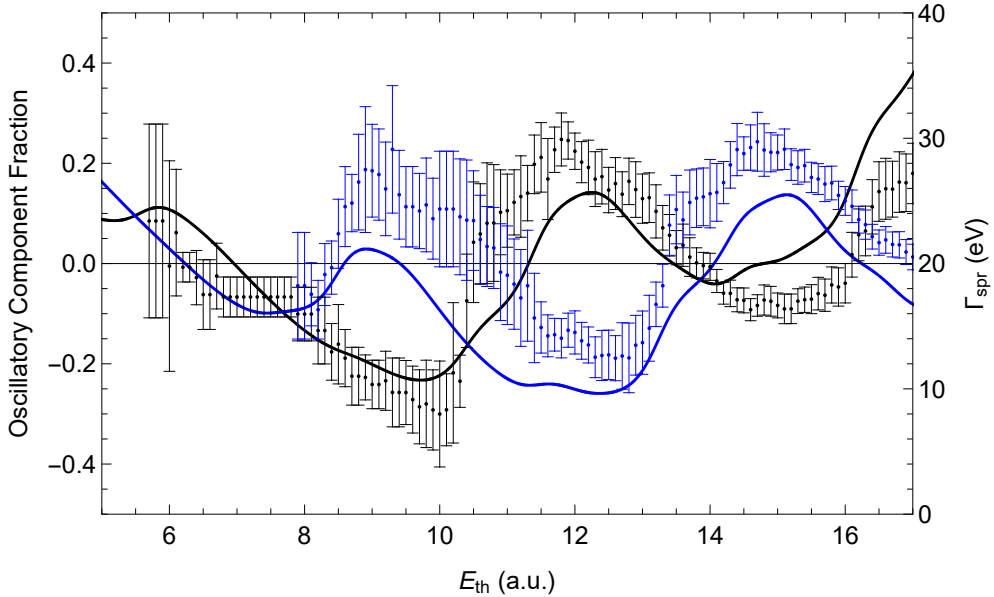


Figure 17. Oscillatory component of the level density normalised by the exponential density component (Eq. (117)), and the spreading width  $\Gamma_{\text{spr}}$  for  $\text{Sn}^{13+}$   $J = 1/2$ , as a function of threshold energy  $E_{\text{th}}$ . Black shows even parity, blue shows odd parity. Left axis (solid lines) shows the oscillatory component of the level density normalised by the total density. Right axis (dots) shows the corresponding  $\Gamma_{\text{spr}}$ .

As the energy threshold  $E$  increases, levels become more dense, and even and odd states occur more frequently. As a result, there is less of a difference in  $\rho$  and  $\Gamma_{\text{spr}}$  between the even and odd parities. The system approaches similar values for both parities, as the density oscillates with smaller amplitudes and higher frequencies. As seen in Fig. 17, the oscillatory component of the level density given by Eq. (117), qualitatively matches the oscillations in  $\Gamma_{\text{spr}}$ .  $\Gamma_{\text{spr}}$  is evidently highly dependent on the level density.

$$Osc = \left[ \rho(E) - a \exp(-E/\varepsilon_\rho) \right] / \rho(E) , \quad (117)$$

where  $a \exp(-E/\varepsilon_\rho)$  is the exponential component of  $\rho(E)$  obtained by finding the line of best fit.

This oscillation in even and odd level densities results in the large production of EUV light in tin ions. The first three local peaks in the density coincide with the average energy of the configurations that are primarily responsible for the emission of the 13.5 nm (91.8 eV) EUV light. These primary configurations and their energies for  $\text{Sn}^{13+}$  are summarised in Table 2. The large number of states at these peaks allows for many electric dipole (E1) transitions between successive peaks of opposite parity to occur. In particular, a large number of transitions can originate from highly excited states, and not just from the first excitation [4]. This further supports recently published work by Torretti et al. [9] that transitions between highly excited states contributes substantially to the 13.5 nm light emitted from the plasma. The inclusion and understanding of these states are hence critical to determining the properties of tin plasmas.

It should be noted that the energy gaps between these initial three peaks are approximately 70 eV–80 eV (15.5 nm–17.7 nm) instead of the expected 91.8 eV (13.5 nm). The well known phenomena of spectral narrowing due to configuration interaction however, shifts the spectra to the appropriate higher

energy [54] (this is discussed further in Section 5.3). Other local peaks can be observed beyond the third peak. These peaks are not as sharp though, do not occur in a strictly alternating fashion, and have a smaller separation between successive peaks. As a result, it is expected that transitions from these states will not have a significant contribution to the relevant narrow bandwidth centred at 13.5 nm as they will have longer wavelengths and will not occur with the same prominence.

Table 2. Primary EUV producing configurations of  $\text{Sn}^{13+}$  with their corresponding parities, energies and level density local peaks.

Peak	Configuration	$\pi$	E	
			(a.u.)	(eV)
Ground	$4s^24p^64d^1$	Even	0	0
1st peak	$4s^24p^54d^2$	Odd	2.758	75.0
	$4s^24p^64f^1$	Odd	3.040	82.7
2nd peak	$4s^24p^44d^3$	Even	5.579	151.8
	$4s^24p^54d^14f^1$	Even	5.758	156.7
3rd peak	$4s^24p^34d^4$	Odd	8.464	230.3
	$4s^24p^44d^24f^1$	Odd	8.539	232.4

For most MBQC applications, such as calculating the atomic cross-sections as discussed in Section 2.6, it is sufficient in to use an average value of  $\Gamma_{\text{spr}}$  for the entire system. This value can be obtained by taking the mean value for the odd and even  $\pi$  at small values of  $J$ , using an energy threshold that produces sufficiently large Hamiltonians such that MBQC is observed, but is also small enough that it is fast to compute the matrices. Average values of  $\Gamma_{\text{spr}}$  for the tin ions  $\text{Sn}^{7+}$ – $\text{Sn}^{14+}$  are provided in Table 3.

Furthermore, by using plots such as Fig. 16b, the statistical growth parameter  $\varepsilon_\rho$  can be extracted for a system. This parameter is useful in other calculations involving plasma. For instance, a crucial diagnostic element of EUV lithography, and plasma processes in general, is the measurement of the plasma temperature. This is well known as being experimentally difficult to obtain. However, a recently published method for measuring the temperature of a plasma based on the spectra of ions that exhibit MBQC, depends explicitly on  $\varepsilon_\rho$  [55]. Values of  $\varepsilon_\rho$  are also tabulated in Table 3.

Table 3. Values for  $\Gamma_{\text{spr}}$  and  $\varepsilon_\rho$  in the  $\text{Sn}^{7+}$ – $\text{Sn}^{14+}$  systems.

Ion	$\Gamma_{\text{spr}}$ (eV)	$\varepsilon_\rho$ (eV)
$\text{Sn}^{7+}$	13	$28.2 \pm 1.5$
$\text{Sn}^{8+}$	15	$30.8 \pm 1.8$
$\text{Sn}^{9+}$	16	$34.5 \pm 2.9$
$\text{Sn}^{10+}$	17	$41.6 \pm 2.0$
$\text{Sn}^{11+}$	20	$43.0 \pm 1.9$
$\text{Sn}^{12+}$	22	$44.0 \pm 6.2$
$\text{Sn}^{13+}$	23	$48.5 \pm 2.8$
$\text{Sn}^{14+}$	24	$50.5 \pm 1.9$

## 5 Transition Lines

Now that the spreading width for an atomic system has been shown to be weakly varying with energy, the transition lines for the  $\text{Sn}^{12+}$  system will be calculated using the statistical theory discussed in Section 2.8 and derived below. Due to the presence of an extra electron in the ground state  $4d$  orbital of  $\text{Sn}^{12+}$ , significantly more configurations exist for low energy states compared to  $\text{Sn}^{13+}$ . As a result, the chaotic mixing of  $\text{Sn}^{12+}$  is observed to a greater extent at lower excitations, making it an easier and more accurate system to analyse the statistical emission spectrum compared to that of  $\text{Sn}^{13+}$ .

### 5.1 A Derivation for the Statistical Line Strength

Starting by converting the single particle operator  $\hat{M}$  to the operator  $\hat{m}$  in the single electron orbital basis

$$\hat{M} = \sum_{ab} \langle a | \hat{m} | b \rangle a_a^\dagger a_b \quad (118)$$

$$M_{21} = \langle \Psi_2 | \hat{M} | \Psi_1 \rangle \quad (119)$$

$$= \sum_{ab} \langle a | \hat{m} | b \rangle \langle \Psi_2 | a_a^\dagger a_b | \Psi_1 \rangle \quad (120)$$

$$= \sum_{ab} m_{ab} \rho_{ab}^{(21)}, \quad (121)$$

where  $a$  and  $b$  are the final and initial electron orbitals.  $\rho_{ab}^{(12)} = \langle \Psi_2 | a_a^\dagger a_b | \Psi_1 \rangle$  is the transition matrix for the  $|\Psi_1\rangle \rightarrow |\Psi_2\rangle$  transition and determines the weight of the  $b \rightarrow a$  single electron transition in  $M_{21}$ . Due to the chaotic nature of the  $\Psi$  states, the matrix elements between different states are zero (see Eq. (56)). If it is also assumed that single-electron transitions are uncorrelated, the mean squared transition matrix element becomes

$$\overline{|M_{21}|^2} = \sum_{ab} |m_{ab}|^2 \overline{|\rho_{ab}^{(21)}|^2}. \quad (122)$$

Using the MBQC property that  $\Psi$  is a superposition of a large number of single electron basis states (Eq. (36)), the mean squared transition matrix can be written as

$$\overline{|\rho_{ab}^{(21)}|^2} = \sum_{ij} \overline{C_j^{(2)} C_i^{(1)}} \langle \Phi_j | a_a^\dagger a_b | \Phi_i \rangle \langle \Phi_i | a_b^\dagger a_a | \Phi_j \rangle \quad (123)$$

$$= \sum_{ij} w_1(E_j) w_2(E_i) \langle \Phi_j | a_a^\dagger a_b | \Phi_i \rangle \langle \Phi_i | a_b^\dagger a_a | \Phi_j \rangle, \quad (124)$$

where  $w$  are the Lorentzian distributions previously discussed. The double sum can be simplified, as for a fixed  $j$  there is only one basis state  $|\Phi_j\rangle = a_b^\dagger a_a | \Phi_j \rangle$  that gives a non-zero contribution. Furthermore, this state has energy

$$E_i = E_j + \varepsilon_b - \varepsilon_a \quad (125)$$

$$= E_j + \omega_{ba}, \quad (126)$$

where  $\varepsilon_{a/b}$  are the single electron orbital energies and  $\omega_{ba}$  is the energy of the single-electron transition.

Equation (124) can hence be reduced to

$$\overline{\left| \rho_{ab}^{(21)} \right|^2} = \sum_j w_1(E_j + \omega_{ba}) w_2(E_j) \langle \Phi_j | a_a^\dagger a_b a_b^\dagger a_a | \Phi_j \rangle \quad (127)$$

$$= \sum_j w_1(E_j + \omega_{ba}) w_2(E_j) \langle \Phi_j | \hat{n}_a (1 - \hat{n}_b) | \Phi_j \rangle . \quad (128)$$

$\hat{n}$  is the number operator and gives the number of particles in the  $a$  and  $b$  orbitals of the  $j$ th basis state. If occupancies vary slowly with energy, this occupancy matrix element can be replaced by the average value

$$\langle n_a (1 - n_b) \rangle_2 = \sum_j w_2(E_j) \langle \Phi_j | \hat{n}_a (1 - \hat{n}_b) | \Phi_j \rangle , \quad (129)$$

which gives the mean occupancy in the vicinity of the chaotic  $|\Psi_2\rangle$  state. Hence

$$\overline{\left| \rho_{ab}^{(21)} \right|^2} = \langle n_a (1 - n_b) \rangle_2 \sum_j w_1(E_j + \omega_{ba}) w_2(E_j) . \quad (130)$$

The remaining summation can be shown to yield the following (see Eq. (4.12)–(4.18) of Ref. [13] for mathematical details)

$$\sum_j w_1(E_j + \omega_{ba}) w_2(E_j) = D_1 \tilde{\delta}(\Gamma_1, \Gamma_2, \Delta) \quad (131)$$

$$\tilde{\delta}(\Gamma_1, \Gamma_2, \Delta) = \frac{1}{2\pi} \frac{(\Gamma_1 + \Gamma_2)}{\Delta^2 + (\Gamma_1 + \Gamma_2)^2/4} \quad (132)$$

$$\Delta = \omega_{ba} - \omega \quad (133)$$

$$\Rightarrow \overline{\left| \rho_{ab}^{(21)} \right|^2} = D_1 \langle n_a (1 - n_b) \rangle_2 \delta(\Gamma_1, \Gamma_2, \Delta) \quad (134)$$

$$\text{or equivalently } \overline{\left| \rho_{ab}^{(21)} \right|^2} = D_2 \langle n_b (1 - n_a) \rangle_1 \delta(\Gamma_1, \Gamma_2, \Delta) , \quad (135)$$

by initially summing over  $j$  instead of  $i$ .  $D_i$  is the average level spacing in the vicinity of the  $|\Psi_i\rangle$  state, and  $\tilde{\delta}$  is a finite width  $\delta$  function.  $\tilde{\delta}$  is taken to have the same Lorentzian form as the strength functions.  $\Gamma_1$  and  $\Gamma_2$  are the spreading widths for states 1 and 2 respectively.  $\tilde{\delta}$  is a manifestation of conservation of energy in the transitions. When the energy of the single electron transition is significantly different to that of the photon energy (i.e.  $|\Delta| > \Gamma$ ),  $\tilde{\delta}$  becomes small. This corresponds to a decrease in  $\overline{\left| \rho_{ab}^{(21)} \right|^2}$  due to there being a low probability of the principal components of states in  $|\Psi_1\rangle$  and  $|\Psi_2\rangle$  differing by only one electron.

Finally, by applying the Wigner-Eckhart theorem to give the reduced matrix elements, independent of the angular projections (also detailed in Ref. [13]), the statistical line strength  $S$  of the transition between complex states  $|\Psi_1\rangle$  and  $|\Psi_2\rangle$  is obtained as was presented in Eq. (73), and repeated is below

$$S_{21} = \overline{|\langle \Psi_2 | \hat{M} | \Psi_1 \rangle|^2} \\ = \frac{2J_1 + 1}{3} D_2 \sum_{a,b} |\langle a | \hat{m} | b \rangle|^2 \frac{1}{2\pi} \frac{\Gamma_1 + \Gamma_2}{(\omega_{ba} - \omega)^2 + (\Gamma_1 + \Gamma_2)^2/4} \left\langle \frac{n_b}{2j_b + 1} \left( 1 - \frac{n_a}{2j_a + 1} \right) \right\rangle_1 , \quad (73)$$

where  $J_1$  is the average total momentum of the  $|\Psi_1\rangle$  state and  $j$  is the total angular momentum of the  $a/b$  single electron orbitals.

Typically only E1 transitions are considered as they are usually orders of magnitude stronger than other higher order transitions, such as the M1 and E2 transitions.  $\hat{M}$  and  $\hat{m}$  can hence be replaced by the electron dipole moment operators  $\hat{D}$  and  $\hat{d}$ . Equivalent substitutions could be made for the higher order transitions.

## 5.2 A Mean Spectrum from Averaged Configurations

Without resorting to performing computationally expensive CI, the exact energies and compositions of the eigenstates  $|\Psi\rangle$  are unknown. However, an average value of the states  $|\chi\rangle$  in a local area can be determined using the number of projections  $N_j$  and average energy  $E_j$  in each relativistic basis configuration  $|\Phi_j\rangle$ . These values for the ground and first excited states of  $\text{Sn}^{12+}$  are presented in Table 4.  $|\chi_i\rangle$  is chosen to coincide with  $|\Phi_i\rangle$ , such that it contains  $N_i$  states in its vicinity with average energy  $E_i$ . As the system is chaotic, the weighting of the relativistic basis configurations in the mixed state is given by

$$|\chi_i\rangle = \sum_j N_j C_j^{(i)} |\Phi_j\rangle . \quad (136)$$

While the  $D_2$  level spacing can still be obtained from the inverse level density using a density graph like that shown in Fig. 16b, due to the averaging process, the value  $J_1$  of each state is unknown. Instead an average value  $\bar{J}_1$  is used. This is the average value of  $J_i$  for each basis state  $|\Phi_i\rangle$  weighted by the mixed state  $|\chi_1\rangle$  coefficients.

A further modification has been made to Eq. (73) as the Lorentzian strength and finite width delta function were found to not decay fast enough, producing non-negligible contributions at large distances (i.e.  $\Delta \gg \Gamma$ ). This results in highly energetic multiply excited states mixing with the ground state of the system, producing noticeable contributions despite being many multiples of  $\Gamma_{\text{spr}}$  apart in energy. When calculating the line strengths, this manifests itself as non-physical transitions between levels that mostly contain basis states of the same excitation, or basis states that differ by two or more excitations. This second scenario is especially troublesome as the energies of these transitions are significantly higher than that of the physical transitions. As observed intensity scales as  $\omega^4 S$ , these non-physical lines can become orders of magnitude larger than the actual transitions. It is known that the tails of the strength function  $w$  do decay much faster than that of a Lorentzian (this can be seen in Fig. 11b), and alternative distributions such as the Squared Lorentzian and Lorentzian with exponential tails have been suggested [13]. For simplicity, a Lorentzian with a sharp cutoff has been used here, with the function re-normalised such that the integral of the distribution over all energy remains equal to unity as shown in Eq. (137)

$$\frac{1}{2\pi} \frac{\Gamma}{(E - E_0)^2 + \Gamma^2/4} \rightarrow \frac{1}{2\pi} \frac{\Gamma}{(E - E_0)^2 + \Gamma^2/4} \theta(|E - E_0| - E_c) \frac{\pi}{2 \tan^{-1}(2E_c/\Gamma)} , \quad (137)$$

where  $\theta$  is the Heaviside step function and  $E_c$  is the cutoff energy such that the function is zero when  $|E - E_0| > E_c$ .  $E_c$  has been set to approximately  $2\Gamma_{\text{spr}}$ . Furthermore, as previously shown in Section 4,  $\Gamma_{\text{spr}}$  is slowly varying and the approximation  $\Gamma_1 + \Gamma_2 \sim 2\Gamma_{\text{spr}}$  can be readily assumed.

Finally, the expectation value can be calculated explicitly from the occupancies of the weighted basis states (Eq. (129)), and the single electron transition matrix elements can be obtained directly from AMBiT. Table 5 shows these matrix elements, and the energies of the transitions  $\omega_{ba}$  for the relevant transitions in the  $\text{Sn}^{12+}$  system. The average statistical line strength  $\bar{S}$  of a transition between chaotically mixed states is hence given by

$$\overline{S_{21}} = N_2 N_1 \overline{|\langle \chi_2 | \hat{D} | \chi_1 \rangle|^2} \quad (138)$$

$$= N_2 N_1 \frac{2J_1 + 1}{3} D_2 \sum_{a,b} |\langle a | \hat{d} | b \rangle|^2 \frac{1}{2\pi} \frac{2\Gamma_{\text{spr}}}{(\omega_{ba} - \omega)^2 + (2\Gamma_{\text{spr}})^2 / 4} \theta(|\omega_{ba} - \omega| - E_c) \\ \times \frac{\pi}{2 \tan^{-1}(E_c / \Gamma_{\text{spr}})} \left\langle \frac{n_b}{2j_b + 1} \left( 1 - \frac{n_a}{2j_a + 1} \right) \right\rangle_1. \quad (139)$$

Figure 18 shows the application of Eq. (139) to obtain the line strength spectra for the  $\text{Sn}^{12+}$  system when including the various excitation levels primarily responsible for the emission of EUV light.  $\Gamma_{\text{spr}}$  has been set to 22 eV (as determined from Table 3). The blue lines show the spectra due to the statistical theory, while the black and red lines show the spectra obtained directly from AMBiT with and without CI enabled respectively. Furthermore, the solid lines show the discrete spectra convolved with a narrow Lorentzian that has full width half maximum (FWHM) 1 eV so that the cumulative effects of the exact spectra can be easily compared with the statistical theory. See file [Spectra\\_Calculation.nb](#) in the github repository for the implementation of this theory.

Once the line strengths are calculated using Eq. (139), the power intensity spectrum can be determined by using the LTE assumptions discussed in Section 2.8. For convenience, the relevant equations are repeated below.

$$Z = \sum_i g_i \exp\left(-\frac{E_i}{T}\right) \quad (78)$$

$$\frac{I_{12}}{N_T} = \frac{1.0608 \times 10^6}{4\pi} \frac{1}{Z} \exp\left(-\frac{E_1}{T}\right) \omega^4 S_{21}. \quad (79)$$

The difference in the application of these formulas when using the average statistical line strength is that, instead of  $g_i$  being the statistical weight of an individual level, it is now the statistical weight for the mixed state  $|\chi_i\rangle$  with  $g_i = N_i$ . Similarly,  $E_i$  is also now the average energy of the mixed state  $|\chi_i\rangle$ . Figure 19 shows an example of this power intensity spectrum when including the highest level excitations at an effective LTE temperature of  $T = 26$  eV. This is equivalent to an actual plasma temperature of 36 eV as shown by Sheil and Versolato [51].

Table 4. Configuration average energies and number of projections for relativistic configurations in the ground and first excited states of  $\text{Sn}^{12+}$ .

Excitation	Relativistic Configuration	$E$ (eV)	$N$
Ground	$4p_{1/2}^2 4p_{3/2}^4 4d_{3/2}^2$	0.00	6
	$4p_{1/2}^2 4p_{3/2}^4 4d_{3/2}^1 4d_{5/2}^1$	1.88	24
	$4p_{1/2}^2 4p_{3/2}^4 4d_{5/2}^2$	3.29	15
First ( $d$ shell)	$4p_{1/2}^2 4p_{3/2}^3 4d_{3/2}^3$	68.68	16
	$4p_{1/2}^2 4p_{3/2}^3 4d_{3/2}^2 4d_{5/2}^1$	72.03	144
	$4p_{1/2}^2 4p_{3/2}^3 4d_{3/2}^1 4d_{5/2}^2$	74.88	240
	$4p_{1/2}^2 4p_{3/2}^3 4d_{5/2}^3$	77.31	80
	$4p_{1/2}^1 4p_{3/2}^4 4d_{5/2}^3$	82.26	40
	$4p_{1/2}^1 4p_{3/2}^4 4d_{3/2}^1 4d_{5/2}^2$	83.35	120
$f$ shell	$4p_{1/2}^1 4p_{3/2}^4 4d_{3/2}^2 4d_{5/2}^1$	83.97	72
	$4p_{1/2}^1 4p_{3/2}^4 4d_{3/2}^3$	84.11	8
	$4p_{1/2}^2 4p_{3/2}^4 4d_{3/2}^1 4f_{5/2}^1$	81.44	24
	$4p_{1/2}^2 4p_{3/2}^4 4d_{3/2}^1 4f_{7/2}^1$	82.97	32
	$4p_{1/2}^2 4p_{3/2}^4 4d_{5/2}^1 4f_{7/2}^1$	83.56	48
	$4p_{1/2}^2 4p_{3/2}^4 4d_{5/2}^1 4f_{5/2}^1$	84.41	36

Table 5. Single electron transition reduced matrix elements for  $\text{Sn}^{12+}$ .

$b \rightarrow a$	$\omega_{ba}$ (eV)	$ \langle a \parallel \hat{d} \parallel b \rangle ^2$ (a.u.)
$4d_{3/2} \rightarrow 4p_{1/2}$	80.52	0.901
$4d_{3/2} \rightarrow 4p_{3/2}$	71.07	0.186
$4d_{5/2} \rightarrow 4p_{3/2}$	72.76	1.687
$4f_{5/2} \rightarrow 4d_{3/2}$	106.37	1.928
$4f_{5/2} \rightarrow 4d_{5/2}$	104.67	0.139
$4f_{7/2} \rightarrow 4d_{5/2}$	104.76	2.790

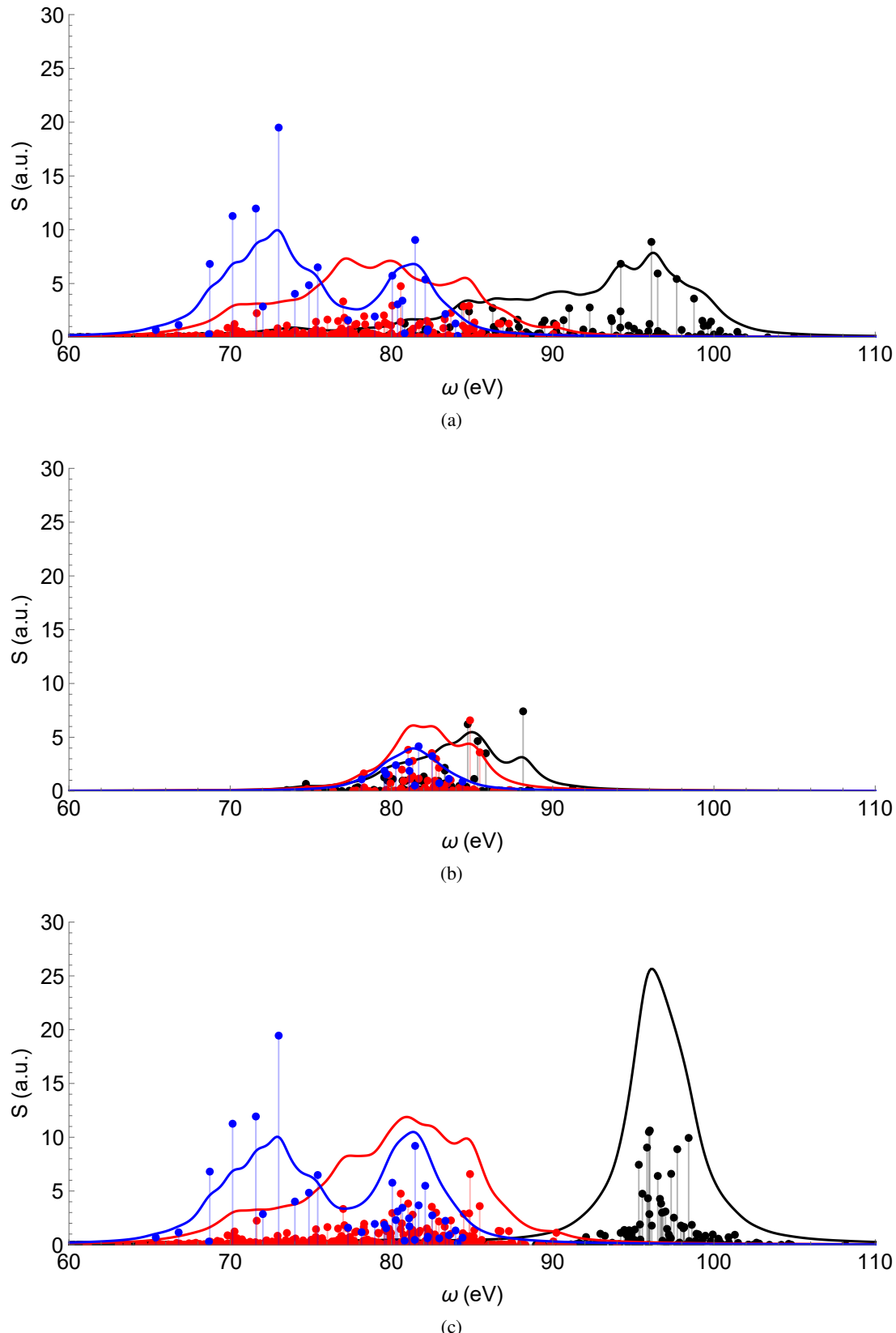


Figure 18. Line strengths for EUV producing configurations of  $\text{Sn}^{12+}$ . All figures include the ground state  $4p^6 4d^2$ . (a) includes  $4p^5 4d^3$ ; (b) includes  $4p^6 4d^2 4f^1$ ; (c) includes  $4p^5 4d^3 + 4p^6 4d^2 4f^1$ ; (d) additionally includes  $4p^4 4d^4 + 4p^5 4d^3 4f^1$ ; (e) further includes  $4p^3 4d^5 + 4p^4 4d^4 4f^1$ . Blue/Red/Black lines are the statistical/non-CI/CI theories respectively.

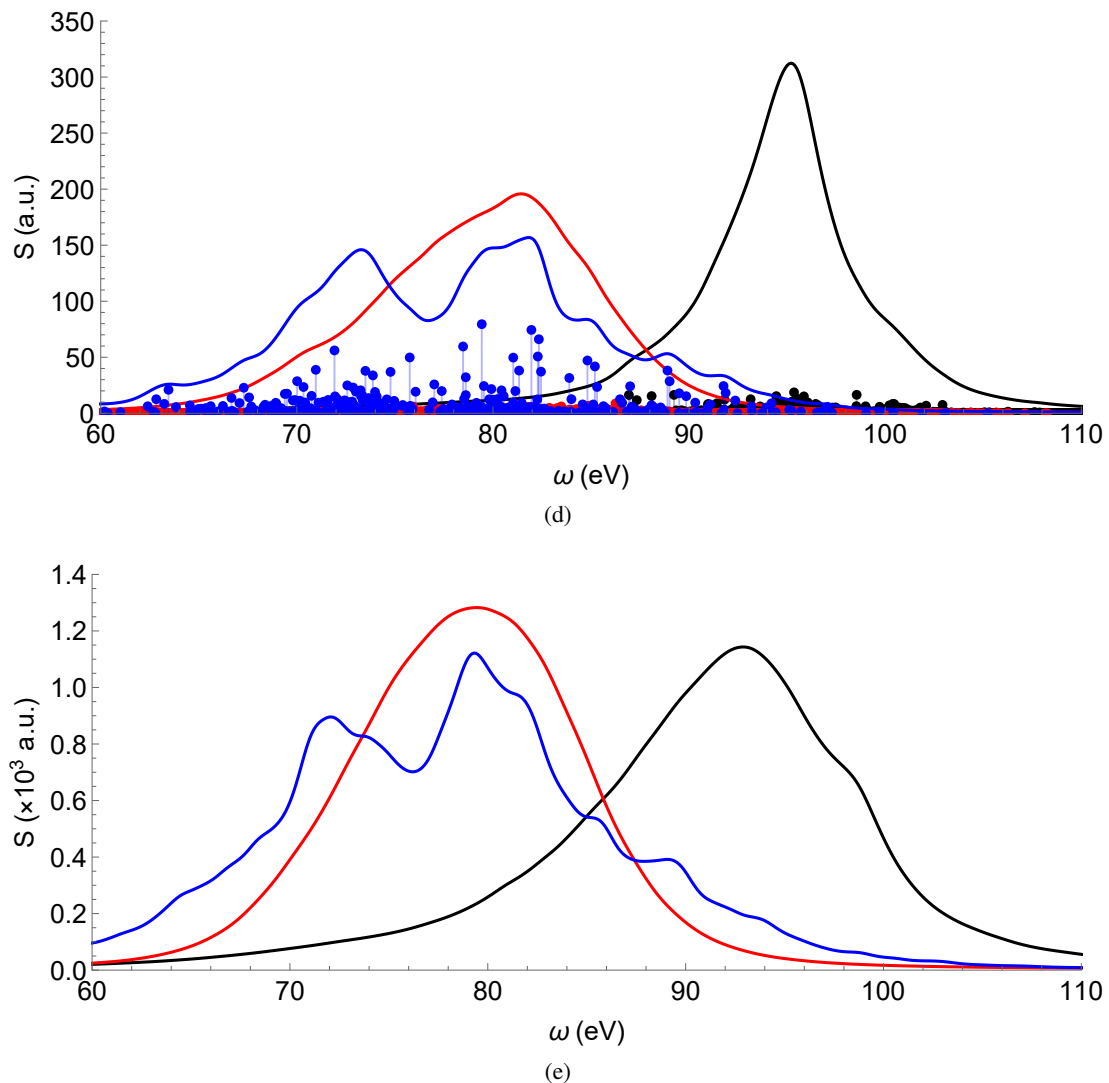


Figure 18. Line strengths for EUV producing configurations of  $\text{Sn}^{12+}$  continued.

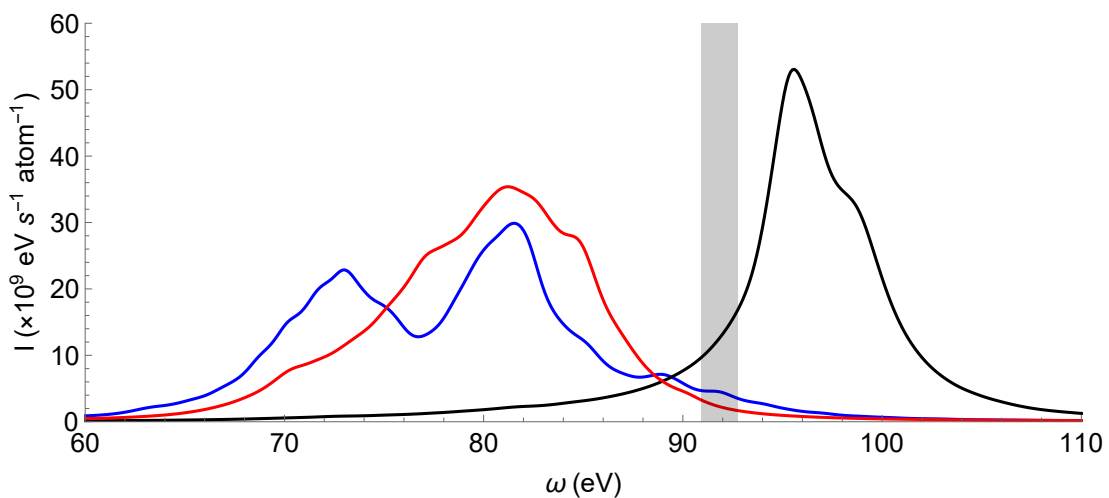


Figure 19. Power intensity spectrum including up to the third level excitations for  $\text{Sn}^{12+}$  (Fig. 18e) at the LTE temperature of 26 eV. Blue/Red/Black lines are the statistical/non-Cl/CI theories respectively. Grey shading shows the 2% bandwidth useful for EUV lithography. The inclusion of further configurations would shift the black peak into this region.

### 5.3 The Impact of CI on the Emission Spectra

From Fig. 18 it can be seen that the statistical theory agrees quite well with the non-CI results, with the total line strength (i.e. the summation of all the discrete lines or the integral of the continuous lines) agreeing to within 10%. Furthermore, as the energy and number of configurations included increases, the statistical theory improves with respect to the non-CI results, with total line strengths growing closer in agreement. As the number of configurations increases, the amount of interactions in the system, and hence chaos, increases and MBQC becomes more strongly applicable. In addition to the line strength spectra being in agreement, so to is the power intensity spectrum shown in Fig. 19.

The main discrepancy between the statistical and non-CI theory is the presence of two distinct peaks occurring in the statistical theory. This is due to the large fine structure splitting of the  $p_{1/2}$  and  $p_{3/2}$  shells in the  $d$  level excitations causing a large split in the average configuration energies. Although individual projections do lie between these energies and distribute the spectrum in between the peaks, the states and line strengths have been collected on either side due to the averaging process. This results in the formation of the two peaks.

It is important to note however, that the statistical theory (blue line) clearly does not agree at all with the results obtained when using CI (black line). While it appears to reproduce the effects of having transitions between mixed states, two key effects are not replicated by the statistical theory: the increase in photon energy, and spectral narrowing. These are important effects that cause the spectrum to occur in the narrow bandwidth near the important 91.8 eV (13.5 nm) EUV energies, and must be present in the statistical theory for it to be properly applicable to the tin systems.

#### 5.3.1 Energy Shift

As was discussed in Section 2.3, the presence of interactions between the levels causes level repulsion that spreads out the distribution of energy levels within the system. This redistribution results in higher energy levels that can produce higher energy photons, enabling the spectrum to shift to higher energies as made evident in Fig. 18 for all transitions. When the statistical theory was applied, the average energy levels were taken as the average energy of each relativistic configuration. These values are obtained from AMBiT prior to the application of CI and mixing of states, and as such do not include the appropriate energy shifts.

An approximation for how these average energies change due to interactions can be obtained through second order perturbation theory. In MBQC, the interactions between individual levels is of the same or higher magnitude than the level spacing, necessitating the diagonalisation of the full Hamiltonian. However, the energy spacing between the average configurations is significantly larger while the interaction energy remains the same (average states interact with a similar strength to that of individual states within the average). Hence  $V^2 \ll D$  and second order perturbation can reasonably be applied to the system. This is equivalent to obtaining the eigenvalues of a Hamiltonian where the average configuration energies populate the main diagonal, and interactions populate the off-diagonal elements.

Furthermore, as  $\text{Sn}^{12+}$  is a chaotic system that obeys GOE statistics, the off diagonal interaction elements can be obtained from a Gaussian distribution with mean 0 and standard deviation equalling the

mean interaction strength  $V$ . This  $V$  can be obtained from the spreading width  $\Gamma_{\text{spr}}$  of the system (which has been shown to be approximately constant), and the maximum level density of the system (which can be obtained using a level density plot such as in Fig. 16b). As  $H_{ij}$  is randomly distributed, a Monte-Carlo simulation can be performed to obtain an average value of the eigenvalues (see file [Monte-Carlo.nb](#) in the github repository). This is computationally tractable, as by only considering the average energies of each configuration, the size of the matrix reduces by orders of magnitudes. As was shown in Section 4.1, the number of configurations grows via a power law instead of exponentially like the number of levels. For instance, considering up to the third level excitations of  $\text{Sn}^{12+}$ , a matrix of only 81 average energies needs to be diagonalised instead of 38075 individual levels.

Figure 20 show the application of this method to obtain the shifted average energy levels when including the second excitement levels, as well as a comparison to the exact shift of the energy levels as obtained from AMBiT. They are in good agreement. It is important to note that the method of obtaining  $V$  via  $\Gamma_{\text{spr}}$  and  $D$  does not work particularly well when only a few, low energy configurations are included, as MBQC has not fully developed within the system. The  $V$  used in Fig. 20 was instead obtained directly from the Hamiltonian matrices produced by AMBiT.

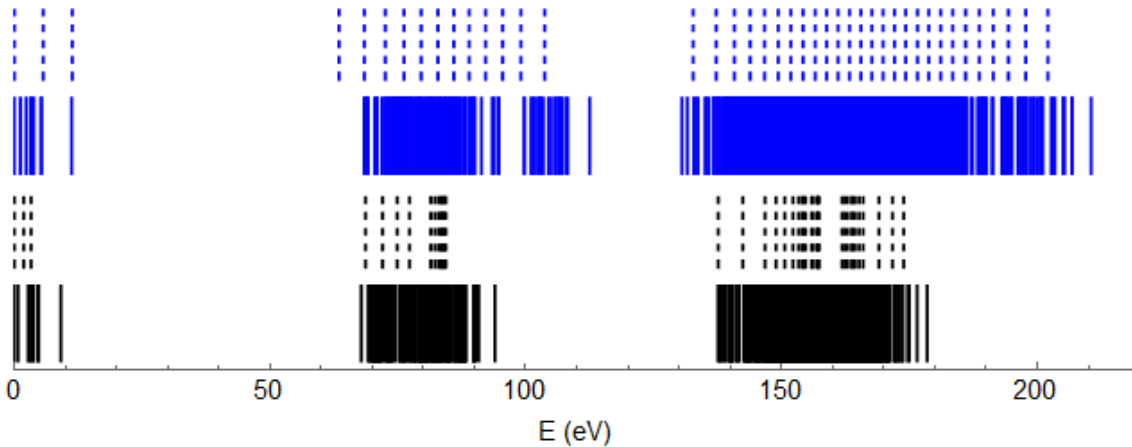


Figure 20. Energies of all second level excitations states in  $\text{Sn}^{12+}$ . Black shows energies without CI; Blue shows energies with CI; Solid lines show individual levels; Dashed lines show configuration averaged energies. CI lines were obtained using an average interaction energy  $V = 2.2 \text{ eV}$ .

### 5.3.2 Spectral Narrowing

While it is straightforward to use the newly shifted average energy levels in the statistical theory, it far from reproduces the CI spectrum. In addition to producing higher energy configurations that higher energy photons can be produced from, level repulsion also narrows the gap between the excitation levels as illustrated by the blue lines in Fig. 20, allowing much lower energy photons to also form. This spectral broadening is not physically observed however, and most of the low energy transitions are heavily suppressed, leaving only a narrow band of strong lines in the 90–100 eV region such that the total line strength is preserved. This spectral narrowing is a well known phenomena of systems that include transitions from the  $4p^5 4d^{m+1} + 4p^6 4d^m 4f^1$  configurations [54, 56, 57]. This narrowing can be clearly be seen when the excitaions from Figs. 18a and 18b are included together to produce Fig. 18c, which has a sharp peak at  $\sim 96 \text{ eV}$ .

Although this is a well known effect of CI, the physical mechanisms responsible for this narrowing are not well understood, and are not reflected in the statistical theory. While the statistical theory does suppress transitions that occur far from the single electron transitions, these single electron energies do not occur at the high energies required to match the CI results. Take for instance the  $4p^54d^3 \rightarrow 4p^64d^2$  transitions in Fig 18a. Although photons occur at the necessary high energy ranges, the allowed single electron transitions (see Table 5) occur at energies of  $\sim 70$  and  $80\text{ eV}$ , resulting in the incorrect suppression of the desired high energy photons in the  $90\text{--}100\text{ eV}$  range.

This result implies three distinct possibilities for the origin of the discrepancy between the statistical theory and the CI results

1. CI completely changes the single electron orbital energy levels  $\varepsilon_{a/b}$ , and  $\omega_{ba}$  needs to be redefined for use in the energy conservation term  $\Delta = \omega_{ba} - \omega$ .
2. After the line strengths are calculated, a secondary (currently unknown) mechanism redistributes the line strengths among the various basis configurations to produce the spectral narrowing.
3. Transitions from the individual basis state components cannot be treated completely independently in a transition between CI mixed states as currently formulated in the statistical theory.

At this stage it is unknown which (or whether it is a combination) of these possibilities is responsible for the spectral narrowing. A secondary mechanism (Option 2) is currently preferred by existing works, although it is not obvious how to include this in the statistical approach.

### 5.3.3 The Difficulty of a Generalised Heuristic

The development of a heuristic to redistribute the line strengths was considered, however one could not be formulated so as to be generalised to include additional configurations, let alone different systems. While a bandpass filter based on the photon energies could be applied to centre the line strength spectrum at the empirically observed  $91.8\text{ eV}$ , this does not reproduce the power intensity spectrum. Due to the Boltzmann factor suppression of the intensity, which configurations the photons originate from have important implications. Lines attributed to higher energy configurations would become heavily suppressed, while lines from lower energy configurations would remain pronounced. As a result, the line strengths would need to be redistributed based on the configurations instead of the photon energies. However it is unknown *a priori* which configurations are responsible for the emitted light.

Considering the second excitations of  $\text{Sn}^{12+}$ , it was empirically found that by only considering the line strengths originating from configurations in the upper energy regions of each excitement level, the spectra could be reasonably reproduced as shown in Fig. 21 (see file [Heuristic.nb](#) in the github repository). However there did not appear to be any defining features of these configurations that would lead to them being the primary sources of light. Furthermore, when additional configurations are added that lie between the excitement levels, it would become impossible to identify where each excitement level begins and ends, and hence which configurations to include. It is also unknown what additional effects the interaction and mixing of these additional states may have on the spectra.

Without a more thorough understanding of the physical mechanisms that cause spectral narrowing and how the lines strengths are reallocated, no heuristic can be successfully developed to accurately re-produce the line strength and power intensity spectra.

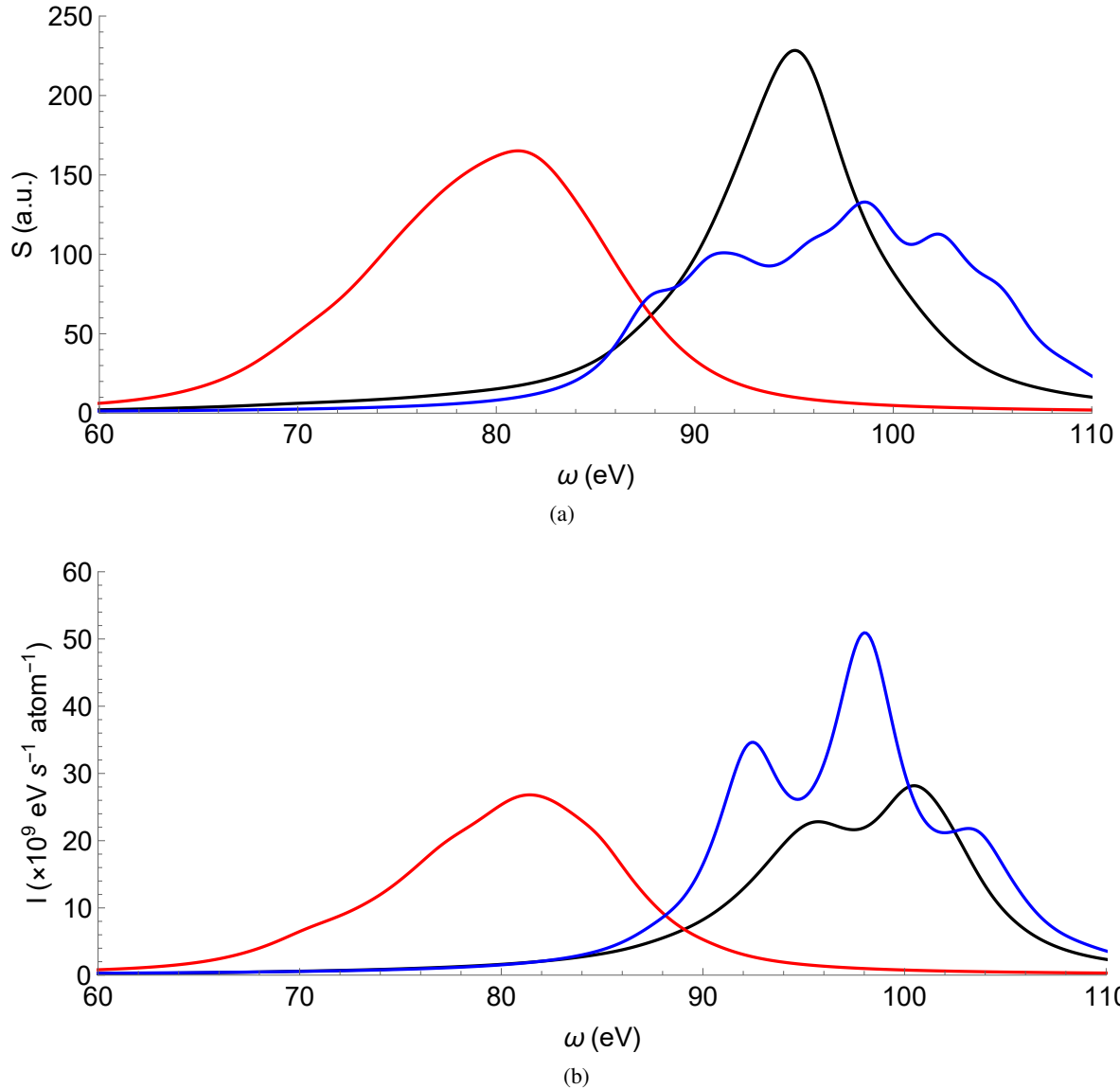


Figure 21. Spectra for second level excitations of  $\text{Sn}^{12+}$  sing the heuristic described in Section 5.3.3. (a) shows the line strength; (b) shows the power intensity. Blue line shows the statistical theory with applied heuristic. Red and black lines show non-CI and CI theories respectively.

#### 5.4 A Statistical Plasma Intensity Spectrum

Although the statistical theory for the line strength is acknowledged as being incomplete because it does not reproduce the expected spectral narrowing, it has been used in its current form (described in Section 5.2, i.e. without CI) to produce the total emission spectra observed from a tin plasma. Figure 22 shows the spectra for a tin plasma at a temperature of 36 eV. See file [Plasma\\_Spectra.nb](#) in the github repository for the application of the theory to the given plasma. Sheil and Versolato [51] have shown that this condition is equivalent to a LTE plasma with temperature 26 eV and ionic constituents as per

Table 6. Only the primary EUV generating configurations (Eq. (1), repeated below) have been included. The spreading widths and ground state occupancies  $m$  have also been included in Table 6.

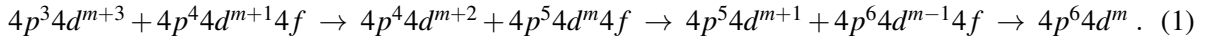


Table 6. Fraction of ions present and spreading width in a tin plasma with a LTE temperature of 26 eV

Ion	Fraction [51]	$\Gamma_{\text{spr}}$ (eV)	$m$
$\text{Sn}^{10+}$	0.013	17	4
$\text{Sn}^{11+}$	0.103	20	3
$\text{Sn}^{12+}$	0.374	22	2
$\text{Sn}^{13+}$	0.396	23	1
$\text{Sn}^{14+}$	0.114	24	0

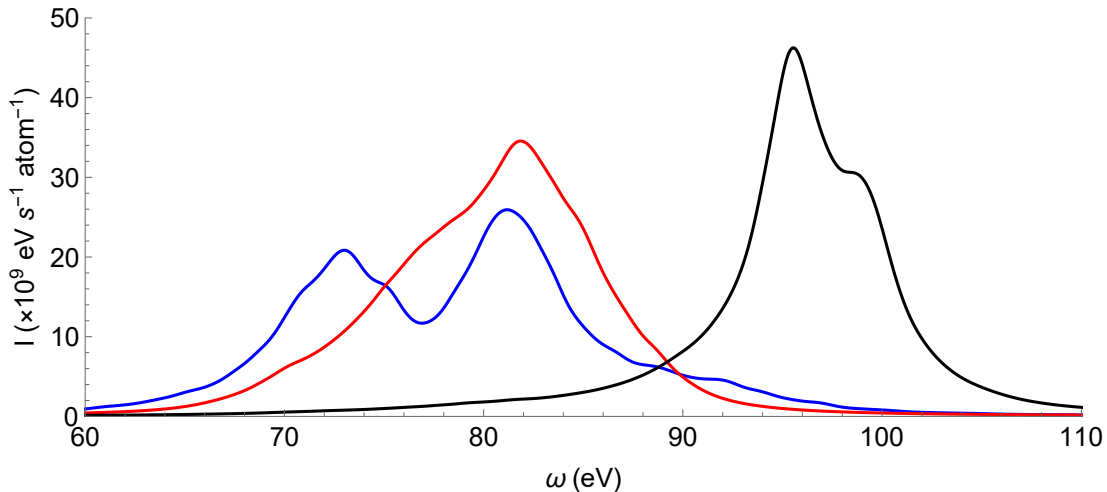


Figure 22. Power intensity spectrum for a tin plasma at a non-LTE (LTE) temperature of 36 eV (26 eV).

Again it can be seen that the statistical theory (blue) agrees well with the non-CI results (red) but not the CI spectra (black). The statistical theory also exhibits two peaks for the same averaging reasons explained earlier in Section 5.3. Figure 22 does however show that the statistical spectra from various ionic constituents can be combined together to give an approximation of the actual spectra. Once the effects of CI have been properly incorporated into the statistical theory, it is expected that the total optical spectra from a tin plasma will be able to be accurately calculated in a fast and computationally efficient manner.

## 6 Conclusion

EUV-lithography is the next step to producing smaller, more efficient semiconductor components. However, in order for it to become industry standard, the tin plasma utilised to produce the EUV light needs to be better optimised. In order for this to occur, the understanding of the atomic properties and light emission characteristics of highly charged tin ions needs to be improved. This is difficult to accomplish due to the size and complexity of calculating the properties of systems with open  $d$  and  $f$  shells.

By using MBQC and statistical theories such as doorway states, a better understanding of the properties of highly charged tin ions can be obtained. Due to the strong interactions of the many excited states, RMT and MBQC are appropriate theories that can be applied to the tin system. This has been verified as the nearest neighbour spacing of all the tin ions can be fitted to Wigner's surmise, and the eigenstate components of the mixed energy levels match the theorised Lorentzian distributions.

Furthermore, through the use of combinatorics, the MBQC property of spreading width  $\Gamma_{\text{spr}}$  has been shown to be constant to a good approximation. Constant values for this spreading width for use in calculating statistical atomic cross-sections and line strengths were determined and found to be in the 13–24 eV range for the  $\text{Sn}^{7+}$ – $\text{Sn}^{14+}$  ions. With these values, further work could now be performed in calculating the resonant recombination cross-sections of the tin systems and comparing them to experimental results.

Another parameter obtained was the level growth parameter  $\varepsilon_\rho$  for the tin systems. Now that these values are known, recent theories on methods to perform temperature diagnostics on plasmas can be applied to EUV-lithography. If successful, this will greatly impact and improve the ability to characterise, monitor and optimise plasma systems in an industrial setting.

Higher order corrections to the spreading width were also shown to be proportional to the number and maximum energy of the configurations included in the Hamiltonian, but are heavily suppressed in the tin systems. In addition, it was found that although the number of individual levels grows exponentially with energy, the number of configurations grows via power law. This result can significantly reduce the size of calculations if average states centered about the average configuration are considered instead of all of the exact levels. The origin of this power law relation in the number of configurations is currently unknown though. Additional research into reasons behind this relation would improve our understanding of atomic configurations, as well as inform as to where this averaging simplification can be utilised.

The statistical theory for obtaining line strengths due to transitions between mixed states was also applied to real tin systems. This theory was also successfully modified so that average states could be used instead of all the individual transitions. It was found that the statistical theory agreed well with the results obtained from exact numerical calculations that did not include configuration interactions. However, deficiencies were found within the theory as it did not replicate the key configuration interaction effect of spectral narrowing which is responsible for the large production of EUV light from the tin ions. A better understanding of the mechanisms in CI that redistribute the line strengths amongst the configurations will lead to a more complete theory, and enable the implementation of the suggestions made in Section 5.3.2. Once these correction are made though, MBQC will provide a computationally efficient method of calculating the spectra observed from a plasma, allowing for a better understanding and optimisation of the emission spectra.

Through the use of MBQC, it is hoped that a better understanding of atomic processes can be obtained, and more computational efficient methods for calculating average atomic properties can be implemented. This thesis has shown that highly charged tin ions are optimal systems in which to apply MBQC, as well as having calculated crucial values for the application of these theories. Notwithstanding the problems with implementing CI, incorporating MBQC into the calculation of plasma properties will enable improved optimisation of EUV-lithography techniques, facilitating the mass manufacture of vastly improved semiconductor components.

## References

- [1] A. Mallik et al., “The need for EUV lithography at advanced technology for sustainable wafer cost”. In: *Extreme Ultraviolet (EUV) Lithography IV*. Ed. by P. P. Naulleau. SPIE, 2013. DOI: 10.1117/12.2011528.
- [2] O. O. Versolato, “Physics of laser-driven tin plasma sources of EUV radiation for nanolithography”. *Plasma Sources Science and Technology*, 28.8 (2019) 083001. DOI: 10.1088/1361-6595/ab3302.
- [3] S. Fujioka et al., “Pure-tin microdroplets irradiated with double laser pulses for efficient and minimum-mass extreme-ultraviolet light source production”. *Applied Physics Letters*, 92.24 (2008) 241502. DOI: 10.1063/1.2948874.
- [4] G. O’Sullivan et al., “Spectroscopy of highly charged ions and its relevance to EUV and soft x-ray source development”. *Journal of Physics B: Atomic, Molecular and Optical Physics*, 48.14 (2015) 144025. DOI: 10.1088/0953-4075/48/14/144025.
- [5] N. Fu, Y. Liu, X. Ma, and Z. Chen, “EUV Lithography: State-of-the-Art Review”. *Journal of Microelectronic Manufacturing*, 2.2 (2019) 1–6. DOI: 10.33079/jomm.19020202.
- [6] H. Gelderblom, H. Lhuissier, A. L. Klein, W. Bouwhuis, D. Lohse, E. Villermaux, and J. H. Snoeijer, “Drop deformation by laser-pulse impact”. *Journal of Fluid Mechanics*, 794 (2016) 676–699. DOI: 10.1017/jfm.2016.182.
- [7] D. Kurilovich, A. L. Klein, F. Torretti, A. Lassise, R. Hoekstra, W. Ubachs, H. Gelderblom, and O. O. Versolato, “Plasma Propulsion of a Metallic Microdroplet and its Deformation upon Laser Impact”. *Physical Review Applied*, 6.1 (2016) 014018. DOI: 10.1103/physrevapplied.6.014018.
- [8] S. Fujioka et al., “Opacity Effect on Extreme Ultraviolet Radiation from Laser-Produced Tin Plasmas”. *Physical Review Letters*, 95.23 (2005) 235004. DOI: 10.1103/physrevlett.95.235004.
- [9] F. Torretti et al., “Prominent radiative contributions from multiply-excited states in laser-produced tin plasma for nanolithography”. *Nature Communications*, 11.1 (2020) 2334. DOI: 10.1038/s41467-020-15678-y.
- [10] J. Bauche, C. Bauche-Arnoult, and M. Klapisch, “Unresolved transition arrays”. *Physica Scripta*, 37.5 (1988) 659–663. DOI: 10.1088/0031-8949/37/5/002.
- [11] J. White, P. Hayden, P. Dunne, A. Cummings, N. Murphy, P. Sheridan, and G. O’Sullivan, “Simplified modeling of 13.5 nm unresolved transition array emission of a Sn plasma and comparison with experiment”. *Journal of Applied Physics*, 98.11 (2005) 113301. DOI: 10.1063/1.2128055.
- [12] M. G. Su, Q. Min, S. Q. Cao, D. X. Sun, P. Hayden, G. O’Sullivan, and C. Z. Dong, “Evolution analysis of EUV radiation from laser-produced tin plasmas based on a radiation hydrodynamics model”. *Scientific Reports*, 7.1 (2017) 45212. DOI: 10.1038/srep45212.
- [13] V. V. Flambaum, A. A. Gribakina, G. F. Gribakin, and M. G. Kozlov, “Structure of compound states in the chaotic spectrum of the Ce atom: Localization properties, matrix elements, and enhancement of weak perturbations”. *Physical Review A*, 50.1 (1994) 267–296. DOI: 10.1103/physreva.50.267.

- [14] V. A. Dzuba, V. V. Flambaum, G. F. Gribakin, and C. Harabati, “Chaos-induced enhancement of resonant multielectron recombination in highly charged ions: Statistical theory”. *Physical Review A*, 86.2 (2012) 022714. DOI: 10.1103/physreva.86.022714.
- [15] E. P. Wigner, “Characteristic Vectors of Bordered Matrices With Infinite Dimensions”. *Annals of Mathematics*, 62.3 (1955) 548–564. ISSN: 0003486X. URL: <http://www.jstor.org/stable/1970079>.
- [16] E. P. Wigner, “Characteristics Vectors of Bordered Matrices with Infinite Dimensions II”. *Annals of Mathematics*, 65.2 (1957) 203–207. ISSN: 0003486X. URL: <http://www.jstor.org/stable/1969956>.
- [17] E. Fermi, E. Amaldi, O. D’Agostino, F. Rasetti, and E. Segre, “Artificial Radioactivity Produced by Neutron Bombardment”. *Proceedings of the Royal Society of London. Series A, Containing Papers of a Mathematical and Physical Character*, 146.857 (1934) 483–500. ISSN: 09501207. URL: <http://www.jstor.org/stable/2935604>.
- [18] E. Amaldi, O. D’Agostino, E. Fermi, B. Pontecorvo, F. Rasetti, and E. Segre, “Artificial Radioactivity Produced by Neutron Bombardment. II”. *Proceedings of the Royal Society of London. Series A, Mathematical and Physical Sciences*, 149.868 (1935) 522–558. ISSN: 00804630. URL: <http://www.jstor.org/stable/96379>.
- [19] N. Bohr, “Neutron Capture and Nuclear Constitution”. *Nature*, 137.3461 (1936) 344–348. DOI: 10.1038/137344a0.
- [20] M. L. Mehta, *Random Matrices*. 3rd ed. Amsterdam San Diego, CA: Academic Press, 2004. ISBN: 9780080474113.
- [21] C. E. Porter, *Statistical Theories of Spectra: Fluctuations*. Perspectives in Physics. New York: Academic Press, 1965. ISBN: 978-0125623506.
- [22] N. Rosenzweig and C. E. Porter, “Repulsion of Energy Levels” in Complex Atomic Spectra”. *Physical Review*, 120.5 (1960) 1698–1714. DOI: 10.1103/physrev.120.1698.
- [23] R. C. Block, W. M. Good, J. A. Harvey, H. W. Schmitt, and G. T. Trammell, *Conference on Neutron Physics by Time-Of-Flight Held at Gatlinburg, Tennessee, November 1 and 2, 1956*. Tech. rep. 1957. DOI: 10.2172/4319287.
- [24] M. Gaudin, “Sur la loi limite de l’espacement des valeurs propres d’une matrice aléatoire”. *Nuclear Physics*, 25 (1961) 447–458. DOI: 10.1016/0029-5582(61)90176-6.
- [25] F. J. Dyson and M. L. Mehta, “Statistical Theory of the Energy Levels of Complex Systems. IV”. *Journal of Mathematical Physics*, 4.5 (1963) 701–712. DOI: 10.1063/1.1704008.
- [26] J. Sheil, “Many-body quantum chaos and actinide ions: Testing the predictions of random matrix theory with high- Z ions”. *Physical Review A*, 98.2 (2018) 022521. DOI: 10.1103/physreva.98.022521.
- [27] C. E. Porter and R. G. Thomas, “Fluctuations of Nuclear Reaction Widths”. *Physical Review*, 104.2 (1956) 483–491. DOI: 10.1103/physrev.104.483.
- [28] V. V. Flambaum, A. A. Gribakina, and G. F. Gribakin, “Statistics of electromagnetic transitions as a signature of chaos in many-electron atoms”. *Physical Review A*, 58.1 (1998) 230–237. DOI: 10.1103/physreva.58.230.

- [29] A. Bohr and B. Mottelson, *Nuclear structure*. Vol. I. New York: World Scientific, 1969. ISBN: 9810239793.
- [30] H. A. Weidenmüller and G. E. Mitchell, “Random matrices and chaos in nuclear physics: Nuclear structure”. *Reviews of Modern Physics*, 81.2 (2009) 539–589. DOI: 10.1103/revmodphys.81.539.
- [31] T. A. Brody, J. Flores, J. B. French, P. A. Mello, A. Pandey, and S. S. M. Wong, “Random-matrix physics: spectrum and strength fluctuations”. *Reviews of Modern Physics*, 53.3 (1981) 385–479. DOI: 10.1103/revmodphys.53.385.
- [32] H. L. Harney, A. Richter, and H. A. Weidenmüller, “Breaking of isospin symmetry in compound-nucleus reactions”. *Reviews of Modern Physics*, 58.3 (1986) 607–645. DOI: 10.1103/revmodphys.58.607.
- [33] G. F. Gribakin and S. Sahoo, “Mixing of dielectronic and multiply excited states in electron–ion recombination: a study of Au24”. *Journal of Physics B: Atomic, Molecular and Optical Physics*, 36.15 (2003) 3349–3370. DOI: 10.1088/0953-4075/36/15/315.
- [34] G. E. Mitchell, A. Richter, and H. A. Weidenmüller, “Random matrices and chaos in nuclear physics: Nuclear reactions”. *Reviews of Modern Physics*, 82.4 (2010) 2845–2901. DOI: 10.1103/revmodphys.82.2845.
- [35] J. Gómez, K. Kar, V. Kota, R. Molina, A. Relaño, and J. Retamosa, “Many-body quantum chaos: Recent developments and applications to nuclei”. *Physics Reports*, 499.4-5 (2011) 103–226. DOI: 10.1016/j.physrep.2010.11.003.
- [36] T. Guhr, A. Müller-Groeling, and H. A. Weidenmüller, “Random-matrix theories in quantum physics: common concepts”. *Physics Reports*, 299.4-6 (1998) 189–425. DOI: 10.1016/s0370-1573(97)00088-4.
- [37] H. S. Camarda and P. D. Georgopoulos, “Statistical Behavior of Atomic Energy Levels: Agreement with Random-Matrix Theory”. *Physical Review Letters*, 50.7 (1983) 492–495. DOI: 10.1103/physrevlett.50.492.
- [38] G. F. Gribakin, A. A. Gribakina, and V. V. Flambaum, “Quantum Chaos in Multicharged Ions and Statistical Approach to the Calculation of Electron - Ion Resonant Radiative Recombination”. *Australian Journal of Physics*, 52.3 (1999) 443–457. DOI: 10.1071/ph98093.
- [39] A. Hoffknecht et al., “Recombination of Au25+ with free electrons at low energies”. *Hyperfine Interactions*, 114.1-4 (1998) 257–261. DOI: 10.1023/a:1012651311728.
- [40] V. V. Flambaum, A. A. Gribakina, G. F. Gribakin, and C. Harabati, “Electron recombination with multicharged ions via chaotic many-electron states”. *Physical Review A*, 66.1 (2002) 012713. DOI: 10.1103/physreva.66.012713.
- [41] V. A. Dzuba, V. V. Flambaum, G. F. Gribakin, C. Harabati, and M. G. Kozlov, “Electron recombination, photoionization, and scattering via many-electron compound resonances”. *Physical Review A*, 88.6 (2013) 062713. DOI: 10.1103/physreva.88.062713.
- [42] V. V. Flambaum, M. G. Kozlov, and G. F. Gribakin, “Coherent and stochastic contributions of compound resonances in atomic processes: Electron recombination, photoionization, and scattering”. *Physical Review A*, 91.5 (2015) 052704. DOI: 10.1103/physreva.91.052704.

- [43] J. C. Berengut, C. Harabati, V. A. Dzuba, V. V. Flambaum, and G. F. Gribakin, “Level-resolved quantum statistical theory of electron capture into many-electron compound resonances in highly charged ions”. *Physical Review A*, 92.6 (2015) 062717. DOI: 10.1103/physreva.92.062717.
- [44] H. A. Kramers, “XCIII. On the theory of X-ray absorption and of the continuous X-ray spectrum”. *The London, Edinburgh, and Dublin Philosophical Magazine and Journal of Science*, 46.275 (1923) 836–871. DOI: 10.1080/14786442308565244.
- [45] Y. Hahn, “Electron - ion recombination processes - an overview”. *Reports on Progress in Physics*, 60.7 (1997) 691–759. DOI: 10.1088/0034-4885/60/7/001.
- [46] W. G. Graham, W. Fritsch, Y. Hahn, and J. Tanis, *Recombination of Atomic Ions*. Boston, MA: Springer US Imprint Springer, 1992. ISBN: 9781461534709.
- [47] L. D. Landau and E. M. Lifshitz, *Quantum Mechanics Non-Relativistic Theory*. Elsevier LTD, Oxford, 1981. ISBN: 0750635398.
- [48] S. Schippers et al., “Dielectronic recombination of xenonlike tungsten ions”. *Physical Review A*, 83.1 (2011) 012711. DOI: 10.1103/physreva.83.012711.
- [49] G. W. F. Drake, *Springer Handbook of Atomic, Molecular, and Optical Physics*. Springer Nature, Dec. 1, 2005. 1504 pp. ISBN: 038720802X. URL: [https://www.ebook.de/de/product/3897829/springer\\_handbook\\_of\\_atomic\\_molecular\\_and\\_optical\\_physics.html](https://www.ebook.de/de/product/3897829/springer_handbook_of_atomic_molecular_and_optical_physics.html).
- [50] A. Corney, *Atomic and Laser Spectroscopy*. OUP Oxford, Oct. 5, 2006. 782 pp. ISBN: 0199211450. URL: [https://www.ebook.de/de/product/5839650/alan\\_corney\\_atomic\\_and\\_laser\\_spectroscopy.html](https://www.ebook.de/de/product/5839650/alan_corney_atomic_and_laser_spectroscopy.html).
- [51] J. Sheil and Versolato, “Multiply-excited states and their contribution to opacity in CO<sub>2</sub> laser-driventin-plasma conditions”. 2020.
- [52] E. V. Kahl and J. C. Berengut, “AMBiT: A programme for high-precision relativistic atomic structure calculations”. *Computer Physics Communications*, 238 (2019) 232–243. DOI: 10.1016/j.cpc.2018.12.014.
- [53] V. A. Dzuba and V. V. Flambaum, “Exponential Increase of Energy Level Density in Atoms: Th and Th II”. *Physical Review Letters*, 104.21 (2010). DOI: 10.1103/physrevlett.104.213002.
- [54] R. Karazija, S. Kučas, V. Jonauskas, and A. Momkauskaitė, “Formation of a Narrow Group of Intense Lines in the Emission and Photoexcitation Spectra”. In: *New Trends in Atomic and Molecular Physics*. Springer Berlin Heidelberg, 2013, pp. 167–188. DOI: 10.1007/978-3-642-38167-6\_10.
- [55] K. Fujii and J. C. Berengut, “Simple Explanation for the Observed Power Law Distribution of Line Intensity in Complex Many-Electron Atoms”. *Physical Review Letters*, 124.18 (2020). DOI: 10.1103/physrevlett.124.185002.
- [56] S. Kučas, V. Jonauskas, R. Karazija, and I. Martinson, “Global characteristics of atomic spectra and their use for the analysis of spectra. II. characteristic emission spectra”. *Physica Scripta*, 51.5 (1995) 566–577. DOI: 10.1088/0031-8949/51/5/004.
- [57] J. Bauche, C. Bauche-Arnoult, and O. Peyrusse, *Atomic Properties in Hot Plasmas*. Springer International Publishing, 2015. DOI: 10.1007/978-3-319-18147-9.